Optimization of Reconstruction Methods and Injected Activity for Whole Body [^{18}F]FDG PET/CT Imaging

by

Alexander Hart
BS, Pacific Lutheran University, 2015

A Thesis Submitted in Partial Fulfillment of the
Requirements for the Degree of

MASTER OF SCIENCE

In the Department of Physics and Astronomy

Optimization of Reconstruction Methods and Injected Activity for Whole Body [^{18}F]FDG PET/CT Imaging

by

Alexander Hart
BS, Pacific Lutheran University, 2015

Supervisory Committee

Dr. Wayne Beckham, Co-Supervisor
Department of Physics and Astronomy

Dr. Magdalena Bazalova-Carter, Co-Supervisor
Department of Physics and Astronomy

Dr. Derek Wells, Committee Member
Department of Physics and Astronomy

Dr. Arman Rahmim, Committee Member
Department of Physics and Astronomy

Dr. Carlos Uribe, Committee Member
Department of Physics and Astronomy

Abstract

[^{18}F]Fluorodeoxyglucose ([^{18}F]FDG) Positron Emission Tomography/Computed Tomography (PET/CT) imaging is a powerful tool in the diagnosis of cancer and subsequent treatment planning. New state-of-the-art PET/CT scanners have the capacity to generate images of superb quality. The new scanners feature detectors with increased sensitivity and a new generation of reconstruction algorithms that produce higher quality images than the scanners they are replacing. In addition to the scanner, the scan duration, amount of administered [^{18}F]FDG activity, and the anatomy of the patients themselves are also determining factors of image quality. There is evidence suggesting that [^{18}F]FDG PET image quality is significantly reduced for larger patients, jeopardizing lesion detection. Two possible solutions to this problem are to (i) increase injected activity or (ii) increase scan duration. Increasing scan duration is preferable but not always possible in a busy clinic. Increasing injected activity is necessary but a proper scaling regimen with patient size must be determined in order to achieve consistent image quality. The aim of the work presented in this thesis was to achieve higher quantification accuracy and consistent image quality for all patients scanned with [^{18}F]FDG PET.

Because quantitative PET/CT images require corrections for image degrading effects, for which attenuation correction is the main contributor and is performed based on CT images, the first step in this project was to develop software tools to automate the analysis of phantom images for CT quality assurance. The next step was to optimize the reconstruction parameters for whole body [^{18}F]FDG PET based on a phantom experiment. Finally, a retrospective study was conducted using patient [^{18}F]FDG PET images to characterize the relationship between patient anatomical characteristics and image quality. This work concludes by suggesting optimized reconstruction parameters and a scaling regimen for injected [^{18}F]FDG activity. With the implementation of these recommendations it can be possible to obtain images with increased quantitative value while delivering less dose to patients and maintaining a uniform level of image quality between different patients.

Contents

Supervisory Committee ii

Abstract iii

Contents iv

List of Figures vii

List of Tables xi

Acknowledgements xii

Dedication xiii

1 Introduction 1
1.1 Thesis Scope . . . 2

2 Physics of Nuclear Medicine Imaging 3
2.1 Physics of Nuclear Medicine Imaging . . . 3
2.1.1 Positron Emission and Radioactivity . . . 3
2.1.2 Interactions of Charged Particles . . . 4
2.1.3 Photon Interactions with Matter . . . 6
2.2 Positron Emission Tomography . . . 8
2.2.1 [^{18}F]Fluorodeoxyglucose PET . . . 8
2.2.2 Annihilation Coincidence Detection . . . 11
2.2.3 Scintillator Detectors . . . 12
2.2.4 Sources of Image Degradation in PET . . . 13
2.2.5 Performance of PET Scanners . . . 16
2.3 PET Reconstruction Methods . . . 17
2.3.1 Filtered Back Projection . . . 17
2.3.2 Iterative Reconstruction Methods . . . 18
2.4 X-ray Computed Tomography . . . 20
2.4.1 Applications of X-ray CT . . . 22
2.4.2 Production of X-rays . . . 23
2.4.3 Scintillator Detectors . . . 25

2.5 Image Quality 25

3 Automated CT QA Analysis **28**
3.1 Introduction 28
3.2 Materials & Methods 29
3.2.1 Automated Analysis Software 30
3.2.2 Phantom Scanning 36
3.3 Results 38
3.4 Discussion 39
3.5 Conclusion 40

4 Optimization of Reconstruction Parameters and Injected Activity **41**
4.1 Introduction 41
4.2 Materials & Methods 42
4.2.1 PET Scanner 42
4.2.2 Phantom Preparation 42
4.2.3 Image Acquisition 44
4.2.4 Reconstruction Parameter Optimization 46
4.2.5 Analysis Methods 47
4.2.6 Injected Activity Optimization 50
4.3 Results 51
4.3.1 Recovery Coefficients 51
4.3.2 Coefficient of Variation 52
4.3.3 Combined Error 54
4.3.4 Time Activity Product 59
4.4 Discussion 62
4.4.1 Limits 64
4.5 Conclusions 65

5 Optimization of Injected [^{18}F]FDG based on Patient Image Quality Study **66**
5.1 Introduction 66
5.2 Methods 67
5.2.1 Patient Inclusion Criteria 67
5.2.2 Scanners and Image Reconstructions 68
5.2.3 Signal-to-Noise Ratio Calculation 69
5.2.4 Extraction of Patient Metadata 70
5.2.5 Analysis 72
5.3 Results 74
5.4 Discussion 86
5.4.1 Limits: 88
5.5 Conclusions 88

6 Conclusions **90**

Appendix A [^{18}F]FDG Injected Activity Tables **101**
A.1 Injected Activity (MBq): Discovery MI - HDS 2i 34s 6.4mm FWHM . . 101
A.2 Injected Activity (MBq): Discovery MI - FXS 3i 8s 3.2mm FWHM 107
A.3 Injected Activity (MBq): Discovery MI - QFX $\beta = 600$ 112

List of Figures

2.1 **Positron Emission and Annihilation:** after the positron annihilates with an electron, two 511 keV photons are produced with 180 degree separation. Case courtesy of Dr Mohamed Elbanan, Radiopaedia.org, rID: 16433 5
2.2 **Photoelectric Effect:** . Adapted from Bushberg *et al.* [1]. 6
2.3 **Mass Attenuation Coefficients:** It can be seen that for the 511 keV annihilation photons in soft tissue, Compton scattering is the dominant interaction. Adapted from Bushberg *et al.* [1]. 8
2.4 **Decay scheme of ^{18}F:** ^{18}F decays by electron capture 3% of the time and by positron emission the remaining 97%. 9
2.5 **Biological Uptake of FDG** Adapted from Rahman [2]. 10
2.6 **FDG Accumulation in Malignant and Inflammatory Tissues.** Adapted from Houshmand *et al.* [3]. 10
2.7 **Coincidence Detection of Annihilation Photons:** . Adapted from Badawi [4]. 11
2.8 **Time-of-flight PET:** . Adapted from Lecoq [5]. 12
2.9 **Types of Coincidences in PET:** . Adapted from Badawi (1999). 14
2.10 **Noise Equivalent Count Rate:** A sample NECR curve obtained using a NEMA Image Quality Phantom. Adapted from Del Guerra [6]. 17
2.11 **Back Projection in PET:** Back projection results in star shaped (for low numbers of projections) or ringing artifacts (for higher number of projections) around an imaged point source. Adapted from Badawi [4]. 18
2.12 **Iterative Reconstruction:** Visual representation of the iterative reconstruction process used in OSEM. Adapted from G. Sasha [7]. 19
2.13 **Fan Beam Geometry of X-ray CT:** Adapted from Bushberg *et al.* [1]. . 21
2.14 HU values for several materials at two x-ray energies. Note that water is fixed at 0 for both energies. Adapted from Bushberg *et al.* [1]. 22
2.15 **Components of an X-ray Tube:** Adapted from Bushberg *et al.* [1]. . . 24
2.16 **Energy Spectra of X-ray Tubes:** Relative x-ray fluence for different peak energies (each spectra normalized independently). Adapted from Bushberg *et al.*[1]. 24

2.17 **Modulation Transfer Function:** the conventional method is determined by imaging an edge, while the *modulation* method requires measuring the standard deviation of pixels in an ROI. Adapted from Droege [8]. 27

3.1 Schematic of QA Phantom including positioning bracket [9]. 29
3.2 ROIs used to determine high contrast resolution and the measured MTF fit with a cubic spline. 31
3.3 CT slice showing rectangular ROIs used to calculate contrast scale. The lower right ROI shown is placed in water, and the upper left ROI is in plastic. 32
3.4 CT reconstructions of two different slice thicknesses (5.0, and 10.0 mm) and the corresponding profiles used to verify slice thickness. 33
3.5 Profile across top of the CT phantom. The minimum indicates the position of the drilled hole which corresponds to the etched laser alignment mark. 34
3.6 CT slice displaying central and cardinal ROIs used to determine system noise and uniformity. 35
3.7 CT slice displaying 3mm grid in the uniform water region, detectability vs object size function, and distribution of mean HU. 36
3.8 The GE CT QA phantom positioned on the scanner bed, aligned to the external lasers. 38
3.9 Example output summary of CT QA auto analysis software. 39

4.1 **Intego Automatic Injector:** Printed label from the Intego confirming the activity of [^{18}F]FDG dispensed into the background of the NEMA phantom. 44
4.2 **NEMA IQ Phantom:** A side view of the prepared NEMA phantom shows the spheres, lung insert, and uniform background region filled with FDG and green dye. 44
4.3 The NEMA IQ phantom is positioned on the scanner bed in preparation for image acquisition. 45
4.4 **Reconstruction Parameter Optimization Decision Tree** 46
4.5 **Acquired Images**: CT used for attenuation correction (a), and reconstructed PET image using clinical parameters: non TOF, 2 iterations, 34 subsets, 6.4mm FWHM post reconstruction Gaussian smoothing (b). 47
4.6 **NEMA IQ ROI Placement** Axial PET slice of NEMA IQ phantom, showing ROI placement for background COV calculation (a) and segmentation of the spheres before thresholding is applied (b). 49
4.7 **Recovery Coefficients**: Mean, maximum, and peak recovery coefficients for the current Clinical reconstruction **(a,d,g)** as well as FXS with varying iterative update products **(b,e,h)** and QFX with varying β values **(c,f,i)** 53

4.8 **Coefficient of Variation**: COV for the current Clinical reconstruction (HDS 2i 34s 6.4 mm FWHM) and FXS with varying number of iterative updates **(a)** as well as QFX with varying β values **(b)** 54
4.9 **Reconstruction Algorithm Optimization:** Bias vs noise curves were generated for each alorithm type: non TOF OSEM with and without PSF (HDS/HD), TOF OSEM with and without PSF (FXS/FX), and TOF BSREM (QFX). Shown are bias vs noise curves for mean (a), max (b), and peak (c) bias. 56
4.10 **Combined Error:** The label for each point on the OSEM reconstructions indicates the IUP used, and the BSREM reconstructions (QFX) are labeled with the choice of β parameter. 57
4.11 **Post Reconstruction Smoothing**: Mean, max, and peak recovery coefficients for the FXS reconstruction with chosen number of iterative updates and varying level of post reconstruction Gaussian smoothing **(a,b,c)**. Also, the effect of smoothing on the COV in the background region **(d)**. 58
4.12 **Combined Error:** Post Reconstruction Gaussian smoothing from 0mm to 4.0mm FWHM 59
4.13 **Reduced Scan Duration**: The effect of relisting the 10 minute scan for shorter scan durations is analogous to injecting a lower activity of [^{18}F]FDG. 60
4.14 **Minimum Scan Duration:** T_{min} is determined using the power law fit of COV and scan duration and a noise threshold of 10% 61
4.15 **Low Counting Statistics:** RCs are shown for reconstructions of 1 minute acquisitions re-binned from list mode data using the Clinical and optimized FXS reconstructions. 62
4.16 **Optimized Reconstructions:** The same axial slice of the NEMA IQ is shown reconstructed with the Clinical reconstruction (HDS 2i 34s 6.4mm FWHM) (**a**) as well as the optimized reconstructions: FXS with 3i 8s 3.2mm FWHM (**b**) and QFX with $\beta = 600$ (**c**) 63

5.1 **Distribution of Patient Body Mass**: Patient body mass was extracted from the DICOM headers of scans used in this study acquired on the Discovery MI and D690 scanner reconstructed with non-TOF and TOF. 68
5.2 **Patient FDG PET Images**: axial and coronal slices of a patient PET image reconstructed with non-TOF **(a,c)** and TOF **(b,d)** scanned with the Discovery MI. The placement of spherical VOIs is also shown. 70
5.3 **Injection information for the patients scanned on the Discovery MI**: The activity of [^{18}F]FDG at time of injection **(a)**, and decay-corrected to time of scan **(b)** as a function of patient body mass for scans acquired in Victoria with the Discovery MI. Also shown are the bed durations **(c)**, and time-activity product **(d)**. 75

5.4 **Injection information for the patients scanned on the D690**: The activity of [^{18}F]FDG at time of injection **(a)**, and decay-corrected to time of scan **(b)** as a function of patient body mass for scans acquired in Vancouver with the D690. Also shown are the bed durations **(c)**, and time-activity product **(d)**. 76
5.5 **Image Quality for PET/CT images acquired with the Discovery MI scanner**: The measured SNR_L and COV as a function of patient body mass for non-TOF reconstructions **(a,c)** and TOF **(b,d)**. 77
5.6 **Image Quality for PET/CT images acquired with the D690 scanner**: The measured SNR_L and COV as a function of patient body mass for non-TOF reconstructions **(a,c)** and TOF **(b,d)**. 78
5.7 **Discovery MI (non-TOF) Normalized SNR**: SNR_L normalized by the injected activity and scan duration as a function of patient dependent anatomical characteristics for patients scanned on the Discovery MI reconstructed with non-TOF. Only the lean body mass and fat mass definitions with the highest R^2 are shown. 79
5.8 **Discovery MI (TOF) Normalized SNR**: SNR_L normalized by the injected activity and scan duration as a function of patient dependent anatomical characteristics for patients scanned on the Discovery MI reconstructed with TOF. Only the lean body mass and fat mass definitions with the highest R^2 are shown. 80
5.9 **D690 (non-TOF) Normalized SNR**: SNR_L normalized by the injected activity and scan duration as a function of patient dependent anatomical characteristics for patients scanned on the D690 reconstructed with non-TOF. Only the lean body mass and fat mass definitions with the highest R^2 are shown. 81
5.10 **D690 (TOF) Normalized SNR**: SNR_L normalized by the injected activity and scan duration as a function of patient dependent anatomical characteristics for patients scanned on the D690 reconstructed with TOF. Only the lean body mass and fat mass definitions with the highest R^2 are shown. 82
5.11 **New Activity Protocols:** TAP protocols based on equations 5.19, 5.20, and 5.21 for the current clinically used reconstruction (HDS 2i 34s), optimized FXS 3i 8s, and QFX $\beta = 600$, respectively. The TAP used in the patient study is also shown. 84
5.12 **Hepatic Activity Concentration**: measured from TOF scans **(a)**, plotted as a function of injected activity per mass **(b,c)**, and normalized by injected activity per mass **(d)**. 86

List of Tables

2.1 **Characteristics of Common Scintillators Used in Nuclear Medicine:** adapted from Chandra and Rahmim (2018) 13

4.1 **OSEM Reconstructions**: GE reconstruction algorithm names for combinations of TOF and PSF options used in this study. 55
4.2 **IUP**: Iterative updates used for all OSEM reconstructions shown in figure 4.9 55
4.3 Combined Error of optimized reconstructions. Lower Combined Error values are preferred. 56
4.4 **Time Activity Product:** Minimum product of injected activity and scan duration for Clinical HDS, optimized FXS and QFX reconstructions. 61

5.1 **Scan Parameters**: The scanner and reconstructions used to acquire all patient images. Vue Point HDS and FXS are GE's OSEM reconstruction algorithms incorporrating PSF correction (referred to as SharpIR by the manufacturer). 69
5.2 **TAP**: time-activity products calculated using equations 5.19, 5.20, and 5.21 for several patient body masses. 84
5.3 **Fit of SNR_L**: Fit parameters are shown for Discovery MI and D690 scanners with both non-TOF and TOF reconstructions.*b value chosen for scaling time activity product with patient body mass. 85

Acknowledgements

The majority of the work included in this thesis was conducted during the first year of the COVID-19 pandemic. Separated by the USA/Canada border, this is the longest in my life I have gone without seeing my family (which has since grown to include my niece Anastasia). As I'm sure it has been for just about everyone, it has been at times exasperating and demoralizing. That being said, I am extremely lucky to have had the support of a truly exceptional group of people that I would like to acknowledge here. Without them, I would not be writing this today.

It has been a tremendous honor to spend the first years of my graduate career as a member of the UBC-based Qurit lab. Though the pandemic kept us physically separated, our weekly lab meetings over video conference consistently reminded me that I was part of something bigger than myself. I would like to thank Arman Rahmim for modeling the scientific integrity and leadership skills that I would like to possess someday.

This project would have been impossible without the guidance and mentorship of Carlos Uribe. His patience while teaching me object-oriented programming over the phone, and repeating experiments for me after the COVID-19 protocols left me unable to access BC Cancer, will never be forgotten. I consider it a special privilege to be his first MSc student.

Magdalena Bazalova-Carter and Wayne Beckham helped to keep this project on the rails and their genuine support was evident from the moment I chose University of Victoria for my graduate education.

Teaghan O'Briain deserves to be acknowledged for the excellent contribution he made to this project by developing analysis software for PET phantom images.

I would like to thank the PET technologists at BC Cancer Victoria, including Jenn Forer, for sharing their time and expertise (and unlocking doors for me). I hope they will forgive me for any extra hours in the clinic as a consequence of this project.

Finally, I want to thank my family. Their support was clearly felt all the way from Texas. I sure hope I'll be seeing them soon.

Dedication

For my nieces Elizabeth, Juliette, and Anastasia

Chapter 1

Introduction

[^{18}F]Fluorodeoxyglucose ([^{18}F]FDG) Positron Emission Tomography (PET) is an indispensable tool in the diagnosis and treatment of malignant disease. To obtain PET images, radiopharmaceuticals are injected intravenously prior to scanning. By selecting radiopharmaceuticals associated with biological processes of interest such as tumour metabolism ([^{18}F]FDG), it is possible to gain functional insight not attainable with other imaging modalities [10]. Within the first few decades of clinical use, [^{18}F]FDG PET was shown to provide average sensitivities and specificities of 84% and 88%, respectively, across a wide variety of cancers [11][12]. The utility of [^{18}F]FDG PET in oncology continues to expand, finding roles beyond cancer detection including staging [13], radiotherapy planning [14], and treatment response assessment [15].

Positron Emission Tomography/Computed Tomography (PET/CT) imaging combines the functional, molecular imaging of nuclear medicine with the structural, high resolution, anatomical imaging of x-ray CT. The CT images can be used both as a method of correction for PET as well as for diagnostic and treatment planning purposes.

The image quality and quantitative value of a PET image depends greatly on the reconstruction algorithm and parameters used [16]. With the rapid increase in availability of computational resources, advanced reconstruction methods can be used in the clinic, including penalized-likelihood estimation algorithms which could enable acquisition of more quantitative PET images without increasing noise [17].

The higher sensitivity of state-of-the-art PET scanners combined with the implementation of advanced reconstruction algorithms may allow for reduced in-

jected activities while maintaining excellent image quality [18]. However, [18F]FDG PET/CT images can be degraded by differences in counting statistics caused by patient anatomical characteristics such as body mass, lean body mass, or body surface area. Poor image quality can prevent the detection of small tumours in larger patients and raise the rate of false negatives [19]. Scaling the time-activity product (TAP) (i.e. the product of injected activity and bed duration) is one way to mitigate degradation in image quality [20]. There is not, however, consensus within the field on the appropriate method of scaling the TAP for each patient. Proposed methods range from linear [21] to quadratic [22] relations with patient body mass or even relations with multiple patient dependent anatomical characteristics [23].

1.1 Thesis Scope

The purpose of the work outlined in this thesis is to enable the acquisition of high quality, quantitative PET/CT images by: (i) developing and implementing an automated quality assurance process for CT, (ii) optimizing the reconstruction parameters used for PET, and finally, (iii) optimizing injected activity of [^{18}F]FDG in order to obtain consistent image quality independent of patient anatomy.

Chapter 2 will provide a theoretical framework for the work described in this thesis, including the basic physics of nuclear medicine imaging. In chapter 3, the development of an automated quality assurance software package will be discussed. Daily quality assurance is performed on the CT functionality of the PET/CT scanners by scanning an acrylic, water filled phantom. After scan acquisition, the PET technologists are required to manually perform image analysis on several reconstructions of the scan. The software described in chapter 3 was developed to automatically conduct the image analysis, reducing the workload of the technologists and providing a more consistent analysis procedure.

Chapter 4 focuses on PET studies of an image quality phantom. Clinical PET reconstruction methods were optimized by reconstructing the phantom data and analyzing the images for noise and bias. The results from this study were then combined with a retrospective image quality study of patient [^{18}F]FDG PET images to determine the optimum protocol for injected activity presented in chapter 5. The culmination of this work and recommendations for clinical implementation are summarized in chapter 6.

Chapter 2

Physics of Nuclear Medicine Imaging

2.1 Physics of Nuclear Medicine Imaging

This chapter will provide the background information necessary for the work undertaken in the MSc. The basic physics of PET and x-ray CT imaging will be introduced.

2.1.1 Positron Emission and Radioactivity

Central to nuclear medicine imaging is the radioactive decay of unstable nuclei. When a nucleus is unstable because it is neutron deficient, it can achieve stability by one of two methods of decay: *electron capture* or *positron emission*. During electron capture, one of the orbital electrons from a tightly bound shell (K, L, or M) is combined with a proton inside the nucleus to form an additional neutron. A neutrino is also emitted. *Positron emission* occurs when a proton (p) turns into a neutron (n) according to:

$$p \rightarrow n + \beta^{+} + \upsilon_e \tag{2.1}$$

where n is a neutron, β^{+} is a positron, and υ_e is an electron neutrino. Therefore, a generic unstable isotope, X, undergoes the following:

$${}^{M}_{Z}X \rightarrow {}^{M}_{Z-1}X + \beta^{+} + \upsilon_e \tag{2.2}$$

The rate at which a sample of radioactive atoms decays (such as the ^{18}F shown in figure 2.4) is called the *activity* and is measured in disintegrations per second or becquerel (Bq). The activity, A, of a radioactive sample can be determined by the number of atoms, N, and the decay constant, λ, which is unique to each radioisotope according to:

$$A = -\frac{dN}{dt} = \lambda \times N \tag{2.3}$$

By solving this differential equation, the amount of remaining radioactive atoms, N_t, is seen to decay exponentially:

$$N_t = N_0 e^{-(\lambda \times t)} \tag{2.4}$$

where N_0 is the number of radioactive atoms at t = 0. In addition to λ, the time required for the activity of a radioactive sample to reduce by half, or the *half-life* is often used. The half-life is related to λ by:

$$T_{1/2} = \frac{ln(2)}{\lambda} \tag{2.5}$$

The half-life of ^{18}F is 109.8 minutes, which means that if a patient is administered 200 MBq 1 hour before scanning, the activity will be ~137 MBq at the time of the scan.

2.1.2 Interactions of Charged Particles

After an unstable nuclei decays by positron emission, there are several interactions that the positron (a charged particle) can undergo before detection. Conservation of energy with the emitted electron neutrino allows the positron to obtain a continuous spectrum of energies (with a maximum and mean energies of 0.634 and 0.250 MeV, respectively for ^{18}F) [24]. After the positron is produced, it loses energy primarily via Coulomb interactions with surrounding atoms. Positrons can also lose energy by emitting visible Cherenkov radiation. This occurs when the positrons travel faster than the speed of light in the particular medium, leading to a visual phenomena analogous to a sonic boom. The emitted Cherenkov light can be imaged in some conditions but only penetrates a few millimeters in tissue.

Eventually, the positron reaches the end of its range when it has lost nearly all of its kinetic energy. At this point, the positron can interact with an electron by either directly annihilating to produce two 511 keV photons (equal to the rest energy

of the positron-electron pair), or forming an unstable exotic atom, positronium. In the singlet state of positronium, *para*-positronium, the result is also an annihilation event producing two photons, while the triplet state, *ortho*-positronium, yields three annihilation photons. This triplet state comprises a small proportion of annihilation events and is not accounted for when imaging positron-emitters.

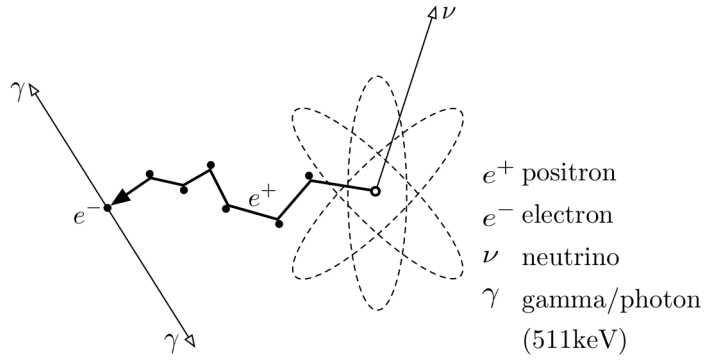

Figure 2.1: **Positron Emission and Annihilation:** after the positron annihilates with an electron, two 511 keV photons are produced with 180 degree separation. Case courtesy of Dr Mohamed Elbanan, Radiopaedia.org, rID: 16433

The distance the positron travels before annihilation, the positron range, is dependent on the kinetic energy imparted to the positron, which varies by isotope. The greater the positron range, the larger the displacement between the detected annihilation event and the biodistribution of interest. Therefore, the positron range imposes an isotope-dependent spatial resolution limit on PET imaging. Positron ranges include 0.22 mm for ^{18}F and 1.07 mm for ^{68}Ga.

Charged particles, including positrons, can also lose energy by emitting high energy x-rays as they decelerate in the presence of the electric field of nuclei. The likelihood of this *Bremmsstrahlung* (or "braking radiation") in a material is proportional to the energy (E in MeV) of the positron or electron and the atomic number (Z) of the material according to:

$$f \approx \frac{Z \cdot E}{1,400} \tag{2.6}$$

where f is the fraction of the charged particle's energy released as x-rays. This process is largely ignored for PET imaging with ^{18}F but is utilized for the imaging of other isotopes including ^{90}Y [25], and is of paramount importance in the production of x-rays for CT imaging, as will be discussed later.

2.1.3 Photon Interactions with Matter

In PET imaging, the biodistribution of radio tracers are indirectly measured by detecting 511 keV photons. Compared to positrons, photons have a much lower probability of interacting with matter and thus traverse much greater distances through tissue. They are however, still subject to attenuation through several processes: photoelectric, pair and triplet production, photodisintegration, Rayleigh, and Compton scattering. The probability of any of these processes occurring is called its *cross section* and depends on the atomic number of the medium and the energy of the photon.

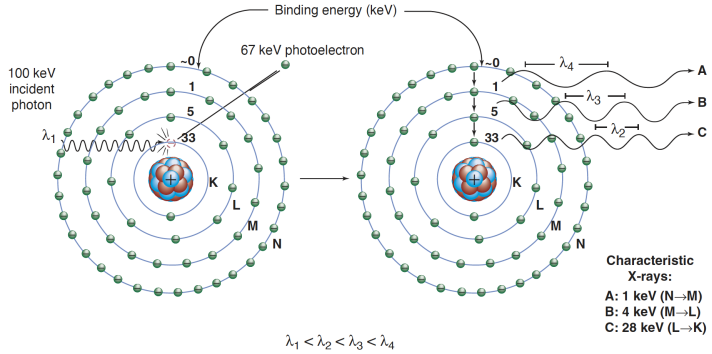

Figure 2.2: **Photoelectric Effect:** . Adapted from Bushberg *et al.* [1].

Also called coherent scattering, *Rayleigh scattering* occurs when an incident photon interacts with an entire atom. No energy is transferred from the photon to the atom or any of its constituent parts, but the photon is scattered by a small angle.

In the case of the *photoelectric effect*, an incident photon is completely absorbed by an orbital electron. The incident photon must have an energy exceeding the binding energy of the electron. The ejected photo-electron also gains the energy of the photon ($h\nu$) in excess of the binding energy (E_b) according to:

$$E_{pe} = h\nu - E_b \tag{2.7}$$

where E_{pe} is the kinetic energy of the ejected photo-electron. The photoelectric effect can also lead to a cascade of other processes including the emission of characteristic x-rays or Auger-Meitner electrons. If a vacancy is left in an inner shell, electrons from upper shells will fall to fill its place. If an ejected electron from the

K-shell of an atom is filled by an L-shell electron, either a characteristic x-ray with an energy equal to the difference of the binding energies of the two shells will be emitted (as shown in figure 2.2), or an additional L-shell electron will be emitted (called an Auger-Meitner electron after its co-discoverers) [26].

Unlike Rayleigh scattering, *Compton* (or incoherent) scattering involves the transfer of some of the incident photon energy to an orbital electron that is ejected from the atom. The incident photon must have an energy far exceeding the binding energy of the electron (that can be considered a free orbital electron). After the collision, conservation of energy shows that the electron has a kinetic energy, T:

$$T = h\nu - h\nu' \tag{2.8}$$

where $h\nu'$ is the energy of the scattered photon. Compton scattering events are the most prominent interaction of photons in tissue-equivalent media in the energy range of 20 keV to 20 MeV. Therefore, they are extremely relevant to the nuclear medicine and x-ray imaging modalities discussed in this work.

In *pair* and *triplet production* an incident photon interacts with the Coulomb field of a nucleus or orbital electron, respectively. The photon disappears, converting its energy into a created electron-positron pair in pair production. In the case of the photon interacting with the Coulomb field of the orbital electron, this electron is emitted along with the new electron-positron pair (the so-called triplet). The threshold energy for these processes is $2m_e c^2 = 1.022$ MeV, and $4m_e c^2 = 2.044$ MeV for pair and triplet production, respectively.

Another possibility of direct photon interaction with the nucleus is the *photonuclear effect* (also called photodisintegration). In this case the incident photon is completely absorbed and a neutron (referred to as a photo-neutron) is ejected. The threshold energy varies with nuclide but on average is ~8 MeV.

Attenuation Coefficients: Each of the processes described above has some probability of attenuating a photons as they travel through an absorbing medium. The number of photons that pass through the medium without interaction, N, is given by:

$$N = N_0 e^{-\mu x} \tag{2.9}$$

where N_0 is the number of incident photons, x is the total thickness of the absorber, and μ is the *linear attenuation coefficient* for the absorbing material at the energy of the incident photon, given in units of cm^{-1}. It is common to normalize the linear attenuation coefficient by the density of the material (μ/ρ) to obtain the

mass attenuation coefficient as shown in figure 2.3.

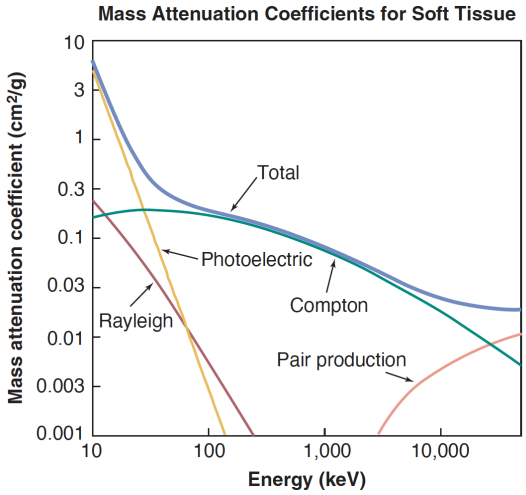

Figure 2.3: **Mass Attenuation Coefficients:** It can be seen that for the 511 keV annihilation photons in soft tissue, Compton scattering is the dominant interaction. Adapted from Bushberg *et al.* [1].

2.2 Positron Emission Tomography

This section provides an overview of PET imaging: from the correction techniques and reconstruction methods used to obtain high quality diagnostic images to the applications of PET imaging. A discussion of how the performance of a PET scanner can be evaluated is also presented.

2.2.1 [^{18}F]Fluorodeoxyglucose PET

The radiopharmaceutical of interest in this thesis is [^{18}F]Fluorodeoxyglucose ([^{18}F]FDG), which relies on the chemical and physical properties of the positron emitter, ^{18}F, to be useful for medical imaging. ^{18}F can be produced by a cyclotron through a few different methods, most commonly by bombarding an $H_2{}^{18}O$ target with 11 - 18 MeV protons which causes the following reaction [7]:

$$ {}^{18}_{8}O + p \rightarrow {}^{18}_{9}F + n \tag{2.10} $$

^{18}F then decays to ^{18}O following the scheme shown in figure 2.4 by emitting a positron ~97% of the time with a half-life of 109.8 minutes. One of the advantages

of radiopharmaceuticals labeled with ^{18}F is that the half-life allows for transportation (within ∼200 miles) from a regional cyclotron [7]. Another advantage comes from the short mean range of the positrons emitted by ^{18}F (0.22mm) [27] which limits the degradation in spatial resolution.

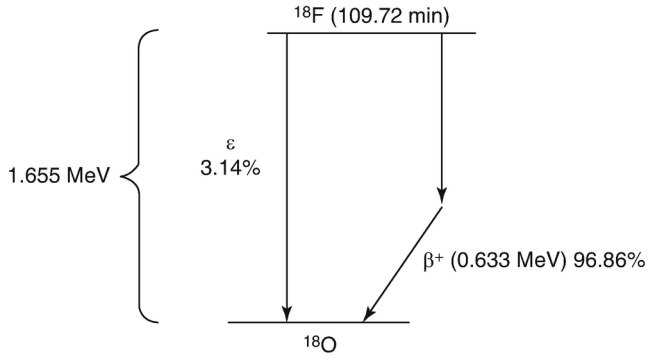

Figure 2.4: **Decay scheme of ^{18}F:** ^{18}F decays by electron capture 3% of the time and by positron emission the remaining 97%.

[^{18}F]FDG PET is a molecular imaging modality that takes advantage of the fact that cancer cells generally uptake and metabolize glucose at higher rates than normal tissue [28]. [^{18}F]FDG, which is a glucose analogue, gets treated by cancer cells in the same way. After intravenous injection, FDG radio-labeled with ^{18}F transfers from the blood into tissue. As shown in figure 2.5 the [^{18}F]FDG is phosphorylated with hexokinase to become [^{18}F]FDG-6-phosphate. Unlike normal glucose, cancer cells cannot further metabolize the [^{18}F]FDG. Cancer cells also have less of the enzyme glucose-6-phosphatase which is used by other tissues to dephosphorylate the [^{18}F]FDG-6-phosphate and release the free FDG into the bloodstream. Instead, the [^{18}F]FDG-6-phosphate continues to accumulate in malignant tissues as can be seen in figure 2.6. Due to these biokinetics, the ratio of [^{18}F]FDG concentrations in tumours to normal tissues are optimal between 20 and 90 minutes post injection [27]. For this reason, [^{18}F]FDG PET scans are generally obtained at 60 minutes post injection.

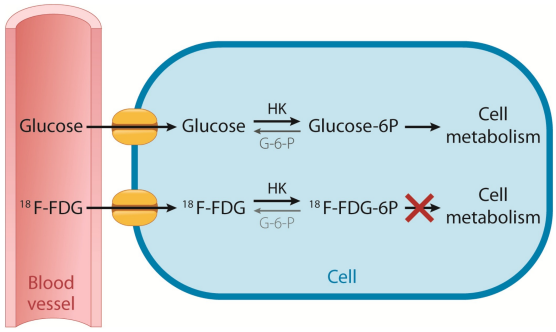

Figure 2.5: **Biological Uptake of FDG** Adapted from Rahman [2].

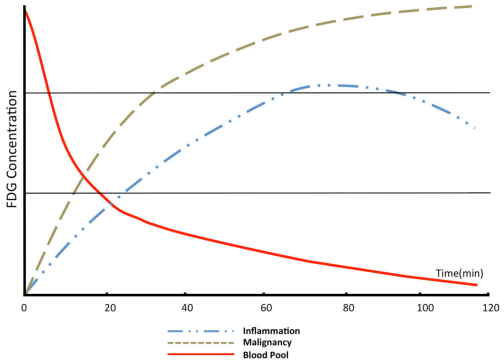

Figure 2.6: **FDG Accumulation in Malignant and Inflammatory Tissues.** Adapted from Houshmand *et al.* [3].

While originally developed for imaging metabolism in the brain, FDG PET has proven to be an invaluable tool in oncology, and is now the primary clinical PET procedure [29]. The value of each pixel in a PET image represents the estimated FDG activity concentration (kBq/mL) in the corresponding volume element (voxel) of the patient. Often, these activity concentrations are normalized by the injected activity per body weight. This is referred to as the standard uptake value (SUV), and is typically given by [30]:

$$SUV = \frac{\text{Decay-corrected activity concentration}}{\text{Injected activity/Body weight}} \tag{2.11}$$

If activity is uniformly distributed in the body, the measured SUV would therefore be equal to one. Physicians can use different thresholds of SUV as a guide to help determine whether a tumour may be malignant but this relationship is not

exact and may be highly influenced by noise. The change in tumour SUV after treatment may be a useful indicator of treatment response [31].

2.2.2 Annihilation Coincidence Detection

In a PET scanner, a ring of scintillation detectors with associated electronics surrounds the patient, allowing annihilation photons to be detected simultaneously. Each detected photon is time stamped, which allows the two photons detected within a short timing window to be considered coincident. This is the key technological component that significantly boosts the sensitivity of PET imaging, compared to single photon nuclear medicine (i.e. planar and SPECT imaging), as it removed the need for physical collimation of single photons to determine their angles of incidence. For this reason, coincidence detection circuitry is sometimes referred to as electronic collimation [4]. Timing windows used by commercial PET scanners are typically on the order of a few nanoseconds. A diagram of coincidence detection circuitry is shown in figure 2.7. A line can then be drawn between the two detectors which contains the positron annihilation event. This is referred to as a *line of response* (LOR) [1].

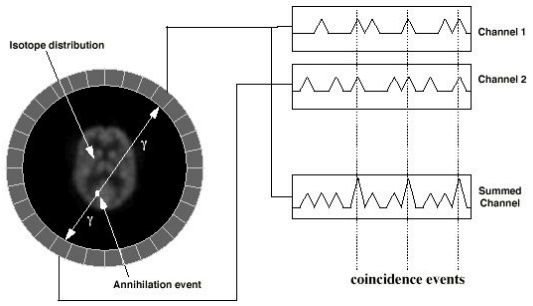

Figure 2.7: **Coincidence Detection of Annihilation Photons:** . Adapted from Badawi [4].

In conventional PET imaging, the probability density of each positron annihilation event is considered to be evenly distributed along the LORs. *Time-of-flight* (TOF) PET imaging improves upon this by using greater timing resolution. In principle, the difference in time of arrival of the two annihilation photons (and their speed, c) should allow precise determination of the position of the annihilation event. This would also make PET an inherently tomographic imaging modality,

[1] The so-called line of response is actually a rectangular tube with side dimensions equal to that of the detectors.

rendering reconstruction unnecessary. The relevant length of the LOR, Δx is related to the timing resolution, Δt, by:

$$\Delta x = \frac{c}{2}\Delta t \tag{2.12}$$

However, it would require timing resolution on the order of 30 ps to determine the location of the annihilation event within 1 cm. Commercial PET scanners currently have timing resolutions of $\sim$ 500 ps, allowing the LOR to be restricted to several cm. As shown in figure 2.8 the probability of an annihilation event is typically modelled using a Gaussian kernel in TOF PET.

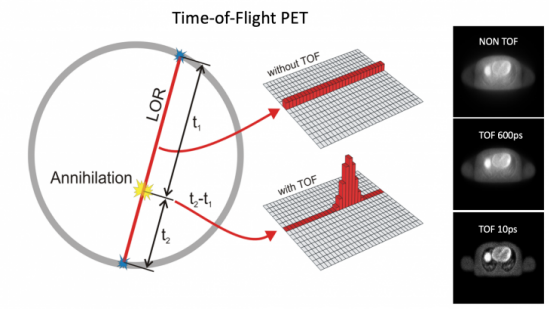

Figure 2.8: **Time-of-flight PET:** . Adapted from Lecoq [5].

2.2.3 Scintillator Detectors

In PET, the annihilation photons produced from a decaying positron emitter are typically detected using scintillator-based detectors. A scintillator is a material that produces visible light when irradiated with high energy photons. As the photons lose energy through the photoelectric, pair production, and Compton processes discussed in section 1.1.2, the ejected electrons cause excitations that ultimately result in the emission of light in the visible to ultraviolet spectrum. The scintillation photons are then detected by a photomultiplier tube (PMT) or silicon photomultipliers (SiPM). Characteristics that are desirable in scintillators include: conversion efficiency of high energy photons into visible light, short decay times (phosphorescence or afterglow), transparent to generated scintillation light, high detection efficiency, as well as durable and inexpensive. The characteristics of some commonly used scintillator materials are shown in table 2.1. Bismuth germanate (BGO) based detectors were the most frequently used until recently when lutetium based detectors (LSO and LYSO) have become more common.

Material	Density (g/cm^3)	Effective Atomic No.	Light Output Relative to NaI	Phosphorescent Decay Time (μs)
Sodium iodide (NaI(T1)	3.67	46	1	0.23
Lanthanum bromide ($LaBr_3$:Ce)	5.3	47	1.6	0.025
Bismuth germinate or BGO ($Bi_4Ge_3O_{16}$)	7.13	74	0.15	0.3
Lutetium oxyorthosilicate or LSO (Lu_2SiO_4O)	7.4	66	75	0.04

Table 2.1: **Characteristics of Common Scintillators Used in Nuclear Medicine:** adapted from Chandra and Rahmim (2018)

The amount of light emitted by the scintillator is proportional to the energy of the incident photon, allowing for energy discrimination using pulse height analysis. In PET an energy window centered on 511 keV is set (425-650 keV is a typical energy window). The dimensions of the scintillator crystals are one of the factors in determining spatial resolution. Rectangular dimensions of 4-5 mm are typical with a depth of 15-25 mm to generate acceptable detection efficiencies.

2.2.4 Sources of Image Degradation in PET

There are several factors that contribute to image degradation. Detection of random coincidences, positron range, and photon non-collinearity are all sources of error unique to PET. Accounting and, when possible, correcting for the following is necessary to obtain images of high quality:

- Annihilation photon attenuation
- Scatter coincidence detection
- Random coincidence detection
- Non-uniformity of detector sensitivity
- Positron range
- Photon noncollinearity
- Inter-crystal scattering
- Detector dead time

Attenuation Correction: As the 511 keV annihilation photons travel towards detector pairs they are attenuated by different tissues, determining the probability of detection according to:

$$P = e^{-\sum_{i=0}^{n} \mu_i D_i} \tag{2.13}$$

where μ_i and D_i are the linear attenuation coefficients and lengths of each tissue along the LOR, respectively. This suggests that patients with larger cross sections, or tissues with higher attenuation of 511 keV photons will result in under estimation of the activity concentration unless attenuation is quantitatively accounted for. Determining the attenuation factors with either (i) transmission scans, or (ii) X-ray CT, allows for such attenuation correction [7]. To obtain transmission scans, a PET scan is first acquired with no patient while a uniform rod ^{68}Ge source is rotated around the gantry so that each detector pair is irradiated. This process is then repeated with the patient in the scanner. The ratio of measured counts from the two scans allows for a correction factor for each LOR (or detector pair). Historically, this method was used before it was common to integrate PET and CT scanners into a single combined unit. The preferred method is to directly determine the linear attenuation coefficients for each pixel by acquiring an x-ray CT image.

In addition to true coincidences, figure 2.9 illustrates two other possibilities: scattered and random coincidences. *Scattered coincidences* are detected when one or both annihilation photons undergo scattering events (Rayleigh or Compton) before reaching the detector. This results in the displacement of the LOR from the actual source of the annihilation event. Some scattered coincidences can be filtered out when energy discrimination is applied but many of these scattering events result in detected events within the energy window. It is common for the fraction of detected counts due to scatter to be greater than 40% for 3D PET [7]. A variety of corrections for scattered coincidences exist, including modeling scatter counts using Monte Carlo simulations and subtracting from the measured counts.

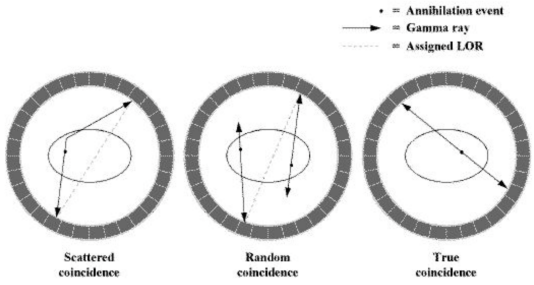

Figure 2.9: **Types of Coincidences in PET:** . Adapted from Badawi (1999).

Random coincidences are detected when two photons from different sources

arrive at the detectors within the timing window and are incorrectly attributed to the same annihilation event. The rate of randoms coincidences can be estimated and corrected for by (i) using a delayed coincidence window, or (ii) using the singles count rates of each detector pair [32]. By using a delayed or offset timing window, two events which cannot be true coincidences are considered coincident. This gives an estimate of the rate of random events being detected. Alternatively, the rate of random events for a pair of detectors (A and B) is described by [7]:

$$R_{random} = \Delta T \cdot R_{single\,A} \cdot R_{single\,B} \tag{2.14}$$

where R_{single} is the count rate of each detector and ΔT is the timing coincidence window. The random rate for each LOR can then be directly measured and subtracted from the total count rate, or incorporated directly within the image reconstruction.

Normalization: The sensitivity of each detector pair in a field of view (FOV) can vary for a few reasons, including the sensitivity and gain of each individual detector and the angle of a LOR relative to the surface of a scintillator crystal. These non-uniformities can be measured and corrected for by exposing each detector pair to a uniform source (similar to the transmission method of attenuation correction), a process which requires a long scan duration to accumulate sufficient counts. It is common to supplement this process by modeling the physical characteristics of each component, including intrinsic and geometric detection efficiency.

Resolution Modeling: In addition to the physical dimensions of the detector, there are three factors that degrade the resolution of PET: positron range, photon noncollinearity, and inter-crystal blurring. As discussed in section 2.1.2, positron range imposes an isotope dependent limit on spatial resolution. For radiopharmaceuticals labeled with ^{18}F this results in an average resolution degradation of $\sim$0.2 mm [27]. When a positron comes to the end of its range, it may retain a small amount of kinetic energy. This results in annihilation photons escaping with an angle that deviates from 180 degrees. Similar to scattered coincidences, noncollinearity causes the LOR to be displaced from the annihilation event. Inter-crystal blurring occurs when an annihilation photon is detected in a neighboring crystal. This can be a result of the photon undergoing scattering events in the scintillator crystal, or the photon entering the crystal at an angle allowing it to pass into the neighboring crystal before detection. The latter happens frequently as the source of annihilation photons moves radially from the center of the FOV, resulting in spatially variant resolution. The resolution degradation caused by these three sources can

be estimated by scanning or simulating a point source throughout the field-of-view (FOV). The blurring can then be corrected for in the system matrix of an iterative reconstruction method. This process is referred to as point spread function (PSF) or resolution modeling [33].

Detector dead time: After an annihilation photon is detected there is a brief processing time referred to as *dead time* when additional events cannot be recorded. For high activities this poses a serious problem as it leads to missing a significant fraction of true counts. Dead time can be minimized by using fast electronics and choosing scintillators with short decay times and can also be corrected for using paralyzable and non-paralyzable models.

2.2.5 Performance of PET Scanners

The performance characteristics of PET scanners are measured routinely to verify the consistency of image quality. Part of this routine includes the daily scanning of a ^{68}Ge filled hollow cylindrical phantom and the quarterly scanning of a uniform phantom filled with ^{18}F. These phantom scans allow for the sensitivity of each detector to be measured in counts per second normalized by the activity (cps/kBq).

Another characteristic of a PET system that informs clinical scanning protocols is the noise equivalent count rate (NECR). As injected activity is increased the rate of true and scatter counts increases linearly, but the randoms rate increases quadratically (the randoms rate increases with the product of the singles rates as shown in equation 2.14). As discussed in section 1.2.4, these scattered and random coincidences can be corrected for, but they still contribute to the statistical noise in an image. NECR can be expressed as:

$$NECR = \frac{T^2}{(T + S + (k)R)} \tag{2.15}$$

where T is the true count rate, S is the rate of scattered coincidences, R is the randoms rate, and k is a factor between 1 and 2 that depends on the randoms estimation method. k is set to 1 when the randoms estimation method is noiseless, and set to 2 when a delayed coincidence window is used. The NECR is particularly important because it implies that at high levels of injected activity, the noise introduced by random coincidences degrades the image quality of the collected data beyond the benefit of the increased true count rate. Therefore the goal should be to injected activity levels that remain at or below the NECR peak shown in figure 2.10. The range of activity concentration where an increase in injected activity would

result in greater NECR (i.e. less than 40 kBq/cc in figure 2.10) is often referred to as the linear region. The exact shape of the NECR curve depends on the properties of the scanner as well as the patient being scanned.

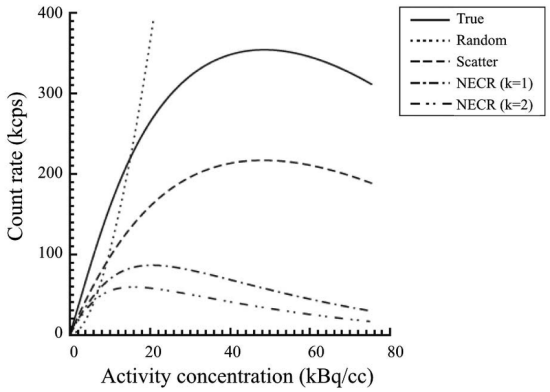

Figure 2.10: **Noise Equivalent Count Rate:** A sample NECR curve obtained using a NEMA Image Quality Phantom. Adapted from Del Guerra [6].

2.3 PET Reconstruction Methods

In PET, the measured LORs are stored in sinograms, using the relative angle of the LOR and the shortest radial distance from the center of the gantry. 3D PET images can be reconstructed using filtered back projection or iterative reconstruction methods. A brief introduction to both is included here.

2.3.1 Filtered Back Projection

The most commonly used analytic reconstruction methods in PET are based on back projection. In basic back projection reconstruction, the LORs are sorted into subsets of parallel lines which form a projection. Each of these projections is then *back projected* into the image matrix, assigning the same value to each pixel (proportional to the projection value) along a given line. As shown in figure 2.11, this method results in significant artifacts. This method can be improved by implementing filtered back projection (FBP) in which the projections are Fourier transformed into frequency space, multiplied with a filter kernel, and inverse-Fourier transformed before back projecting. In FBP, it is typical to apply corrections to the projections before reconstructing.

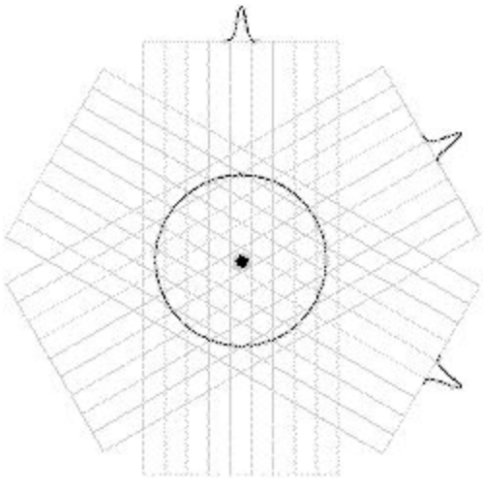

Figure 2.11: **Back Projection in PET:** Back projection results in star shaped (for low numbers of projections) or ringing artifacts (for higher number of projections) around an imaged point source. Adapted from Badawi [4].

2.3.2 Iterative Reconstruction Methods

The basic concept of iterative reconstruction methods is to begin with an estimate of a reconstructed image and to improve it through repeated processes or *iterations*. The process follows these steps: (i) start with a simplistic estimate of the image, (ii) simulate forward projections of that estimate, (iii) compare the simulated projections with the measured projections, (iv) correct the projections based on the differences, (v) back project the corrected projections, and (vi) finally use the resulting image as the starting point for the next iteration. This process is continued until the estimated projections have an acceptable level of difference from the measured projections. There are several possible methods for applying corrections but the one used in Maximum likelihood expectation maximization (MLEM) is the most common. In MLEM, the ratio of the measured counts along an LOR to the estimated counts (p_i/q_i) is used to correct the counts in each projection. The main challenge that MLEM presents are the computational resources required. When using iterative reconstruction methods, the corrections discussed above (including for scatter, randoms, TOF, and PSF) may be applied to the projections or included as part of the system matrix in the iterative reconstruction algorithm for further improvement in image quality.

Ordered subset expectation maximization (OSEM) reduces the computational burden of MLEM by sorting the projections into equally sized subsets. For example, if 32 projections were acquired by a scanner and separated into 8 subsets, each subset would contain 4 projections:
Subset 1: projections 1, 9, 17, 25

Subset 2: projections 2, 10, 18, 26

...

Subset 8: projections 8, 16, 24, 32

The standard MLEM iterative algorithm is then applied to the projections in each subset, with the resulting image from Subset 1 being used as the starting estimate for Subset 2 and so on. A single OSEM iteration with n subsets converges with the image estimate obtained by MLEM reconstruction with n iterations [34]. The optimum number of subsets depends on the total number of projections and the noise propagation through the reconstruction algorithm. More important than the choice of number of subsets is the number of iterative updates (iterations × subsets). Using a high number of iterative updates allows for higher contrast images but also increases image noise [35]. The update function for OSEM reconstruction is given by [36]:

$$\hat{f}_j^{(n,b)} = \frac{\hat{f}_j^{(n,b-1)}}{\sum_{i' \in S_b} H_{i'j}} \sum_{i \in S_b} H_{ij} \frac{p_i}{\sum_k H_{ik} \hat{f}_k^{(n,b-1)} + a_i} \tag{2.16}$$

where f is the reconstructed image, j and k are the voxel indices, n and b are the iteration and subset numbers, i and i'. are the indices of the LOR, S_b is the given subset, H is the system matrix, p is the LOR measurement, and a is the correction model for randoms and scatter.

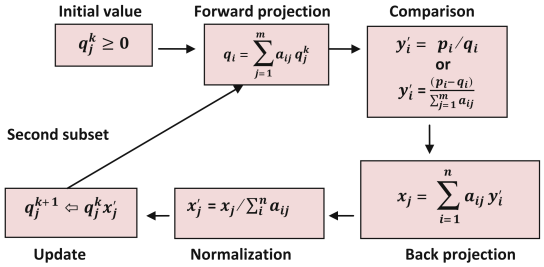

Figure 2.12: **Iterative Reconstruction:** Visual representation of the iterative reconstruction process used in OSEM. Adapted from G. Sasha [7].

In practice, the number of iterations and subsets used for OSEM reconstruction is limited by the noise level of the images, and reconstruction is stopped before full convergence. A new class of Bayesian Penalized Likelihood (BPL) algorithms were developed in order to reach full convergence (maximizing contrast) while maintaining acceptable levels of noise [37]. One such BPL algorithm, block sequential regularization maximization (BSREM), uses a single β-parameter to reduce variations between neighboring pixels while maintaining a high level of contrast at edges [38]. This has the effect of smoothing the images without the usual loss in contrast. The formula for the penalty term is given by [39]:

$$-\beta R(x) = -\beta \sum_{j=1}^{n_v} \sum_{k \in N_j} W_j W_k \frac{\left(x_j - x_k\right)^2}{x_j + x_k + \gamma \left| x_j - x_k \right|} \tag{2.17}$$

where n_v and N_j are the number of voxels and the neighbors of voxel j, w_j and w_k are local penalty weights. γ, controls the level of edge-preservation is kept constant by GE in their BSREM algorithm Q.Clear (GE Healthcare, Waukesha, WI). The effect of the BSREM algorithm, Q.Clear, on image quality will be discussed in more depth in Chapter 4.

2.4 X-ray Computed Tomography

X-ray Computed Tomography (CT) is an imaging modality that provides high resolution structural information about a patient by detecting the transmission of photons through the body. As opposed to radiography, where 2D images are obtained, CT creates a 3D image by reconstructing projections from many angles. In a CT scanner, an x-ray tube and array of detectors are positioned opposite each other on a rotational gantry. With the patient positioned in the center of the gantry, the tube and detector pair are rotated around the patient, while transmission data is recorded. Whole body CT scans can be acquired by moving the imaging couch in a step and shoot manner (axial) or by continuously translating the imaging couch during acquisition (helical). Original CT scanners used a parallel beam geometry from the x-ray tube to a flat panel detector array. The current generation of CT scanners instead use a fan beam geometry with an arc shaped detector array, as shown in figure 2.14. One advantage of this geometry is that there is very little variation in x-ray fluence to each of the detector elements.

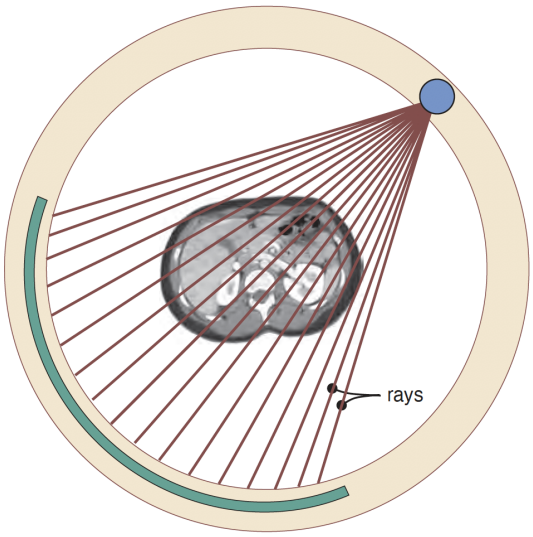

Figure 2.13: **Fan Beam Geometry of X-ray CT:** Adapted from Bushberg *et al.* [1].

After transmission through the patient, the signal measured at a detector (I_j) from an incident beam of intensity I_0 is given by:

$$I_j = I_0^{-(\mu_1 x + \mu_2 x + ... + \mu_n x)} \tag{2.18}$$

where there are n voxels traversed by the photon with a path length of x through each, and μ is the average linear attenuation coefficient of each voxel. By taking the logarithm of this equation we see that the signal is related to the sum of the linear attenuation coefficients along the path of the photon:

$$ln\left\{\frac{I_0}{I_j}\right\} = x(\mu_1 + \mu_2 + ... + \mu_n) \tag{2.19}$$

Similar to the process described for PET, projections from CT are stored in sinograms and can be reconstructed using FBP or iterative methods. Iterative methods such as the adaptive statistical iterative reconstruction (ASIR) allow for lower patient dose while maintaining diagnostic image quality [40]. The measured sinograms are first reconstructed into axial or transverse cross sections (slices) and can then be resampled to form coronal or sagittal views.

CT images are displayed in gray scale representing a special unit called Hounsfield units (HU). The HU value for a particular voxel in a patient is defined by:

$$HU(x,y,z) = 1000\frac{\mu(x,y,z)-\mu_w}{\mu_w} \tag{2.20}$$

where $\mu(x,y,z)$ is the mean linear attenuation coefficient in the voxel, and μ_w is the linear attenuation coefficient of water. This means that if the measured voxel contains only water, the numerator is zero, and the HU for water will be zero. Also, because the linear attenuation coefficient for air is essentially zero, the HU for air is -1000. The HU scale is determined by fixing just these two points.

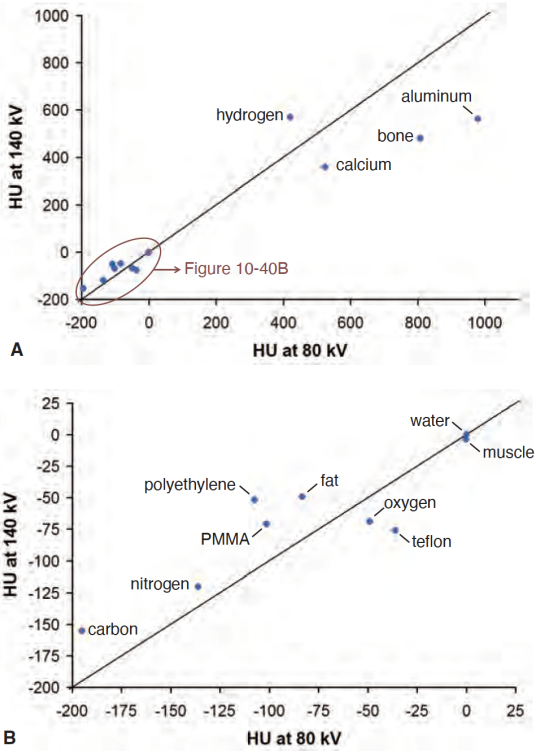

Figure 2.14: HU values for several materials at two x-ray energies. Note that water is fixed at 0 for both energies. Adapted from Bushberg *et al.* [1].

2.4.1 Applications of X-ray CT

CT is widely used for diagnostic imaging. The high spatial resolution of CT allows for detection of small abnormalities in tissue density which may be indicative of disease, including cancer. In addition to using CT to diagnose cancer, CT images are also used in the treatment planning process of radiotherapy. The planning tar-

get volume (PTV) to be irradiated is drawn on the CT data set, and the measured linear attenuation coefficients can be used to calculate the dose that will be delivered to each voxel. CT can also be fused with other imaging modalities, such as PET. Notably, CT provides attenuation correction factors for PET as well as supplementing the functional imaging with anatomical information.

2.4.2 Production of X-rays

The photons used for CT imaging are generated using an x-ray tube. The basic elements of an x-ray tube include: a source of electrons (cathode), a target (anode), a high voltage source to create a potential difference, and an evacuated chamber. These elements are depicted in figure 2.15. The cathode consists of a thin filament (typically made of tungsten) to which a current is applied. The applied current is sufficient to liberate electrons from the material, a process called *thermionic emission*. Then, when the high voltage (kV) is applied between the cathode and anode, the freed electrons are accelerated towards the target. The flow of liberated electrons from the cathode to the anode is called the *tube current* and measured in mA.

The x-rays are generated when the accelerated electrons interact with the tungsten target, producing x-rays predominantly through bremsstrahlung radiation. The maximum or peak energy that can be produced through this process is equal to the high voltage applied and is referred to as kVp. This process is very inefficient for the energy range used in CT imaging (on the order of 100 kV) converting only ~0.9% of the energy of the electrons into x-rays. The majority of the energy is wasted as heat, which poses a significant engineering challenge to cool x-ray tubes for clinical use.

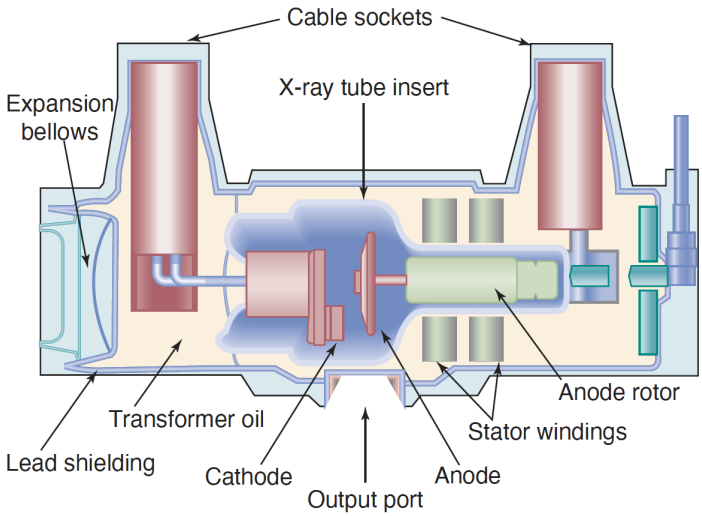

Figure 2.15: **Components of an X-ray Tube:** Adapted from Bushberg *et al.* [1].

The applied high voltage, tube current, and exposure time (kV, mA, s) are the parameters commonly reported to represent x-ray beam quality. As the generated x-rays exit the vacuum tube, they may also be filtered by thin sheets of metal (often aluminum or copper) to change the energy spectrum of the beam.

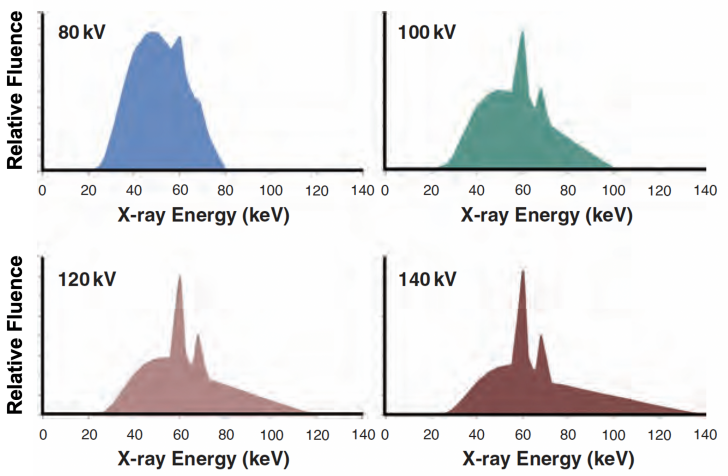

Figure 2.16: **Energy Spectra of X-ray Tubes:** Relative x-ray fluence for different peak energies (each spectra normalized independently). Adapted from Bushberg *et al.*[1].

2.4.3 Scintillator Detectors

As in PET, modern CT scanners employ scintillator based detectors. The scintillator, commonly gadolinium orthosilicate (GSO) is coupled to a photodiode for detection [41]. Lutetium based detectors are poor scintillators for CT because of their long afterglow and the high count rates present in x-ray imaging. The detector elements also have much smaller dimensions than PET detectors, yielding spatial resolutions on the order of 0.5 mm.

2.5 Image Quality

When characterizing the quality of medical images, it is common to use metrics for both *noise* and *bias*. Noise refers to the texture of an image and the variations between neighboring pixels, impacting the ability of a physician to visually interpret an image. Bias on the other hand, measures the deviation of a pixel or ROI from a known true value. Imaging systems with low bias represent an increase in quantitation. It is usually the case that the improvement of one metric (noise or bias) comes at the expense of the other. There are many ways to define these metrics for both PET and CT imaging, and a few of them that will be used in this thesis are presented in this section.

In PET imaging, one of the most frequently used metrics to quantify noise is coefficient of variation (COV). COV is defined as:

$$COV = \frac{SD}{mean} \tag{2.21}$$

where SD is the standard deviation of the pixel values in an ROI and is normalized by the $mean$ pixel value of the ROI. Alternatively, the SD can represent the standard deviation of several ROIs or noise realization and $mean$ would be the average, respectively. Both definitions will be used in this thesis.

Bias in a PET image can be defined as:

$$Bias = \frac{a}{a_{true}} - 1 \tag{2.22}$$

where a is the measured activity concentration in an ROI and a_{true} is the true activity concentration in the same region. Therefore, if a is greater than a_{true}, the bias will be positive and if a is less than a_{true}, bias will be negative. The magnitude of the bias is dependent on the size of the object/lesion detected as well as the spatial resolution and noise properties of the system. A problem known as the partial

volume effect (PVE) arises from activity spilling over into neighboring voxels at the edge of a high activity concentration region. This results in blurred edges and reduced measured activity concentrations for small objects/lesions. Determination of bias requires knowledge of a ground truth, which is very difficult to obtain for patient images. PET images of phantoms prepared with known activity concentrations provide a solution. Typically, a phantom is prepared with simulated lesions of varying diameter so that the impact of the PVE on bias can be quantified.

In order to evaluate the spatial resolution of an imaging system, including PET and CT, the modulation transfer function (MTF) can be characterized. The MTF is a measure of contrast degradation as a function of spatial frequency. It is difficult to directly measure the MTF, so typically an edge or slit with high contrast between two materials is imaged to obtain an oversampled edge spread function (ESF) or line spread function (LSF). The LSF is then fourier-transformed to obtain the MTF [42]. Alternatively, in a method developed by Droege, the MTF can be measured for several different spatial frequencies by imaging a phantom with bar patterns with varying thicknesses. Regions of interest (ROIs) can be drawn in each of the bar patterns and used to calculate the ratio of the standard deviation to the contrast between the two materials [8]. A comparison of the methods to calculate MTF are shown in figure 2.17.

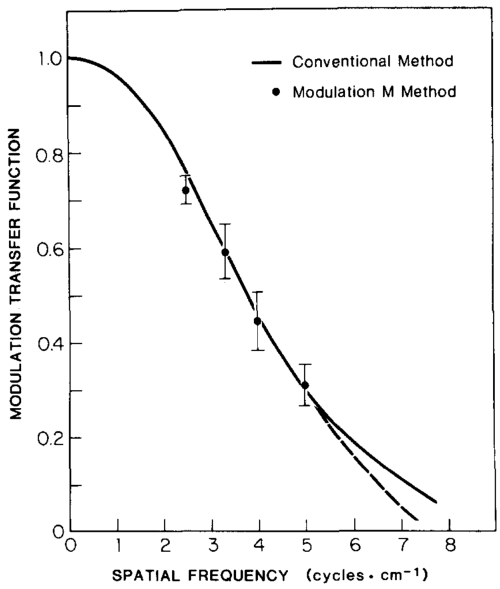

Figure 2.17: **Modulation Transfer Function:** the conventional method is determined by imaging an edge, while the *modulation* method requires measuring the standard deviation of pixels in an ROI. Adapted from Droege [8].

Another method for assessing the image quality of a CT scanner is to estimate the low contrast detectability (LCD). For large anatomical features in a CT image, it may be relatively easy to resolve two features even at low levels of contrast. However, as objects of interest get smaller (micro tumours, for example) higher contrast is needed in order to accurately detect them. By analyzing the noise characteristics in an image of a uniform object, it is possible to estimate the minimum contrast to resolve an object as a function of object size. In the method described by Shin, grids of ROIs are placed in an axial slice of a uniform water phantom. The standard deviation of the means of the ROIs is then calculated. Assuming the means are normally distributed, the standard error can be multiplied by 3.29 to obtain the minimum contrast required for detectability at the 95% confidence level [43].

Chapter 3

Automated CT QA Analysis

3.1 Introduction

The CT system integrated into the PET/CT scanners in BC Cancer can be used as a simulator for radiotherapy treatment (RT) planning in addition to providing attenuation correction factors for PET. In order to achieve high quality quantitative x-ray Computed Tomography (CT) images for both RT simulation purposes and attenuation correction in PET, it is imperative to have a robust quality assurance (QA) program. Quality assurance includes verification of the accuracy and constancy of radiographic images. A robust QA program includes end to end testing of the imaging system, from positioning on the imaging couch to the reconstruction and analysis of the obtained images. The nuclear medicine physicists at BC Cancer, Arman Rahmim and Carlos Uribe, recently worked with the Canadian Partnership for Quality Radiotherapy (CPQR) to draft Technical Quality Control Guidelines for use of PET/CT in Radiation Treatment Planning. The QA methods described in this chapter, are part of an effort to bring our centre in compliance with the proposed guidelines in an efficient manner. The components of a CT system equipped for RT simulation include accessories not routinely used in diagnostic imaging such as a movable laser alignment system, flatbed couch and respiratory gating system. The QA of these RT-specific accessories was outside the scope automated analysis procedure developed here.

The Discovery MI Digital PET/CT (GE Healthcare, Waukesha, WI) scanner installed at BC Cancer Vancouver Island Center is equipped with a Performix 40 Plus X-ray Tube and Clarity Detector with 0.28mm spatial resolution [9]. Part of the QA

program recommended by GE for this scanner is the daily scanning of the water filled QA Phantom [44]. After scanning the phantom, the PET technologists must complete manual image analysis using a suite of tools provided by GE and fill out a daily QA worksheet. The purpose of the work outlined in this chapter was to automate this manual process, taking the burden off of the technologists and implementing a more robust analysis procedure that is less dependent on the user. To this end, an automated analysis software package was developed in Python to automatically analyze the DICOM images obtained by scanning the QA phantom and report the results. In addition, the nuclear medicine physicists overseeing the QA of this centre are based in Vancouver. It is important to be able to easily track the performance of the scanner from a centralized location. The software automatically logs the data to the centralized QATrack+ server, making it simpler to audit scanner performance from a distance.

3.2 Materials & Methods

The QA Phantom used for the daily CT QA is a cylinder with two sections. The first section consists of a Plexiglass frame containing acrylic, water, and air filled cavities. This section is used for High Contrast Resolution, Contrast Scale, Slice Thickness, and Laser Accuracy tests. The second section is a uniform water filled cylinder, used to perform Noise and Uniformity, and Low Contrast Detectability tests.

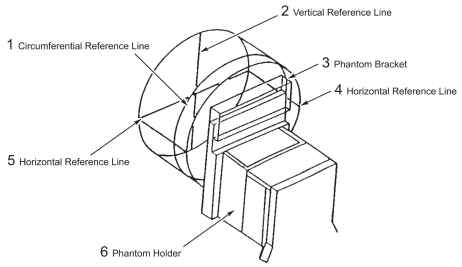

Figure 3.1: Schematic of QA Phantom including positioning bracket [9].

Before daily scanning of patients, the PET technologists perform QA tests on both the CT and PET imaging modalities. The CT QA procedure involves X-ray tube warm-up and the scanning of the QA water phantom. The water phantom is placed on the patient scanning couch and aligned with the setup lasers. The phantom attaches to the scanning bed via a custom mount such that there can be

no lateral movement of the phantom. The circumferential line separating section 1 of the phantom is used to align with the axial lasers while the horizontal and vertical markers aligned with the horizontal and saggittal lasers.

3.2.1 Automated Analysis Software

The purpose of the software outlined here is to fully automate the entire image analysis procedure. The software is given a directory containing several CT reconstructions and then locates the appropriate DICOM images for analysis utilizing a standardized folder hierarchy and data extracted from the DICOM headers. In order to analyze the water phantom images, the voxel data is extracted from the DICOM images using the Python package, pydicom, and corrected with the slope and intercept information from the DICOM header to obtain matrices containing CT number data in Hounsfield Units [45]. The following packages were also used for analysis and graphical presentation of the data: numpy, pandas, and Matplotlib [46][47][48]. The following sub sections give a high level overview of each of the analysis algorithms.

Test 1: High Contrast Spatial Resolution

The first section of the phantom contains six bar patterns (equally spaced water filled cavities) of varying size that can be used to evaluate high contrast spatial resolution of the imaging system. The bar patterns are oriented diagonally and include the following sizes: 1.6, 1.3, 1.0, 0.8, 0.6, and 0.5mm. During the manual QA analysis, the bar patterns in the Bone reconstruction are visually inspected to determine the smallest resolvable bar size. This software package instead provides quantitative analysis by placing rectangular regions of interest (ROIs) on each of the bar patterns in the Standard reconstruction and measures the standard deviation of the voxels contained. Based on the specifications of the manufacturer, the standard deviation of the 1.6 mm bar pattern should fall within 37 ± 4 HU. The four largest bar patterns (1.6, 1.3, 1.0, and 0.8 mm) are measured and recorded by the automated analysis software. Baseline values for the three smaller measured bar patterns can be set from scans of the phantom acquired during acceptance of the scanner.

In addition to comparing the measured standard deviation of the bar patterns to the accepted values, this data can be used to estimate the MTF that characterizes the spatial resolution of the system. In order to calculate the MTF, the method de-

veloped by Droege and Morin was used [8]. The MTF was also set to 1 for a spatial frequency of 0 line pairs per cm.

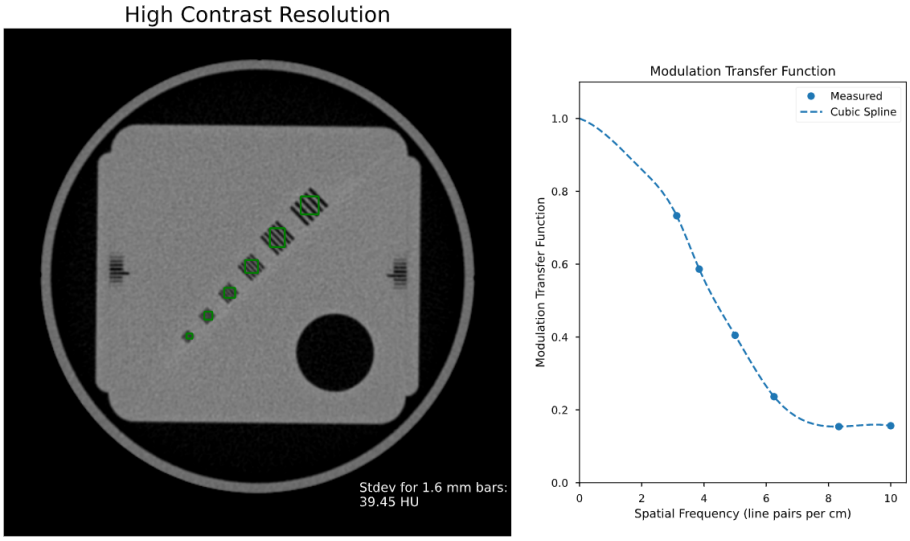

Figure 3.2: ROIs used to determine high contrast resolution and the measured MTF fit with a cubic spline.

Test 2: Contrast Scale

The contrast scale accuracy and constancy for this system is tracked over time by measuring the difference in CT numbers of Plexiglass and water. The first section of the water phantom contains uniform Plexiglass regions and a large water filled cavity which are used for CT number measurements. The developed software places rectangular ROIs with an area of 70mm^2 in each region and measures the mean CT number of the contained voxels. The contrast scale is then determined by taking the difference of the means of the Plexiglass and water ROIs. The measured contrast scale is compared to the manufacturer recommended value of 120 ± 12 HU.

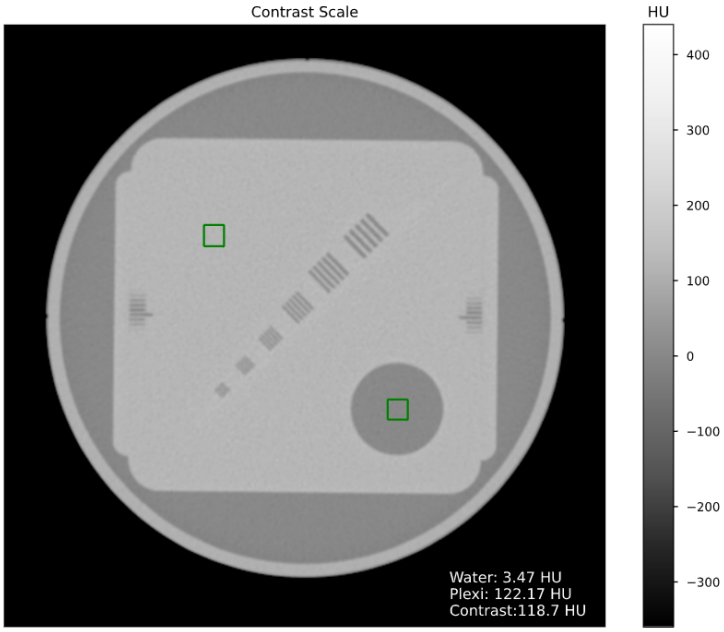

Figure 3.3: CT slice showing rectangular ROIs used to calculate contrast scale. The lower right ROI shown is placed in water, and the upper left ROI is in plastic.

Test 3: Slice Thickness

Slice thickness accuracy and constancy is determined using the horizontal bar patterns on both sides of the phantom in the first section as shown in figure 3.4. GE recommends that operators visually inspect the bar patterns with prescribed window and level settings for each slice thickness. The operator should then determine the number of discernible black or grey lines (black and grey lines corresponding with 1mm and 0.5mm of slice thickness respectively). This is an example of an analysis test that is subjective and the results could vary with user, depending on whether a line was perceived to be black or grey. To quantitatively assess slice thickness, the automated analysis software examines profiles perpendicular to the horizontal bar patterns on either side of the phantom and counts the number of minima. Each local minimum represents either 1mm or 0.5mm of slice thickness, depending on the CT number of the minimum. GE recommends different window and level settings for each slice thickness [44]. These recommendations were used as a basis for setting thresholds for 0.5mm or 1mm of nominal thickness. The slice thickness is calculated from the left and right profiles and averaged to obtain a nominal slice thickness for each reconstruction. The detected minima of the pro-

files is shown in figure 3.4.

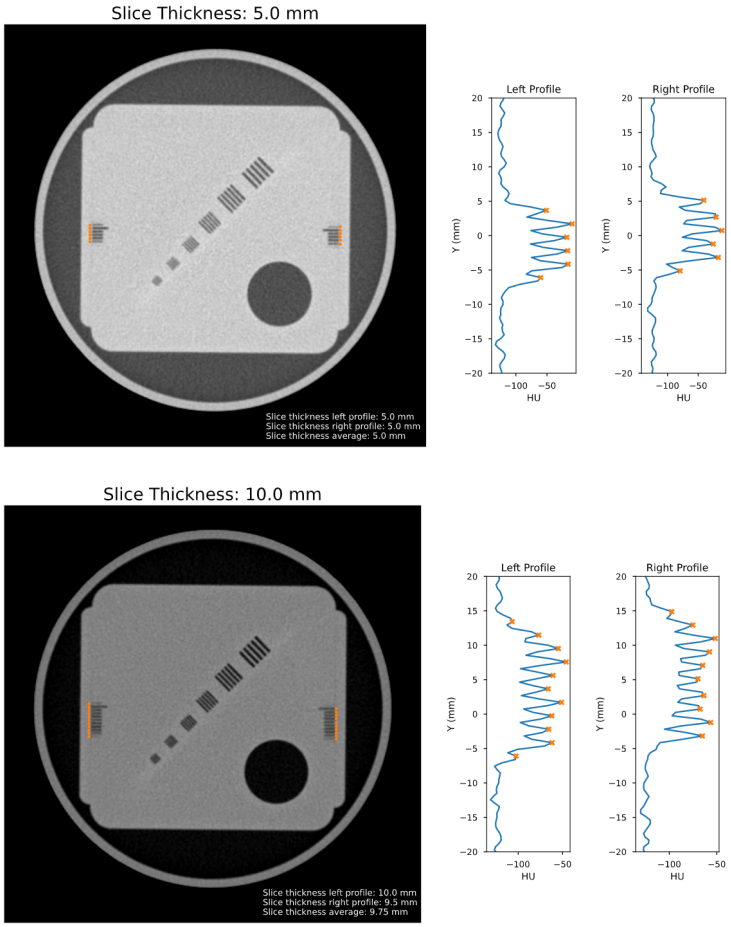

Figure 3.4: CT reconstructions of two different slice thicknesses (5.0, and 10.0 mm) and the corresponding profiles used to verify slice thickness.

Test 4: Alignment Light Accuracy

The Alignment Light Accuracy test is designed to ensure that the reference lasers are aligned with the scanner coordinate system within specification. In addition to the etched markers on the top and side of the phantom, there are drilled holes in the same respective planes which are visible on the CT image. During manual assessment, the operator would place a graticule at the center of the image and measure the offset of the top and side marker from their respective axes (AP or LR). The automated analysis software accomplishes this by measuring profiles across

the top and side edges of the QA Phantom. Example profiles are displayed in figure 3.5.

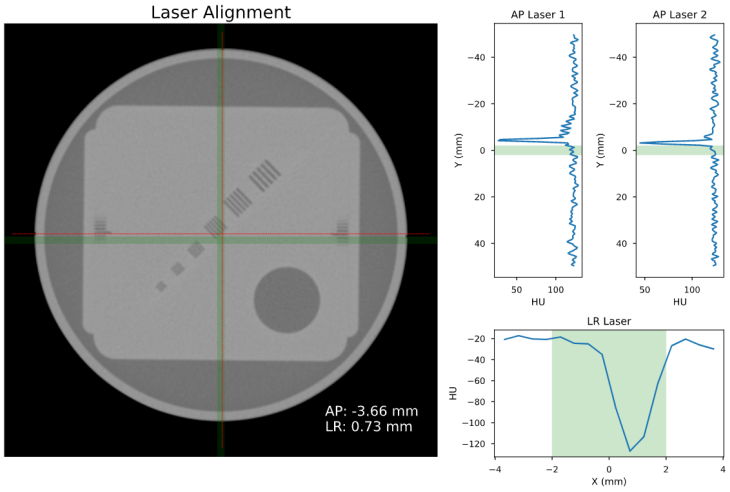

Figure 3.5: Profile across top of the CT phantom. The minimum indicates the position of the drilled hole which corresponds to the etched laser alignment mark.

The drilled hole is detected by determining the location of the local minimum in each of these profiles. This location is then compared to the center of the image matrix. Using the nominal voxel dimensions, the absolute magnitude of the offset from the scanner isocenter to the setup laser isocenter is determined and reported in mm. The alignment light is expected to agree with the scanner coordinate system within ± 2.0mm. The results of the laser alignment test are also used to adapt the positions of ROIs for the other QA tests. The offset of the LR and AP lasers from the center of the image matrix is applied to all ROI positions.

Test 5: Noise and Uniformity

The uniform water section is used to perform QA on the noise and uniformity of measured CT number by the scanner. Uniformity is quantified by measuring the variability of CT number in several regions of interest while image noise is quantified as the corresponding standard deviation of the same regions. 2×2 cm ROIs are placed in the center of the image and all four cardinal positions (contained in the uniform region) as shown in figure 3.6.

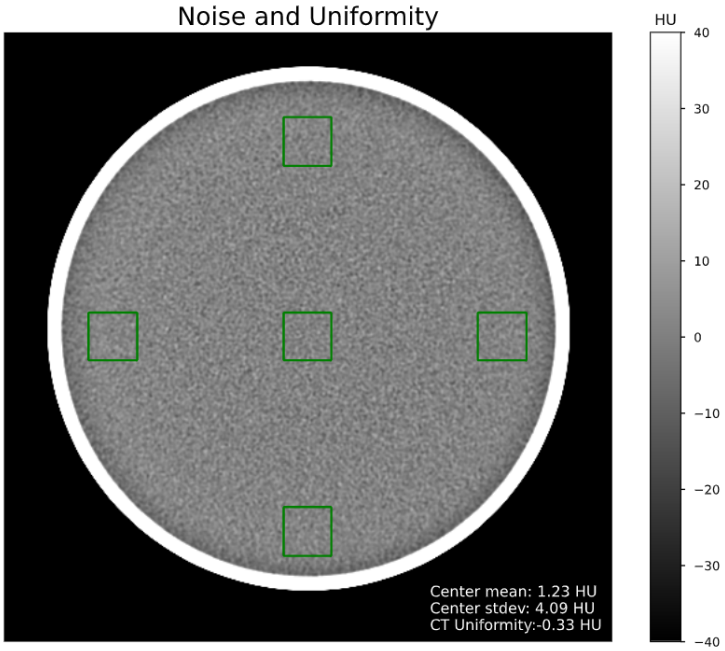

Figure 3.6: CT slice displaying central and cardinal ROIs used to determine system noise and uniformity.

The mean and standard deviation of each ROI are then determined. The uniformity is defined here as the difference between the mean CT number of the central ROI and the average of the means of the outer ROIs. The specification for both uniformity and mean CT number of the central ROI recommended by GE is 0 ± 3 HU. The recommended specification for image noise (using the standard deviation of the central ROI) is 4.3 ± 0.6 HU.

Test 6: Low Contrast Detectability

Low Contrast Detectability (LCD) refers to the ability to accurately identify low contrast objects of a given size. In the software developed, LCD was calculated using the method described by Shin [43] using statistical analysis of the uniform region in the water section of the CT phantom. The developed software places a grid of square ROIs within the uniform region with the grid spacing ranging from 3mm to 15mm in 1mm increments. An example of a 3 mm grid is shown in figure 3.7.

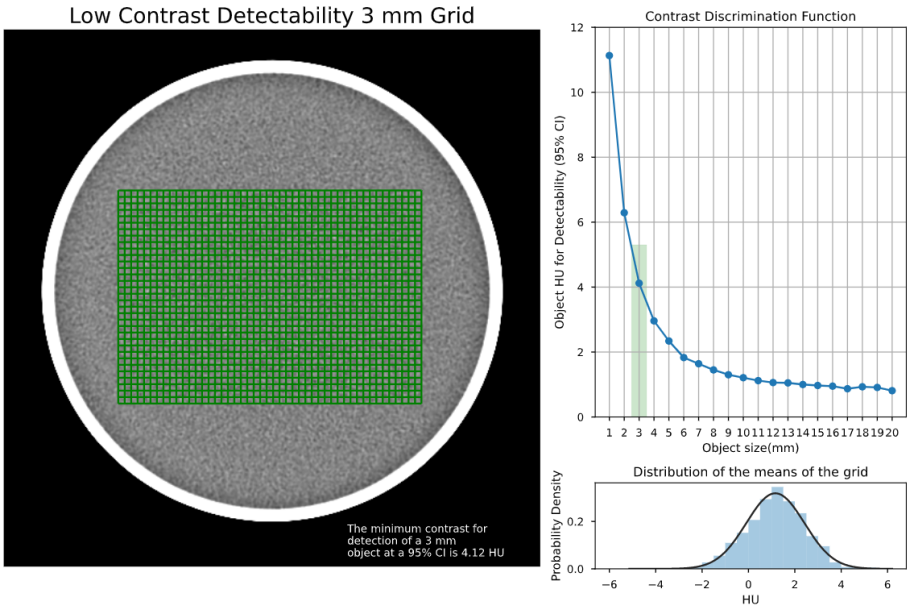

Figure 3.7: CT slice displaying 3mm grid in the uniform water region, detect-ability vs object size function, and distribution of mean HU.

For each grid size, n the software calculates the mean CT number of each $n \times n$ ROI and subsequently the mean and standard deviation of all the ROIs in the grid. The standard deviation of the mean CT numbers is used to determine the minimum detectable contrast at the 95% confidence level (by multiplying the standard deviation by 3.29)[43]. Smaller grid sizes will result in noisier ROIs and consequently higher minimum detectable contrast levels. The automated analysis software also displays the distribution of the mean CT numbers for each grid size. This allows the user to verify that the mean of the ROIs follow a normal distribution.

3.2.2 Phantom Scanning

The phantom scanning includes three image acquisitions: one for the slice thickness tests, one for laser alignment verification, and a third for the remaining tests. The following scan parameters are used for Contrast Scale, High Contrast Resolution, Noise and Uniformity, and Low Contrast Detectability:

- Thickness: 5mm
- Scan Type: Helical

- Tilt: 0°
- kV: 120
- mA: 135
- Rotation Speed: 1 second
- Pitch: 0.516:1
- Algorithm: Standard, Bone
- Matrix Size: 512

Both Standard and Bone reconstructions are made, though only the Standard reconstruction is used for quantitative analysis. See Test 1: High Contrast Spatial Resolution for more detail. The following scan parameters are used for the slice thickness tests:

- Thickness: 1.25, 2.5, 5.0, 10.0mm
- Scan Type: Axial
- Tilt: 0°
- kV: 120
- mA: 200
- Rotation Speed: 1 second
- Algorithm: Standard
- Matrix Size: 512

Reconstructions are made for each of the four slice thickness options. The following scan parameters were used for the Alignment Light Accuracy test:

- Thickness: 2.5mm
- Scan Type: Axial
- Tilt: 0°
- kV: 120

- mA: 260
- Rotation Speed: 1 second
- Algorithm: Standard
- Matrix Size: 512

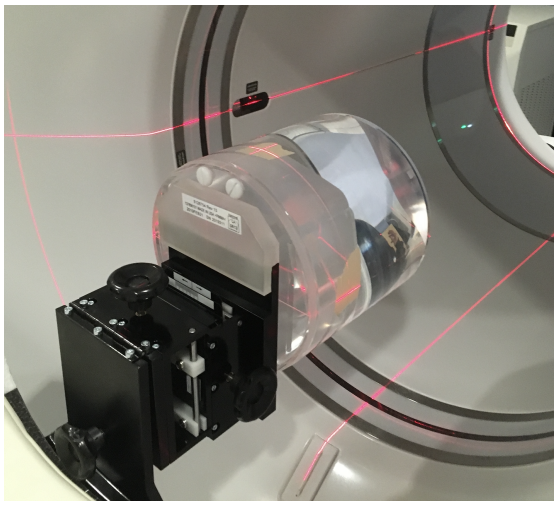

Figure 3.8: The GE CT QA phantom positioned on the scanner bed, aligned to the external lasers.

After acquiring these images, the operators then manually perform the analysis recommended by GE. This includes drawing regions of interest (ROIs), visual analysis, and some processes that are automated by GE's included software tools.

3.3 Results

The analysis software that was developed in this project was used to analyze a sample CT phantom image set acquired with the Vancouver Island Center Discovery MI PET/CT scanner. The previous figures in this chapter were generated using the software. A summary of the results of this analysis is reported in figure 3.9 (images from the same data set are shown in figures 3.2-3.7). This summary is based on the QA worksheet provided by GE that technologists manually fill out regularly.

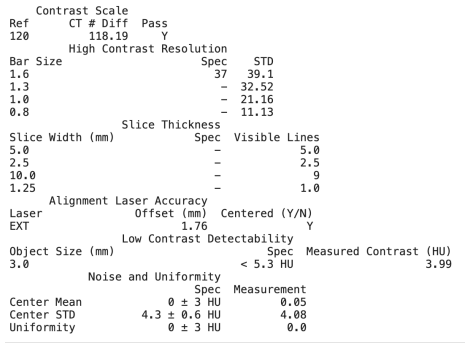

```
    Contrast Scale
Ref      CT # Diff  Pass
120         118.19     Y
         High Contrast Resolution
Bar Size                      Spec    STD
1.6                             37   39.1
1.3                              -  32.52
1.0                              -  21.16
0.8                              -  11.13
                  Slice Thickness
Slice Width (mm)             Spec  Visible Lines
5.0                             -            5.0
2.5                             -            2.5
10.0                            -              9
1.25                            -            1.0
      Alignment Laser Accuracy
Laser               Offset (mm)  Centered (Y/N)
EXT                        1.76              Y
                  Low Contrast Detectability
Object Size (mm)                        Spec  Measured Contrast (HU)
3.0                                < 5.3 HU                    3.99
           Noise and Uniformity
                              Spec  Measurement
Center Mean             0 ± 3 HU         0.05
Center STD          4.3 ± 0.6 HU         4.08
Uniformity              0 ± 3 HU          0.0
```

Figure 3.9: Example output summary of CT QA auto analysis software.

This sample data set passed all of the criteria as defined by the manufacturer. Further analysis will be possible after previously acquired daily QA data sets are analyzed with the software developed for this work. After acquisition of future daily QA scans, the images will automatically be processed using the software and the results will be sent to the QATrack+ server. This will allow physicists in Vancouver to verify the QA of the Victoria scanner just moments after the phantom is scanned.

3.4 Discussion

The daily QA program for the GE Discovery MI Digital PET/CT scanner installed at BC Cancer Vancouver Island Center includes scanning the CT QA phantom and manual analysis of the images by the PET technologists. The manual analysis of these images as recommended by GE can be adapted to a more quantitative process using the software described in this chapter. Moving to a fully automated analysis procedure presents some challenges. Some of the tests are inherently subjective, including the resolvability of bar patterns or whether a water filled region appears more gray or black at a given window and level setting. These subjective tests have been redefined in a way that is easier to quantify and should provide metrics of equal or even greater utility.

The robustness of the auto analysis software to user and image variability remains to be seen and requires testing and validation alongside the manual analysis procedure currently in place. The software is currently written in a rigid way, placing ROIs and drawing profiles in roughly the same position in the image matrix every time (offset by the results of the laser alignment test). This inflexibility means that the analysis for each test has some sensitivity to the positioning of the phantom.

For example, misalignment of the phantom with respect to the lasers could result in misleading results for the Contrast Scale and High Contrast Resolution tests which would not be confirmed by manual analysis. However, phantom placement should be quite consistent, and the software could prompt the operator to re-scan the phantom if a test is out of tolerance by a specified threshold. Future versions of this software could employ machine learning techniques to place the ROIs in the optimum positions.

3.5 Conclusion

The methodology of a Python based automated analysis software for CT QA was detailed in this chapter. This automated analysis software will help to reduce the burden from technologists and allows for a repeatable, non user-dependent QA program. This software can be further improved by setting baselines for each test and reporting trends over time.

Chapter 4

Optimization of Reconstruction Parameters and Injected Activity

4.1 Introduction

[^{18}F]FDG PET is a molecular imaging modality that relies on the fact that cancer cells generally uptake and metabolize glucose at higher rates than normal tissue. [^{18}F]FDG, which is a glucose analogue, is metabolized by cancer cells in a similar way. In order to obtain a diagnostic [^{18}F]FDG PET image, patients are injected with [^{18}F]FDG, scanned , and a 3D tomographic image is reconstructed. The decisions made in each step of this process influence the quality of the resulting image. Care should be taken to choose an appropriate activity of injected radiotracer, scan duration, as well as the optimal reconstruction parameters for a given clinical task (e.g. lesion detectability, tumour quantification, etc.). Of course, it is neither ethical nor practical to inject patients with varying levels of activity in order to determine the optimum dose. Instead, phantom studies allow us to experiment with all the parameters previously mentioned and use the results to inform clinical decision making.

The National Electrical Manufacturers Association IEC Image Quality (NEMA IQ) Phantom has become a standard phantom for evaluating the performance of PET/CT scanners [49]. The European Association of Nuclear Medicine's EANM Re-

search Ltd. (EARL) has developed a procedure and set of performance standards for scanning the NEMA IQ phantom and using the results to determine the injected activity of [^{18}F]FDG for each patient that results in acceptable quantification and image quality metrics [50]. Harmonization of PET/CT scanners is important for multicentre clinical trials. Assessing the image quality of NEMA IQ phantom scans provides a standardized way to compare scanners. In addition, PET/CT centres can submit the results of their NEMA IQ phantom experiments to EARL for accreditation. This chapter expands upon the EARL procedure and it aims at optimizing the reconstruction parameters for the new state-of-the-art GE Discovery MI PET/CT scanner recently installed in the Victoria centre of BC Cancer.

4.2 Materials & Methods

To optimize the reconstruction parameters, a NEMA IQ phantom was scanned on a Discovery MI PET/CT scanner (GE Healthcare, Waukesha, WI). The details of each step of the procedure are described below. Experiments were carried out using the NEMA IQ phantom in order to optimize reconstruction parameters and determine an appropriate scan duration and injected activity for patient scanning. The procedure for this experiment was developed for inter scanner harmonization by EARL (EANM Research Ltd.) and further detailed by Koopman et al. [51][52].

4.2.1 PET Scanner

The scanner used for this work was a Discovery MI PET/CT scanner recently installed at BC Cancer in Kelowna, British Columbia. This particular scanner has the 5 ring detector option with a 25 cm axial FOV and a 70 cm transaxial FOV [53].

4.2.2 Phantom Preparation

The NEMA IQ phantom was prepared with six spherical inserts with sizes ranging from 10 to 37 mm in diameter. The spheres were filled with an activity concentration of 20 kBq/mL and a background activity concentration of 2.0 kBq/mL; defining a tumour to background ratio of 10:1. The phantom included a cylindrical lung insert, filled with foam beads (no FDG). The rationale behind the background activity concentration used comes from the assumption that a 75 kg patient administered with 300 MBq of [^{18}F]FDG and allowed 60 minutes for biological uptake should have an average whole body activity concentration of approximately

2 kBq/mL as discussed by [51]. This however, is an assumption based on a thought experiment, rather than measurements from patient data, which is further studied in chapter 5. The thought experiment suggests that after decaying over 60 minutes and 10% of the activity being lost due to excretion, the remaining activity will be uniformly distributed throughout the body and can be normalized by the patient weight.

$$300MBq \xrightarrow[60\text{ min}]{\text{Decay}} 205MBq \xrightarrow[\text{-10\%}]{\text{Excretion}} 184.5MBq \xrightarrow[75\,kg \cdot 1\,kg/L]{\text{Divide}} 2.46\,kBq/mL$$

The hepatic activity concentration in patients injected with [^{18}F]FDG has been found to be significantly higher, with an average concentration of ~5.4 kBq/mL.

A dilution filling method was used to achieve the target concentrations of [^{18}F]FDG in the spheres and background. The following procedure was used.

- First, the empty background compartment of the NEMA IQ phantom was filled with 974 mL of water (the total capacity of the phantom background is 9740 mL).
- Using the automatic activity injector available in our PET centre, which has been used to perform the well counter calibration of the scanner, 48.1 MBq were added to the volume of water from the previous step. The FDG infusion record printed from the automatic injector is shown in figure 4.1.
- To ensure that the solution was homogeneous, food coloring was then added and the radioactive solution was mixed.
- The six spheres of the phantom were filled with the prepared solution in the background compartment of the NEMA phantom.
- The cylindrical lung insert was then placed and the spheres were placed in their position. the phantom was sealed.
- Using the available filling holes on the sides of the phantom, water was added to the background solution to fill the remainder of the 9740 mL volume.
- This method ensured a 10:1 activity concentration ratio between the spheres and the background. The prepared phantom is shown in figure 4.2

The volume of the solution dispensed from the Intego (35 mL) and the the volume removed from the background compartment to fill the spheres (47.82 mL) was accounted for when calculating the activity concentrations at the time of scan acquisition.

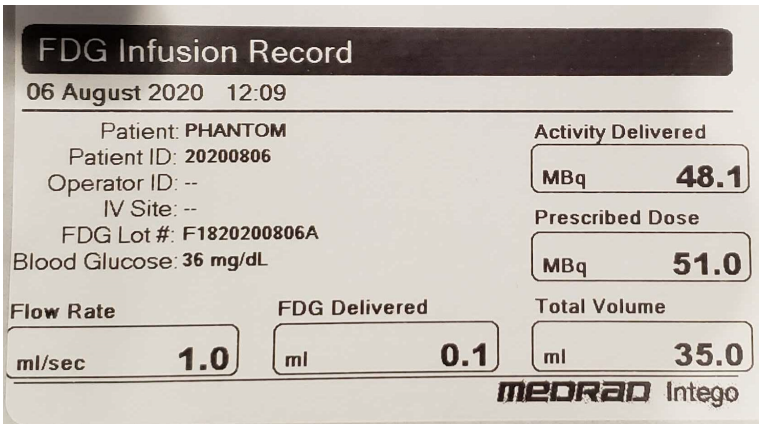

Figure 4.1: **Intego Automatic Injector:** Printed label from the Intego confirming the activity of [^{18}F]FDG dispensed into the background of the NEMA phantom.

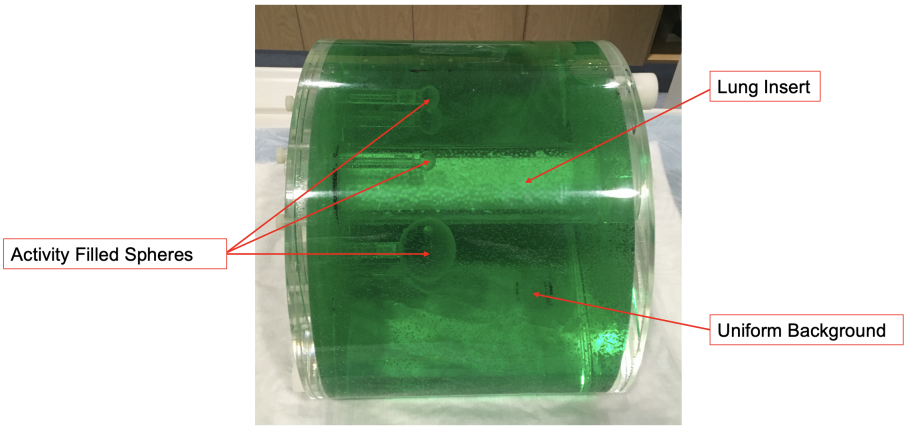

Figure 4.2: **NEMA IQ Phantom:** A side view of the prepared NEMA phantom shows the spheres, lung insert, and uniform background region filled with FDG and green dye.

4.2.3 Image Acquisition

The NEMA IQ phantom was placed on the scanner bed and positioned so that the entirety of the phantom was within the PET FOV. The phantom was oriented in such a way that the center of the spheres were coplanar in the axial plane. The position and tilt of the phantom was confirmed by acquiring a scout CT scan before collecting experimental data.

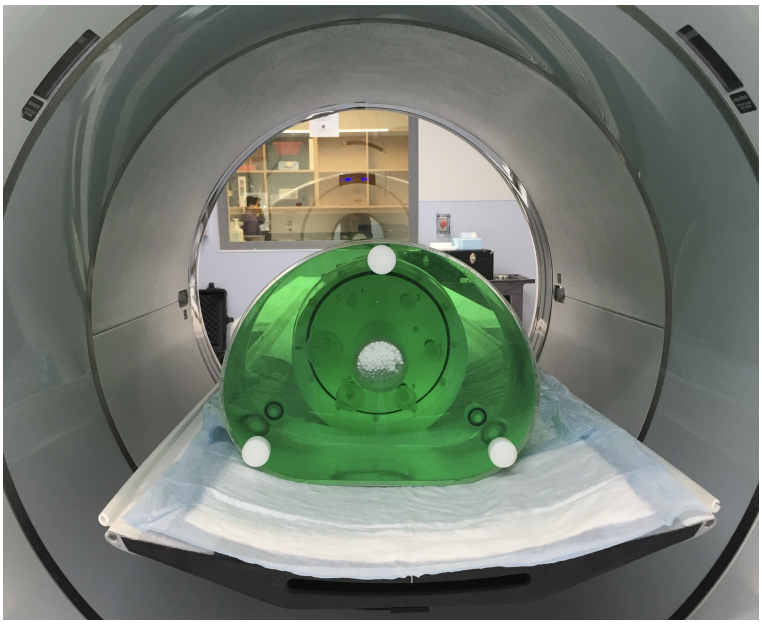

Figure 4.3: The NEMA IQ phantom is positioned on the scanner bed in preparation for image acquisition.

A CT image was then acquired for attenuation correction. The PET scan was started when the sphere and background activity concentrations were 20 and 2.0 kBq/mL, respectively (actual activity concentrations of 19.7 and 1.94 kBq/mL were calculated). This background activity concentration is consistent with the assumptions made by EARL discussed previously. PET data was acquired in list mode for 10 minutes and a single bed position. The data was then reconstructed using:

- Different reconstruction algorithms (OSEM and BSREM).
- Different reconstruction parameters (TOF, PSF, numbers of iterations and subsets, post smoothing filters.
- Re-binned different scan durations of 600, 450, 300, 150, 75, 38, and 19 seconds.

Although the original experiment design was to re-scan the phantom every hour to simulate reduced levels of injected activity, it was shown by Koopman *et al.* that changing the scan duration has an identical effect on the counting statistics [52].

4.2.4 Reconstruction Parameter Optimization

The current clinical protocol uses the OSEM algorithm with 2 iterations, 34 subsets, PSF, non TOF, and smoothed with a 6.4 mm full width half maximum (FWHM) Gaussian filter (HDS 2i 34s 6.4 mm FWHM). This reconstruction will be referred to as 'Clinical' throughout this chapter. To optimize the reconstruction parameters, the high counting statistics full 10 minute PET acquisition was used. The NEMA IQ phantom list mode data was reconstructed using the GE Duetto toolbox (version 2.07) developed in MATLAB and provided to us by the scanner manufacturer to allow off-line reconstructions. Besides the Clinical reconstruction, reconstructions were made using both OSEM and BSREM algorithms (advertised by GE under the name of Q.Clear) with various parameters. For the OSEM reconstructions, parameters investigated included TOF (on/off), PSF (on/off), number of iterations and subsets, and the FWHM of Gaussian post reconstruction smoothing. For the BSREM algorithm, TOF and PSF were left on (called QFX by GE) and the only parameter changed was the Bayesian-penalty factor, β. The decision tree used to optimize reconstruction parameters is depicted in figure 4.4. All reconstructions included in this work were made with a 192×192 matrix size with pixel dimensions of $3.65 \times 3.65 \times 2.8$ mm (x × y × z).

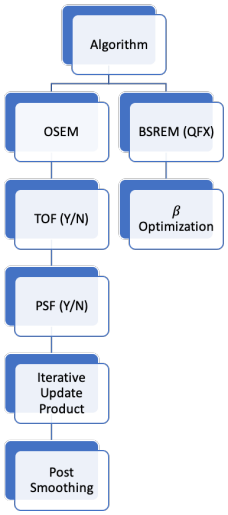

Figure 4.4: **Reconstruction Parameter Optimization Decision Tree**

4.2.5 Analysis Methods

The attenuation, randoms, and scatter corrected reconstructed PET images were analyzed using software tools developed in python [54]. In order to assess the image quality of the NEMA IQ phantom PET images, metrics for both quantification bias and noise were used.

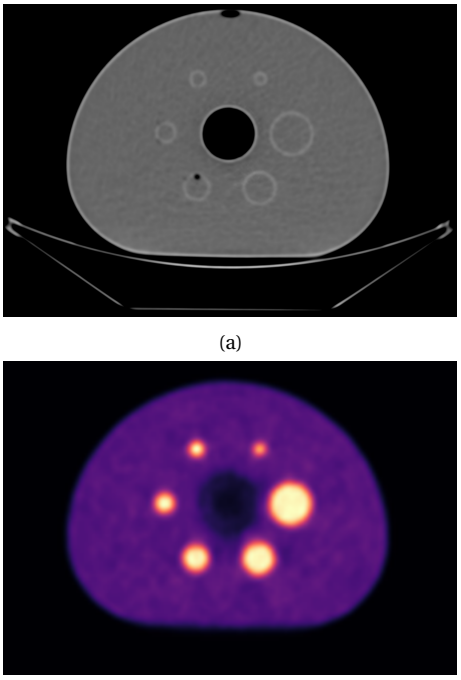

(a)

(b)

Figure 4.5: **Acquired Images**: CT used for attenuation correction (a), and reconstructed PET image using clinical parameters: non TOF, 2 iterations, 34 subsets, 6.4mm FWHM post reconstruction Gaussian smoothing (b).

Recovery Coefficients (Bias)

To determine bias, the mean, maximum, and peak recovery of each of the spheres was first calculated. Recovery coefficients (RC) were defined according to:

$$RC_{mean} = \frac{a_{mean}}{a_{true}},$$

$$RC_{max} = \frac{a_{max}}{a_{true}}, \tag{4.1}$$

$$RC_{peak} = \frac{a_{peak}}{a_{true}},$$

where a_{true} is the true decay-corrected activity concentration in the spheres at the time of the scan acquisition, and a_{mean}, a_{max}, and a_{peak} are the measured mean, maximum and peak activity concentrations in the spheres, respectively [55][51]. The mean contrast recovery (MCR) was then calculated by averaging the recovery coefficients of the six spheres [55]. Separate MCR values were calculated for mean, maximum, and peak recovery. Finally bias was quantified by subtracting MCR from one.

$$Bias_{mean} = MCR_{mean} - 1,$$

$$Bias_{max} = MCR_{max} - 1, \tag{4.2}$$

$$Bias_{peak} = MCR_{peak} - 1$$

Coefficient of Variation (Noise)

The metric used to quantify noise in the phantom images was coefficient of variation (COV). 3 cm rectangular ROIs were placed in the uniform background region of the central slice (and two adjacent slices) of phantom PET images. The mean and SD of the pixels within each of these nine ROIs were used to calculate COV according to:

$$COV = \frac{SD_{ROI}}{mean_{ROI}}. \tag{4.3}$$

The average COV of the nine ROIs was reported as the noise level for each reconstruction [51][52].

Segmentation and ROI Placement

In order to calculate the image quality metrics defined above, each of the spheres was segmented automatically, and rectangular ROIs were placed in the uniform background automatically using software tools developed in python. The Difference of Gaussian method was used to first detect each of the six spheres [56]. Then, using the true diameters of the spheres and the pixel dimensions extracted from the DICOM header, masks were generated containing all voxels within each sphere. The maximum activity concentration was determined by simply taking the pixel with the highest value in each sphere. The mean activity concentration was computed by employing a 50%, background adapted threshold approach as defined by Lodge as [57]:

$$\mathrm{VOI}_{\mathrm{isocontour}} = (a_{max} - a_{bkg}) \cdot f + a_{bkg}, \tag{4.4}$$

where a_{bkg} is the mean activity concentration in the uniform background (measured from the same ROIs used for COV analysis), and f is a fraction used for thresholding. For the analysis in this study, f was set to 50%. The $\mathrm{VOI}_{\mathrm{isocontour}}$ was used to generate a threshold segmentation mask for each sphere. The segmentation was applied and the mean of all the voxels contained in the mask was evaluated to obtain the mean activity concentration.

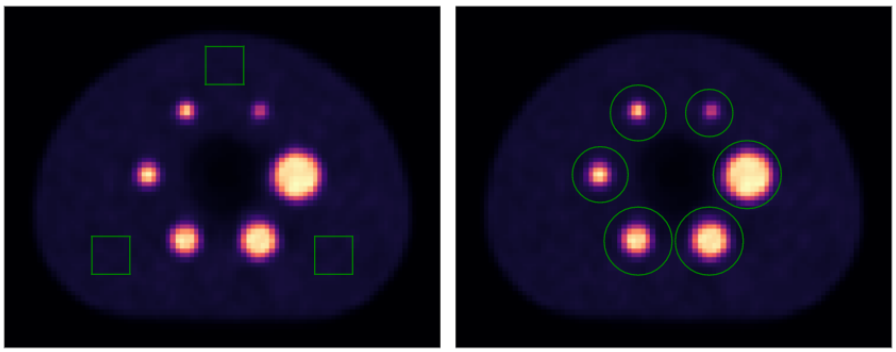

Figure 4.6: **NEMA IQ ROI Placement** Axial PET slice of NEMA IQ phantom, showing ROI placement for background COV calculation (a) and segmentation of the spheres before thresholding is applied (b).

The peak activity concentration is defined as the mean of a 1 mL VOI with the highest average activity concentration in a given structure. This metric is similar to the maximum, but less influenced by noise. In this study, peak activity concentra-

tion was calculated using a convolution of the PET image matrix with a 3D kernel with a 1 mL volume (a cube with 1 cm sides). The highest pixel values in the spheres of the convolution image were taken to be the peak activity concentrations.

To calculate background COV, the nine ROIs were placed relative to the identified center of of the largest sphere. After locating the center of the sphere with the Difference of Gaussians method, three ROIs were placed in the same slice in the arrangement shown in figure 4.6. The remaining six ROIs were placed in the two adjacent axial slices as described by EARL [51].

At each step in the decision tree in figure 4.4, parameters were chosen that minimized bias and COV according to equations 4.2 and 4.3.

4.2.6 Injected Activity Optimization

After optimizing reconstruction parameters based on the 10 minute scan, the procedure developed by Koopman et al. was followed to determine the minimum injected activity and scan duration to achieve PET images of acceptable quality [52]. The COV analysis described above is repeated for PET images re-binned for shorter scan durations. Then, by fitting the COV as a function of scan duration, it is possible to determine the minimum scan duration to maintain a certain noise threshold. Finally, the level of quantitation at the reduced scan duration is verified by calculating RCs and bias. The RC ranges suggested by EARL were considered only as a reference and a lower threshold [55][51].

Because positron emission is a Poisson distributed random process, the signal-to-noise ratio (SNR, reciprocal of COV defined above) of measured sinogram data is proportional to the square root of the product of the injected activity and the scan duration [58].

$$SNR = \frac{mean}{SD} \propto \sqrt{A \cdot t} \tag{4.5}$$

This suggests that adjusting either the injected activity, or the scan time per bed position should have a similar impact on PET image quality. Equation 4.5 also illustrates the importance of the time activity product (TAP). When specifying the scanning parameters for a patient, it is the TAP rather than just the injected activity or scan duration independently that is important in determining image quality.

For the NEMA IQ phantom experiment, different TAPs were produced by re-binning the 10 minute list mode scan for shorter frame durations. Assuming that the injected activity is in the linear region of the NECR curve, the effect is the same

as keeping a fixed scan duration and reducing the injected activity. If the phantom preparation was analogous to scanning a patient injected with 300 MBq, resampling for a 2.5 minute frame duration should result in the same image quality as injecting 150 MBq and scanning for 5 minutes. If we express equation 4.5 in terms of COV instead we see that,

$$COV = \frac{SD}{mean} \propto (A \cdot t)^{-1/2}. \tag{4.6}$$

We can use this to model the COV as a function of TAP (or just the scan duration given that we have a fixed injected activity) according to:

$$COV = a \cdot T^{-b} \tag{4.7}$$

where a and b are fit parameters. Based on equation 5.18, we would expect to find that $b = 1/2$. After obtaining these fit parameters, and choosing a COV threshold indicative of acceptable image quality, we solve for the minimum scan duration:

$$T_{min} = \left(\frac{a}{COV_{threshold}} \right)^{1/b} \tag{4.8}$$

EARL suggests a COV threshold of 15% as representative of suitable clinical image quality, but after measuring noise in patient images obtained within BC Cancer, a COV threshold of 10% was found to be more appropriate (see chapter 5). Using this COV threshold, and the injected activity (based on the activity concentration in the background of the phantom) we were able to calculate the minimum TAP for a 75 kg patient:

$$TAP_{75kg} = A_{inj} \cdot T_{min} \tag{4.9}$$

where A_{inj} is the injected activity assumed to result in a hepatic activity concentration of 2.0 kBq/mL in a 75 kg patient. Scaling the TAP to patients of different sizes is also explored in chapter 5.

4.3 Results

4.3.1 Recovery Coefficients

Reconstructions from the 10 minute sinogram made with the current clinical parameters as well as OSEM with TOF and PSF (FXS) and BSREM with TOF and PSF

(QFX) are shown in figure 4.7. While the Clinical reconstruction falls within the EARL 2 ranges given for RC_{mean}, RC_{max}, and RC_{peak}, it is clear that FXS and QFX reconstructions result in a better recovery (i.e. closer to 1), particularly for the smallest spheres, which are more affected by the PVE. FXS reconstructions were made for a variety of iterative update products (IUP) defined as:

$$\text{IUP} = \text{iterations} \times \text{subsets} \tag{4.10}$$

The IUP of FXS reconstructions ranged from 16 (2 iterations, 8 subsets) to 64 (4 iterations, 16 subsets). It can be seen that increasing IUP results in greater quantitation (higher recovery), though the returns are diminishing beyond IUP = 24. Unlike the Clinical reconstruction, the FXS and QFX reconstructions shown here do not include post reconstruction smoothing.

Increasing β results in decreased recovery, but even for the highest allowable value the mean and peak recovery of the smallest sphere is above the range defined by EARL 2.

4.3.2 Coefficient of Variation

COV values are shown for the same three reconstructions and parameter sets from figure 4.7. Here, the opposite trend can be observed: increasing IUP results in noisier images, while increasing β produces smoother images with lower COV. The low COV of the Clinical reconstruction relative to the FXS reconstructions shown is due to the high level of post reconstruction Gaussian smoothing (6.4mm FWHM).

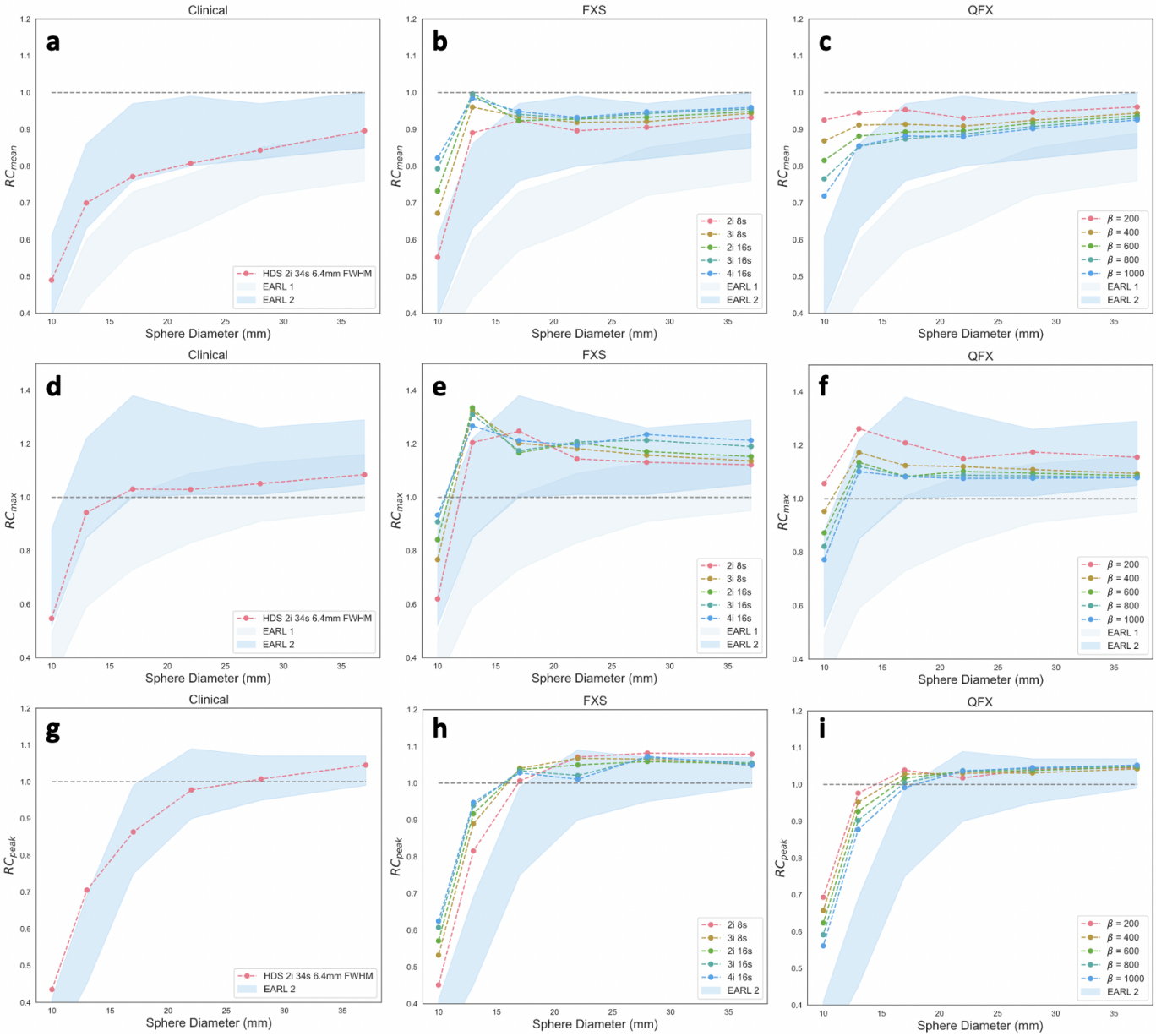

Figure 4.7: **Recovery Coefficients**: Mean, maximum, and peak recovery coefficients for the current Clinical reconstruction **(a,d,g)** as well as FXS with varying iterative update products **(b,e,h)** and QFX with varying β values **(c,f,i)**

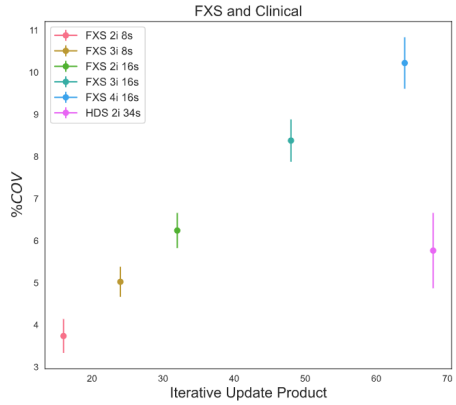

(a)

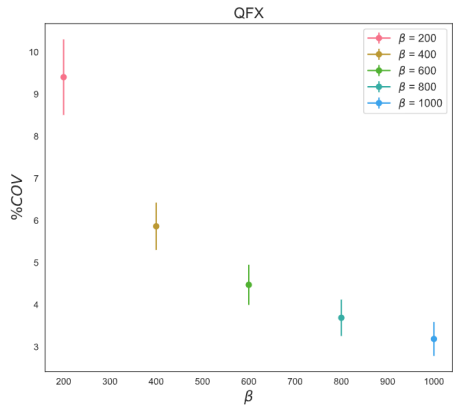

(b)

Figure 4.8: **Coefficient of Variation**: COV for the current Clinical reconstruction (HDS 2i 34s 6.4 mm FWHM) and FXS with varying number of iterative updates **(a)** as well as QFX with varying β values **(b)**

4.3.3 Combined Error

The RC and COV analysis shown illustrate the trade-off between quantitative accuracy with low bias, and high noise, and visually appealing images with low noise, and high bias (especially for small lesions). We can combine these metrics to better assess this trade off, plotting the bias as a function of the COV as in figure 4.9. OSEM reconstructions with and without TOF and PSF (as shown in table 4.1) were analyzed. All OSEM reconstructions shown were generated with the same range of IUPs, detailed in table 4.2.

Name	TOF (Y/N)	PSF (Y/N)
HD	N	N
HDS	N	Y
FX	Y	N
FXS	Y	Y

Table 4.1: **OSEM Reconstructions**: GE reconstruction algorithm names for combinations of TOF and PSF options used in this study.

Iterations	Subsets	IUP
2	8	16
3	8	24
2	16	32
3	16	48
4	16	64

Table 4.2: **IUP**: Iterative updates used for all OSEM reconstructions shown in figure 4.9

As IUP increases and β decreases, the curves in figure 4.9 move from lower left to upper right. Identifying a single point on these curves as 'best' is not immediately obvious as the answer may vary with clinical task. However, it is clear on the $Bias_{mean}$ and $Bias_{peak}$ plots that selecting curves closer to the origin (circled in green) results in reduction of both bias and noise. Based on this, moving from non TOF to TOF, from non PSF to PSF, and finally from OSEM to BSREM is advantageous. Interestingly, the benefit from PSF is greater than that of TOF. Further, the benefit of TOF is dependent on the IUP. As described by Morey and Kadrmas, at higher number of iterations and subsets the improvements in detectability conferred by TOF vanish [35].

	Clinical	HDS 2i 16s	FXS 3i 8s	QFX $\beta = 600$
Combined Error	18.3%	12.8%	11.2%	9.1%

Table 4.3: Combined Error of optimized reconstructions. Lower Combined Error values are preferred.

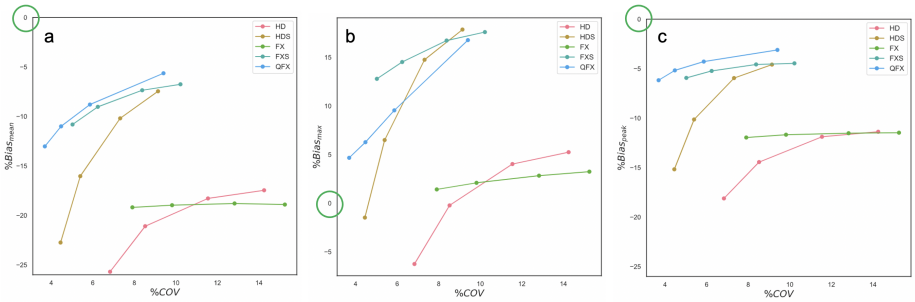

Figure 4.9: **Reconstruction Algorithm Optimization:** Bias vs noise curves were generated for each alorithm type: non TOF OSEM with and without PSF (HDS/HD), TOF OSEM with and without PSF (FXS/FX), and TOF BSREM (QFX). Shown are bias vs noise curves for mean (a), max (b), and peak (c) bias.

While the optimum reconstruction parameters within a given algorithm may be dependent on the needs of a particular clinical task, for the purposes of this study we will make a compromise by equally weighting the three types of bias as well as the COV.

$$\text{Combined Error} = \sqrt{\frac{1}{3}Bias^2_{mean} + \frac{1}{3}Bias^2_{max} + \frac{1}{3}Bias^2_{peak} + COV^2} \tag{4.11}$$

The reconstruction with the lowest Combined Error defined in this way was then chosen as the most appropriate for clinical use. HDS with $IUP = 32$ (2i 16s), FXS with $IUP = 24$ (3i 8s), and QFX with $\beta = 600$ were the OSEM (non TOF and TOF) and BSREM reconstructions with the lowest Combined Error. It is notable that each of these reconstructions exhibited significantly lower Combined Error than the Clinical reconstruction.

After selecting the OSEM reconstructions with the optimal number of iterative updates (HDS 2i 16s and FXS 3i 8s), the optimization process was repeated with post reconstruction Gaussian smoothing ranging from 2.0 to 6.4mm FWHM

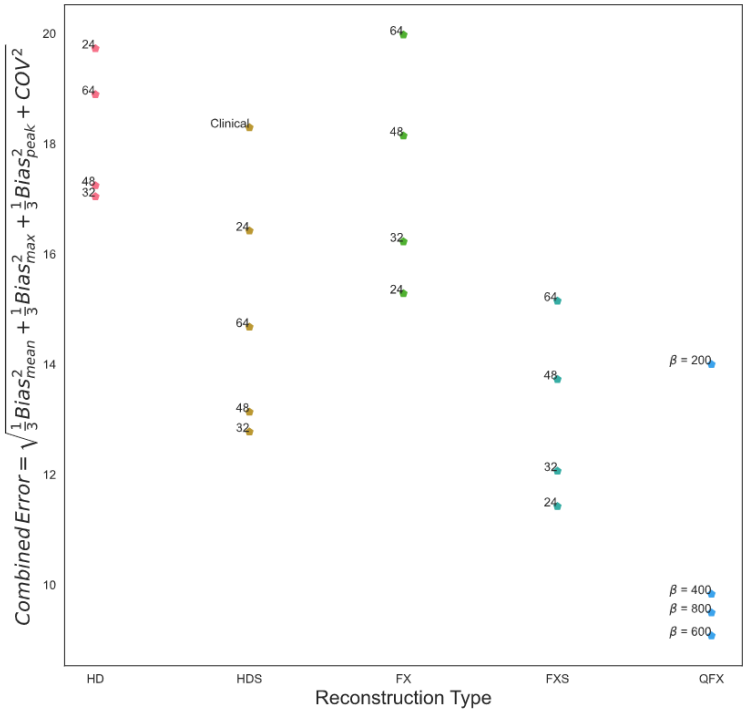

Figure 4.10: **Combined Error:** The label for each point on the OSEM reconstructions indicates the IUP used, and the BSREM reconstructions (QFX) are labeled with the choice of β parameter.

(in 0.2mm increments) using software developed in python. RCs and COV for the filtered PET images are shown in figure 4.11. Increasing the filter width lowers recovery as well as the noise level. For the non TOF HDS 2i 16s, adding Gaussian smoothing did not reduce the Combined Error, so only filtering of the TOF FXS 3i 8s is shown in figure 4.11. A filter size of **3.2mm** was found to result in the lowest Combined Error for the TOF OSEM reconstruction as shown in figure 4.12.

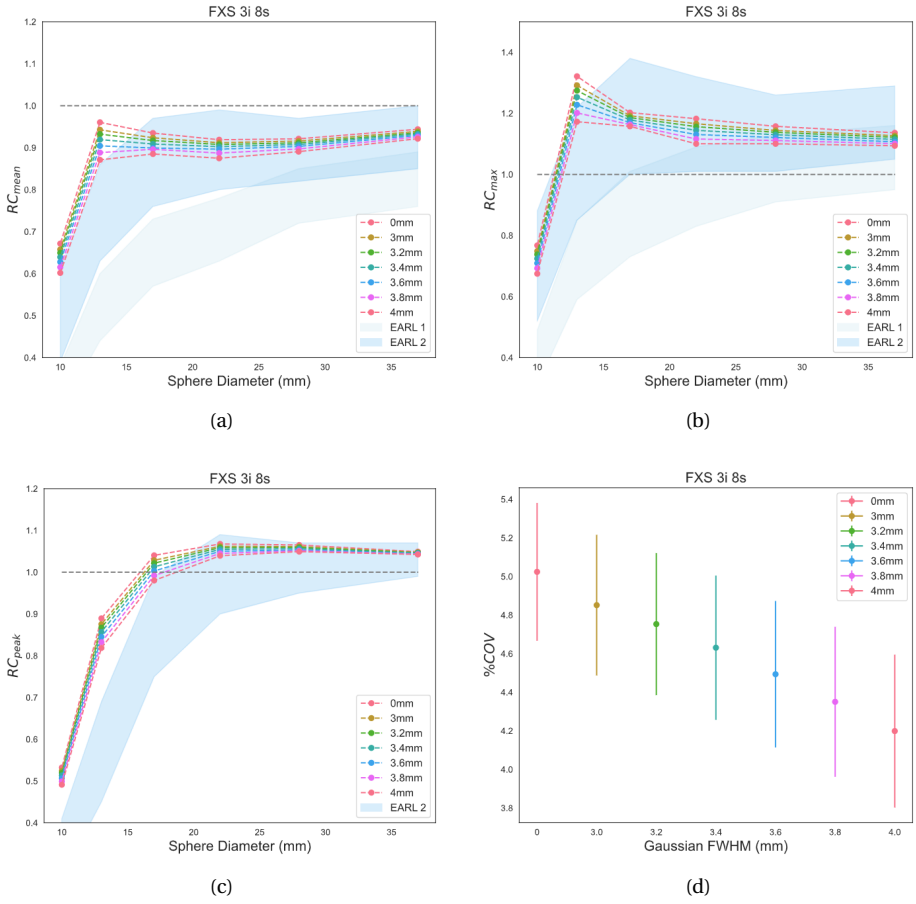

Figure 4.11: **Post Reconstruction Smoothing**: Mean, max, and peak recovery coefficients for the FXS reconstruction with chosen number of iterative updates and varying level of post reconstruction Gaussian smoothing **(a,b,c)**. Also, the effect of smoothing on the COV in the background region **(d)**.

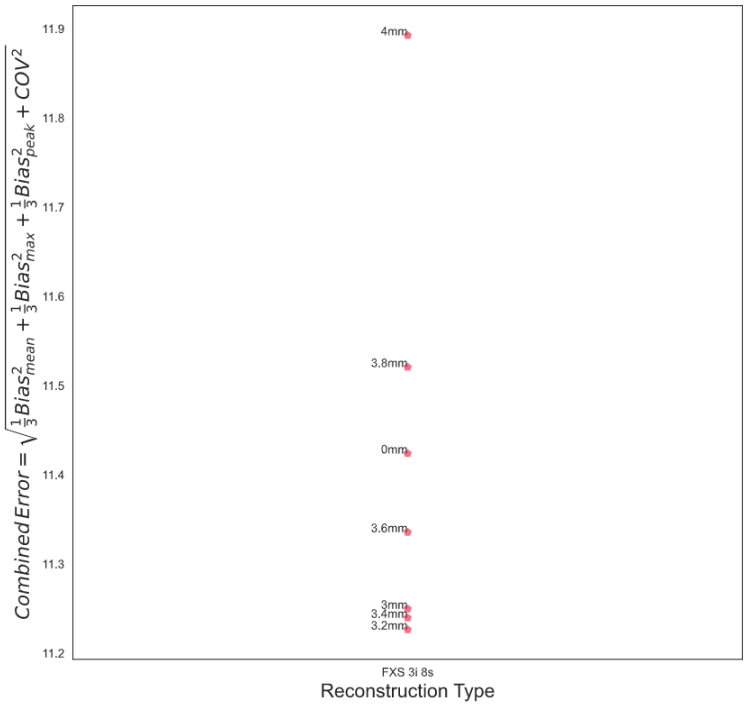

Figure 4.12: **Combined Error:** Post Reconstruction Gaussian smoothing from 0mm to 4.0mm FWHM

4.3.4 Time Activity Product

The minimum time activity product was determined for the optimized OSEM and BSREM reconstructions as well as the currently used Clinical reconstruction. Reconstructions were made using the optimized parameters with reduced counting statistics (scan durations from 600 seconds down to 19 seconds). In figure 4.13 it can be seen how COV increases with decreasing counting statistics (due to lower scan duration or TAP).

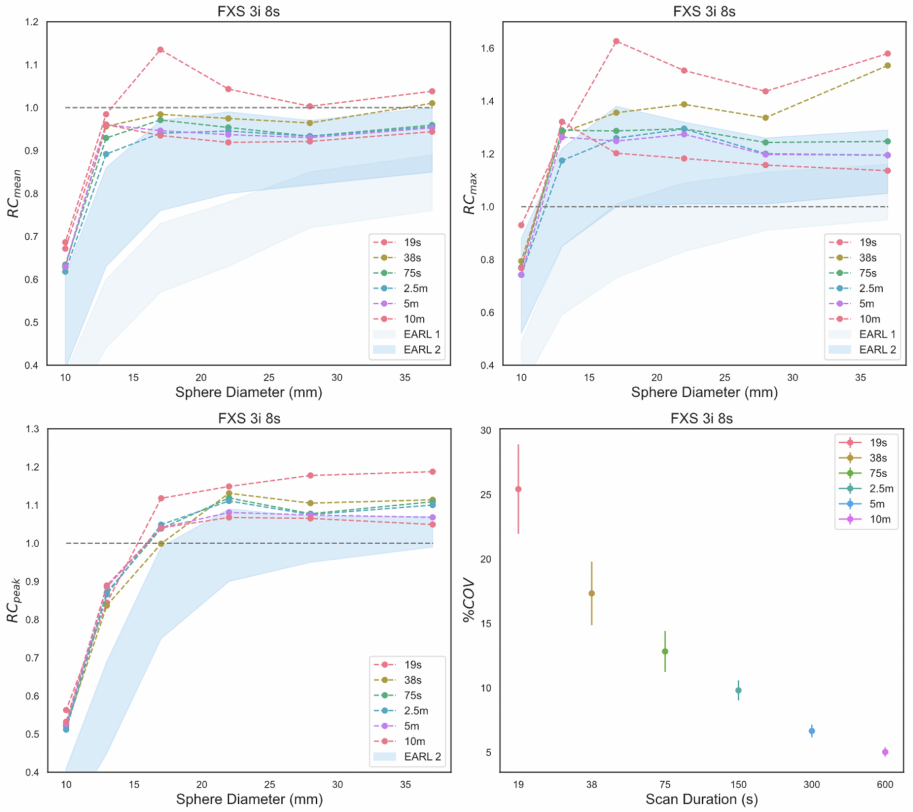

Figure 4.13: **Reduced Scan Duration**: The effect of relisting the 10 minute scan for shorter scan durations is analogous to injecting a lower activity of [^{18}F]FDG.

In addition to meeting the COV threshold chosen, reconstructions were evaluated based on their RC curves. As can be seen in figures 4.13 (a) and 4.15 the RC curves trend upwards with the reduced counting statistics of shorter scan durations.

The fit of COV and scan duration is shown in figure 4.14. The minimum scan duration is combined with the assumption that an injected activity of 83 MBq in a 75 kg patient would result in a hepatic activity concentration of 2.0 kBq/mL (as in the background of the NEMA IQ phantom) to obtain values of TAP shown in table 4.4.

	HDS 2i 34s 6.4mm	FXS 3i 8s 3.2mm	QFX 600
COV Threshold		10%	
A inj		83 MBq	
T_{min}	171 s	115 s	135 s
$TAP_{75\,kg}$	237 min × MBq	159 min × MBq	187 min × MBq
% Difference	-	-32.7%	-21.1%

Table 4.4: **Time Activity Product:** Minimum product of injected activity and scan duration for Clinical HDS, optimized FXS and QFX reconstructions.

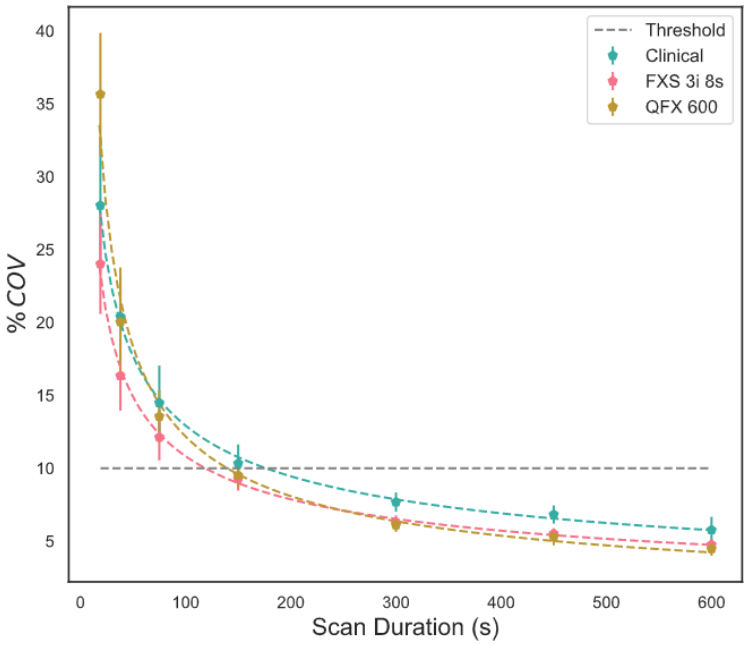

Figure 4.14: **Minimum Scan Duration:** T_{min} is determined using the power law fit of COV and scan duration and a noise threshold of 10%

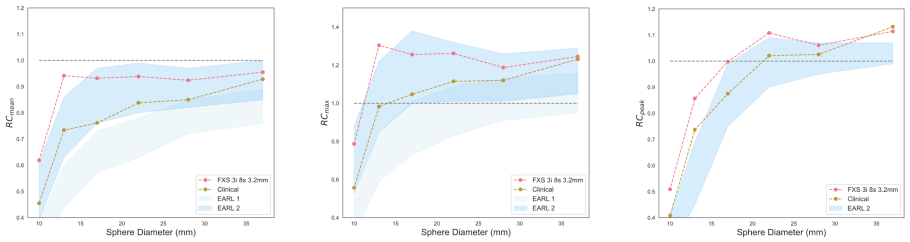

(a) (b) (c)

Figure 4.15: **Low Counting Statistics:** RCs are shown for reconstructions of 1 minute acquisitions re-binned from list mode data using the Clinical and optimized FXS reconstructions.

The recovery of the optimized and Clinical reconstructions were analyzed using 1 minute list mode data (below the calculated T_{min}) to demonstrate the stability of the RCs at low counting statistics. Recovery is biased upwards at reduced counting statistics.

4.4 Discussion

This study was part of an effort to characterize the image quality of current whole-body [^{18}F]FDG PET protocols in place in BC Cancer and to recommend updates to this protocol. In the near future, three state-of-the-art, identical PET/CT scanners will be serving patients throughout BC Cancer (Victoria, Vancouver, and Kelowna). These new scanners necessitate review and update of the current clinical protocols, in terms of the reconstruction methods used as well as the injected activity and scan duration for each patient. NEMA IQ phantom experiments were performed on one of the newly installed GE Discovery MI digital PET/CT scanners.

Other investigations into the image quality capabilities of the Discovery MI PET/CT scanner have included studies of the NEMA IQ phantom, but these have focused on clinically used reconstructions and have evaluated noise (COV) and bias (RC) separately [59][53][60]. To the best of our knowledge, this is the first work to optimize the available reconstruction methods by minimizing the combined error due to both bias and noise. Though the optimal parameters may depend on the clinical task, whether it be visual analysis by a physician, or feature selection using artificial intelligence, the method proposed in this chapter represents a compromise between quantitative and visually optimized images. Future insights from

nuclear medicine physicians may lead to updating the criteria for parameter optimization. In defining the Combined Error metric used to optimize parameters, it was decided to give equal weight to the three types of bias and COV. This decision is a starting point and could be adapted to better serve the needs of physicians. For example, because the physicians in BC Cancer only report SUV_{max} values, it may be more appropriate to give increased weight to $Bias_{max}$ and reduce the weight given to $Bias_{mean}$ which is seldom used outside of phantom experiments.

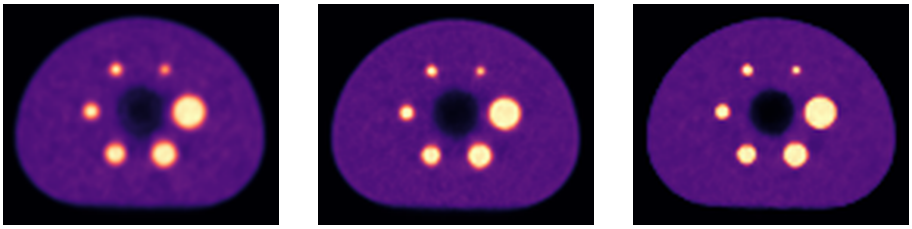

(a) (b) (c)

Figure 4.16: **Optimized Reconstructions:** The same axial slice of the NEMA IQ is shown reconstructed with the Clinical reconstruction (HDS 2i 34s 6.4mm FWHM) (**a**) as well as the optimized reconstructions: FXS with 3i 8s 3.2mm FWHM (**b**) and QFX with $\beta = 600$ (**c**)

The recovery coefficients of the unfiltered, PSF corrected reconstructions (FXS and QFX shown in figure 4.7) exhibit the Gibbs artifact-like edge overshoot effect [61]. This resulted in over estimated recovery of the 13 and 17mm spheres. This effect was mitigated by increasing β value for QFX reconstructions and by using more aggressive filtering of the FXS reconstructions (as can be seen in figure 4.11). Higher β values and filtering also had the effect of reducing COV measured in the background compartment of the phantom and lowering the Combined Error.

Reconstructions of the 10 minute list mode data for the the Clinical reconstruction as well as optimized FXS and QFX reconstructions are shown in figure 4.16. The partial volume effect can be seen visually in the Clinical reconstruction **(a)**, where the smallest sphere has lower recovery and all of the spheres exhibit blurred edges. Both the FXS and QFX reconstructions **(b,c)** maintain low levels of noise, as seen in the smooth uniform background, while having sharper edges of the hot spheres.

The low value of the TAP_{75kg} obtained in this study illustrates the high performance of the current state-of-the-art PET scanners. The increased detector sensitivity paired with the optimized reconstruction parameters as well as TOF and PSF

correction mean that the image quality of patient scans can be increased while reducing injected activity. Under the current clinical protocol, 75 kg patients are injected with ~ 250 MBq [^{18}F]FDG and scanned for 2.5 minutes. The updated phantom preparation assumption suggests very low injected activities. If the 2.5 minute time per bed position was kept the same, this assumption implies that the same patient could be injected with 63 MBq, nearly a quarter of the previous dose. It may not be reasonable to directly compare phantom preparations with injected activities in patients based on hepatic activity alone. To avoid dependency on this assumption, activity could instead be scaled by the ratio of T_{min} shown in table 4.4. This would lead to a reduction in TAP of 32.7% for 75 kg patients. Because this result is based on fixing the COV at a threshold of 10%, the image noise should be comparable to that of scans acquired with the current Clinical reconstruction but with significantly reduced bias.

4.4.1 Limits

One of the key assumptions of this study is that scan duration and injected activity have an equivalent impact on the image quality of a reconstructed PET image. While this is true to a first order approximation, there are limits to the image quality benefits of increasing injected activity, dependent on the noise equivalent count rate (NECR) and the reconstruction algorithms/parameters used [58]. SNR^2 exhibits a nonlinear relationship beyond the NECR peak for OSEM reconstructions, and further, if present, detector dead time would result in the collected data not following a Poisson distribution [62]. Given the relatively low activity concentrations measured and recommended in this study, it is reasonable to assume that the injected activity is within the linear region of the NECR curve. However, when scaling the recommended TAP to larger patients, care should be taken not to increase the injected activity too much, instead relying on longer scan durations per bed to achieve the target TAP.

In the literature, EARL, who first proposed the NEMA IQ experiment as a method to determine the minimum injected activity of [^{18}F]FDG, reference the assumption that a 75 kg patient injected with 300 MBq will have a whole body activity concentration of 2.0 kBq/mL when scanned 60 minutes post injection [51][52]. Others have proposed alternative relationships between phantom preparation and activity concentration in patients [60]. Based on the measured hepatic activity concentration of patients scanned at BC Cancer, the hepatic activity concentration is significantly higher than the average whole body activity concentration. The as-

sumption presented here, that the phantom preparation is analogous to a 75 kg patient injected with 83 MBq was justified using the measured average hepatic activity concentration normalized by injected activity per mass. The magnitude of the discrepancy between this assumption and the one presented by EARL suggests that caution should be taken when directly comparing phantom and patient injected activities.

Finally, the injected activity and scan duration recommended here is, of course, only valid for a 75 kg patient. In order to apply this recommendation to patients of all sizes, a proper scaling method must be validated. Others have suggested linear, quadratic, or even no scaling of injected activity at all [50][22]. In order to validate any of these approaches or another entirely, the relationship between patient size and image quality must be examined. Chapter 5 will focus on our own analysis to better scale and optimize the injected activity in our centre.

4.5 Conclusions

The performance of a GE Discovery MI PET/CT scanner was evaluated using list mode scans of a NEMA IQ phantom filled with known activity concentrations of [^{18}F]FDG. The list mode data were reconstructed using several different algorithm types including the proprietary GE BSREM-based algorithm, Q.Clear. The scans were evaluated using metrics for noise and bias, allowing for the optimization of reconstruction methods. Three reconstructions are suggested as significant improvements over the reconstruction currently used by PET centres in BC Cancer: HDS with 2 iterations, 16 subsets, FXS with 3 iterations, 8 subsets, and 3.2mm FWHM Gaussian smoothing, and QFX with $\beta = 600$. Using the optimized TOF OSEM reconstruction (FXS), a minimum time activity product for a 75 kg patient (TAP_{75kg}) was determined using a COV threshold of 10%. These recommendations could provide a ~33% reduction in patient dose while simultaneously improving the quantitative value of PET images. The results presented here must be combined with a validated dose scaling protocol in order to ensure target image quality is achieved for every patient scanned at BC Cancer.

Chapter 5

Optimization of Injected [^{18}F]FDG based on Patient Image Quality Study

5.1 Introduction

One of the goals of quantitative molecular imaging is to provide high quality diagnostic images for all patients, regardless of their anatomy. [^{18}F]Fluorodeoxyglucose PET scans of larger patients suffer from reduced counting statistics due to increased attenuation and scatter, resulting in lower image quality that can ultimately jeopardize the detection of small lesions and raise the rate of false negatives [19]. The most straightforward solution to this problem is to increase the activity of injected [^{18}F]FDG or the scan duration when scanning larger patients [20]. The European Association of Nuclear Medicine (EANM) has published [^{18}F]FDG imaging guidelines for tumours and provides minimum injected activity formulas including linear or quadratic scaling with patient body mass. The linear regimen is suggested as an option on the basis of 'pragmatic reasons', while quadratic scaling is presented as a method of '[compensating] for the lower signal to noise ratio (and hence degraded image quality)' [63] that results when linear scaling is applied to heavier patients.

In order to identify the target image quality, some studies have considered the activity necessary to reach peak noise equivalent count rate (NECR) or a thresh-

old of noise equivalent counts (NEC) [58][23][64]. However, accurate estimation of patient-specific NECR is difficult to obtain (count rate information is not always available from reconstructed images) and varies significantly over the length of each patient due to varying levels of scatter and attenuation [58]. The signal-to-noise ratio measured in the liver (SNR_L) is a more common metric that has been used to quantify patient image quality [65]. The relative uniformity of hepatic uptake makes SNR_L a robust metric that is not highly impacted by differences in biological uptake between patients [66]. By examining the relationship between SNR_L and a variety of patient dependent parameters, de Groot *et al.* suggest that quadratic scaling of injected activity with patient body mass resulted in consistent image quality across a range of patient sizes [22].

The optimal relation between injected activity and patient size is also dependent on the scanner used. Detector characteristics and reconstruction algorithms provided by different vendors require validation of activity scaling protocols on each scanner.

The first aim of this study was to characterize the relationship between patient dependent parameters and image quality in existing [^{18}F]FDG PET scans previously acquired at BC Cancer. The work presented in this chapter is based on the method proposed by de Groot *et al.* and expands upon it by combining the recommendations for implementing new reconstruction methods presented in the previous chapter. The result is a protocol that is not just focused on the amount of injected activity but also includes the scan duration, allowing for optimal use of of resources for radioisotope production and patient throughput. This protocol is expected to provide a similar image quality for all patients scanned at BC Cancer regardless of their anatomy and physiology.

5.2 Methods

This study used PET/CT images from a cohort of 200 patients scanned at BC Cancer Victoria and Vancouver centres (100 patients from each centre). the study was conducted retrospectively and has received ethics approval from the BC Cancer Research Ethics Board (H20-00347) and the University of Victoria (20-0405).

5.2.1 Patient Inclusion Criteria

Patients included in this study were scanned with [^{18}F]FDG PET/CT at BC Cancer between August 1, 2019 and June 1, 2020. All patients were over the age of 18 and

did not have lesions or disease in the liver that would disrupt the uniformity of hepatic [^{18}F]FDG uptake. Also, patients included in this study represented a range of patient body masses (from 45 to 168 kg) as shown in figure 5.1 so that the relationship between image quality and patient size could be characterized over a range reflective of the population.

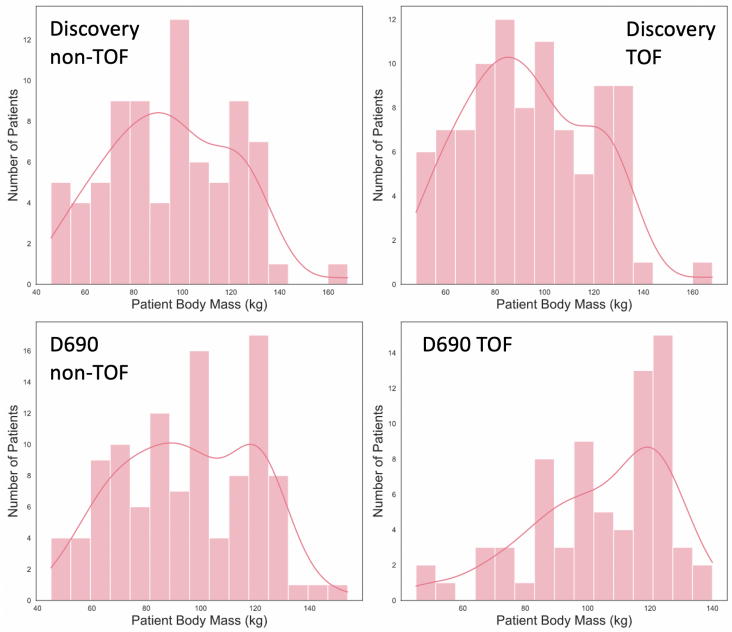

(a)

Figure 5.1: **Distribution of Patient Body Mass**: Patient body mass was extracted from the DICOM headers of scans used in this study acquired on the Discovery MI and D690 scanner reconstructed with non-TOF and TOF.

5.2.2 Scanners and Image Reconstructions

The PET/CT images analyzed in this study were obtained on two GE scanners: a state-of-the-art Discovery MI and a previous generation scanner, a D690 PET/CT (GE Healthcare, Waukesha, WI). Images were reconstructed using two algorithms: non-TOF OSEM with PSF correction (HDS), which is the current protocol from which SUV values are being reported in the clinic, and OSEM with PSF and TOF correction. Table 5.1 summarizes the reconstruction parameters used in the current clinical protocol. Note that not all patient scans were available with both reconstructions. The raw data, that would allow for retrospective reconstructions

was not available and no additional parameters could be tested on this cohort of patients.

	Discovery MI	D690
Algorithm	# of Scans	# of Scans
OSEM + PSF (HDS)	78	109
OSEM + TOF + PSF (FXS)	93	72
Iterations	2	2
Subsets	34	34
Gaussian Filter FWHM (mm)	6.4	6.4

Table 5.1: **Scan Parameters**: The scanner and reconstructions used to acquire all patient images. Vue Point HDS and FXS are GE's OSEM reconstruction algorithms incorporrating PSF correction (referred to as SharpIR by the manufacturer).

5.2.3 Signal-to-Noise Ratio Calculation

Image quality of patient scans was quantified by determining the SNR_L of each PET/CT image according to:

$$SNR_L = \frac{Mean_{VOI}}{SD_{Union}} \tag{5.1}$$

The numerator, $Mean_{VOI}$, was calculated by taking the average pixel value of volumes of interest (VOIs) placed in the right lobe of the liver, near the dome. The denominator, SD_{Union}, was calculated by measuring the standard deviation (SD) of the union of the VOIs. Noise was calculated from the union of the VOIs so that a sufficient number of pixels was used. Four 3cm diameter spherical volumes of interest (VOI) were placed using MIM® (MIM Software Inc., Cleveland, OH). An example of VOI placement in the liver is shown in figure 5.2.

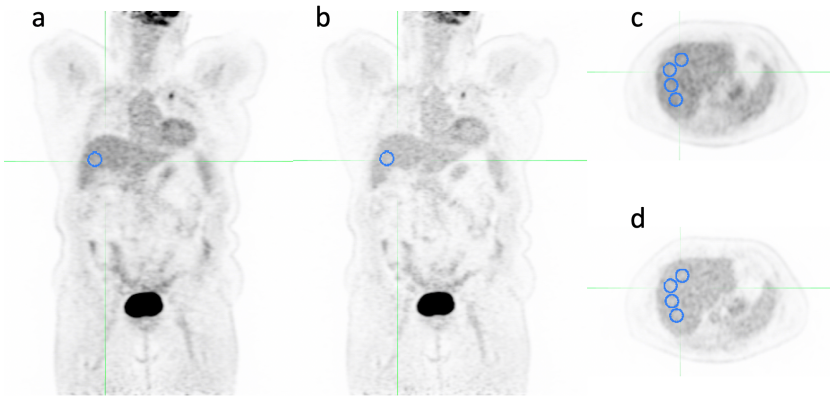

(a)

Figure 5.2: **Patient FDG PET Images**: axial and coronal slices of a patient PET image reconstructed with non-TOF **(a,c)** and TOF **(b,d)** scanned with the Discovery MI. The placement of spherical VOIs is also shown.

The mean pixel value, and standard deviation of each VOI (as well as their union) were exported as CSVs for analysis with Python. The mean and SD of SNR_L calculated using the each of the four VOIs were then reported as SNR_L and the relative error.

5.2.4 Extraction of Patient Metadata

To determine the injected activity for each patient, and to find correlations with image quality and patient anatomy, the following fields were extracted from the DICOM headers of each scan:

- Patient body mass (kg)
- Patient Height (m)
- Patient Sex
- Scan Date-time
- Actual frame duration (time per bed position)
- Injected Activity (Bq)
- Injection Date-time
- Scan Date

In addition to the parameters available directly from the DICOM headers, patient anatomical characteristics were calculated including:

- Mass per length (kg/m)
- Body surface area
- Body mass index
- Lean body mass
- Fat mass

Body surface area (BSA) was calculated using the Mosteller equation [67] according to:

$$BSA(m^2) = \sqrt{\frac{height(cm) \times weight(kg)}{3600}} \tag{5.2}$$

Lean body mass (LBM) was calculated using three formulas as defined by Boer, James [68], and Hume [69] according to:

$$LBM_{male}^{Boer} = (0.407 \cdot m) + (0.267 \cdot H) - 19.2 \tag{5.3}$$

$$LBM_{female}^{Boer} = (0.252 \cdot m) + (0.473 \cdot H) - 48.3 \tag{5.4}$$

$$LBM_{male}^{James} = (1.10 \cdot m) - 128 \cdot \left[\frac{m^2}{100 \cdot H}\right] \tag{5.5}$$

$$LBM_{female}^{James} = (1.07 \cdot m) - 148 \cdot \left[\frac{m^2}{100 \cdot H}\right] \tag{5.6}$$

$$LBM_{male}^{Hume} = (0.32810 \cdot m) + (0.33929 \cdot H) - 29.5336 \tag{5.7}$$

$$LBM_{female}^{Hume} = (0.29569 \cdot m) + (0.41813 \cdot H) - 43.2933 \tag{5.8}$$

Fat mass was calculated by subtracting LBM (using each of the above definitions) from total body mass.

5.2.5 Analysis

As discussed in previous chapters, positron emission is a random process following a Poisson distribution, therefore the signal to noise ratio of the collected lines of response should be described by [58]:

$$SNR_{data} = \frac{Mean}{SD} \sim \frac{N}{\sqrt{N}} = \sqrt{N} = \sqrt{A \cdot t} \tag{5.9}$$

where N is the number of positron annihilations, A is the injected activity decay-corrected to the time of scan, and t is the duration of the scan. In practice, image degrading effects such as scatter, randoms, attenuation, detector response, and propagation of noise through reconstruction methods should also be included in the above formula. For the SNR_L measured in this study it would be more accurate to describe the relation with injected activity and scan duration as proportional:

$$SNR_L \propto \sqrt{A \cdot t} \tag{5.10}$$

A constant of proportionality, K, is then introduced such that:

$$SNR_L = K \cdot \sqrt{A \cdot t}. \tag{5.11}$$

Solving for K, we obtain:

$$K = \frac{SNR_L}{\sqrt{A \cdot t}} \tag{5.12}$$

K may have complex dependencies on the properties of the scanner and many patient dependent parameters that are outside the scope of this work [65]. However, clinical insight can be gained by modeling K as a power law function of a single patient dependent anatomical characteristic, p:

$$K = a \cdot p^{-b} \tag{5.13}$$

where a and b are fit parameters. Combining equations 5.12 and 5.13 we obtain an expression relating SNR_L, the time-activity product, and a patient dependent anatomical characteristic:

$$SNR_{norm} = \frac{SNR_L}{\sqrt{A \cdot t}} = a \cdot p^{-b} \tag{5.14}$$

After characterizing this relationship, the method proposed by de Groot *et al.*

proceeded by determining a clinically acceptable level of image quality, SNR_{acc}, based on the qualitative judgment of nuclear medicine physicians [22]. By substituting SNR_{acc} for SNR_L in equation 5.14 and rearranging we see that:

$$SNR_{acc} = \sqrt{A \cdot t} \cdot a \cdot p^{-b} \tag{5.15}$$

Finally, by solving for the time-activity product (TAP), $A\dot{t}$, an injected activity protocol is derived:

$$A \cdot t = \left(\frac{SNR_{acc}}{a} \right)^2 \cdot p^{2b} \tag{5.16}$$

Because SNR_{acc} is held constant, it is expected that an injected activity protocol of the form of equation 5.16 will result in consistent image quality across a range of the modeled patient anatomical characteristic, p. Rather than independently determine SNR_{acc} as de Groot *et al.* did, a value of 10 was chosen. The time activity product was also scaled by the ratio of the TAPs derived from the clinical and optimized reconstructions presented in chapter 4. This allows for the TAP to be reduced when the optimized reconstruction methods are implemented clinically.

The analysis was performed using the following patient dependent anatomical characteristics: body mass, mass per length, body surface area, body mass index, lean body mass, and fat mass. The anatomical characteristics with the highest correlation between TAP and SNR_L (highest coefficient of determination) was chosen as the basis for a new injected activity protocol, following equation 5.16. The relative error of the fit was computed for each PET/CT image according to:

$$SNR_{fit} - \frac{SNR_{norm}}{SNR_{fit}} \times 100\% \tag{5.17}$$

where SNR_{fit} is $a \cdot p^{-b}$ evaluated at the same values of p as SNR_{norm}. A Bartlett's test was then performed between the the distribution of relative error for the anatomical characteristic, p, with the highest R^2 and each other anatomical characteristic to test the null hypothesis that the samples were taken from the same distribution. Low values of the test statistic indicate that the sample size is sufficient to distinguish the quality of fits. Statistical significance was set to a threshold of $p = 0.05$.

The coefficient of variation (COV) was also measured using the same four VOIs in the liver used for the SNR_L analysis. The mean and SD of the means of the four VOIs was computed and used to calculate COV according to:

$$COV = \frac{SD_{means}}{Mean_{means}} \tag{5.18}$$

For this analysis, only the mean pixel value of each of the four VOIs was used (the SD of the pixels contained in each VOI or the union of VOIs was not used). This definition of COV is analogous to treating each VOI as a unique noise realization.

In addition to image quality analysis, the measured hepatic activity concentration of each patient was also used to assess the phantom preparation assumptions discussed in the previous chapter. The mean activity concentrations in the liver (kBq/mL) as a function of the injected activity (MBq) and body mass normalized injected activity (MBq/kg) were investigated. A possible way of scaling phantom injected activity to reflect realistic hepatic activity concentrations is discussed.

5.3 Results

Figures 5.3 and 5.4 show the injected activity, injected activity at the time of the scan, the bed duration, and the time-activity product for the examined group of patients scanned with the Discovery MI and D690, respectively.

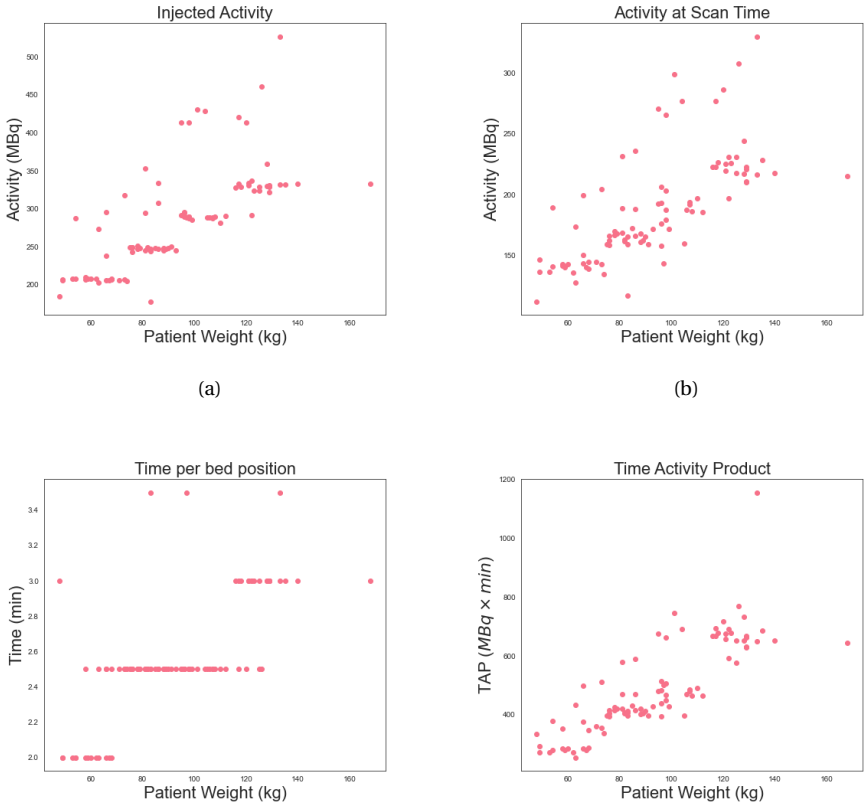

Figure 5.3: **Injection information for the patients scanned on the Discovery MI**: The activity of [^{18}F]FDG at time of injection **(a)**, and decay-corrected to time of scan **(b)** as a function of patient body mass for scans acquired in Victoria with the Discovery MI. Also shown are the bed durations **(c)**, and time-activity product **(d)**.

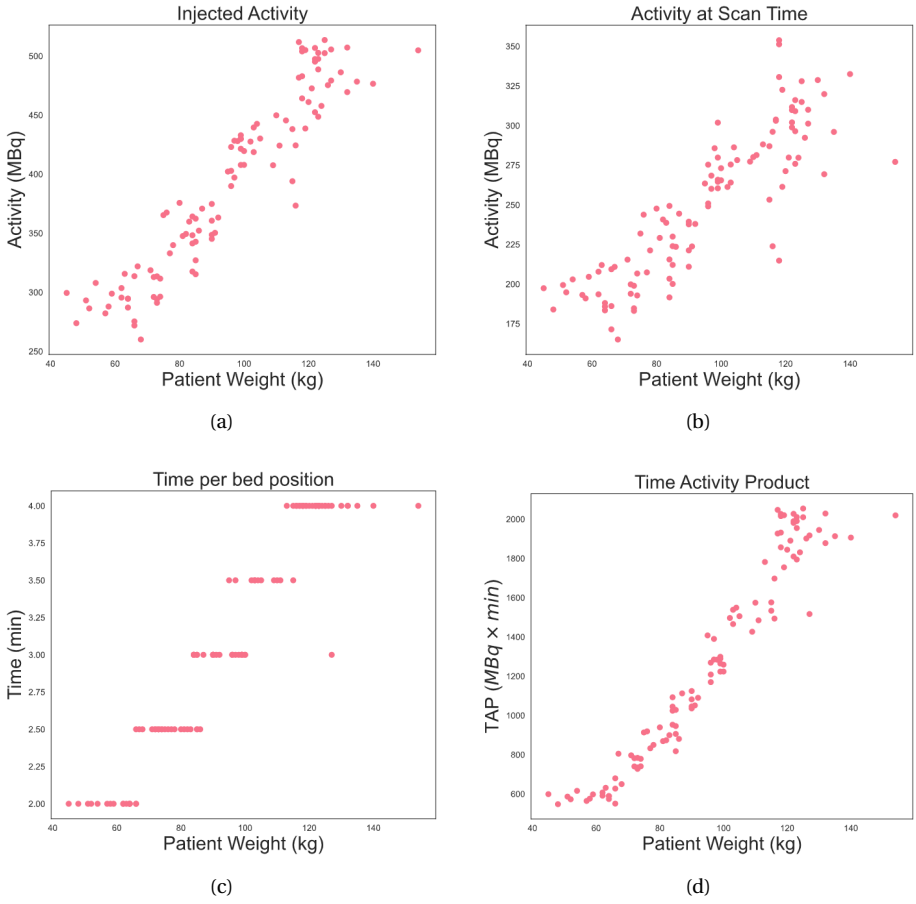

Figure 5.4: **Injection information for the patients scanned on the D690**: The activity of [^{18}F]FDG at time of injection **(a)**, and decay-corrected to time of scan **(b)** as a function of patient body mass for scans acquired in Vancouver with the D690. Also shown are the bed durations **(c)**, and time-activity product **(d)**.

The measured SNR_L and COV as a function of patient body mass are shown in figures 5.5 and 5.6. If the current injected activity protocol was sufficient to overcome the deficits in counting statistics suffered by larger patients, the slope of the linear regression should be zero. However, it can be seen that under the current injection and scanning protocols, both metrics of image quality degrade with increasing patient body mass (SNR_L decreases and COV increases).

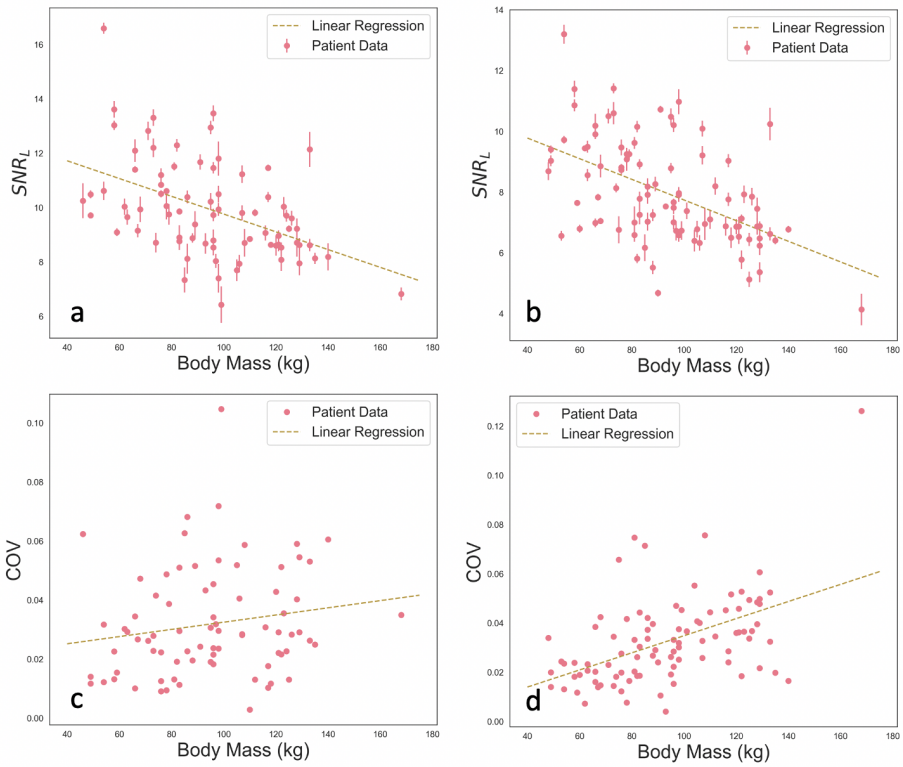

Figure 5.5: **Image Quality for PET/CT images acquired with the Discovery MI scanner**: The measured SNR_L and COV as a function of patient body mass for non-TOF reconstructions **(a,c)** and TOF **(b,d)**.

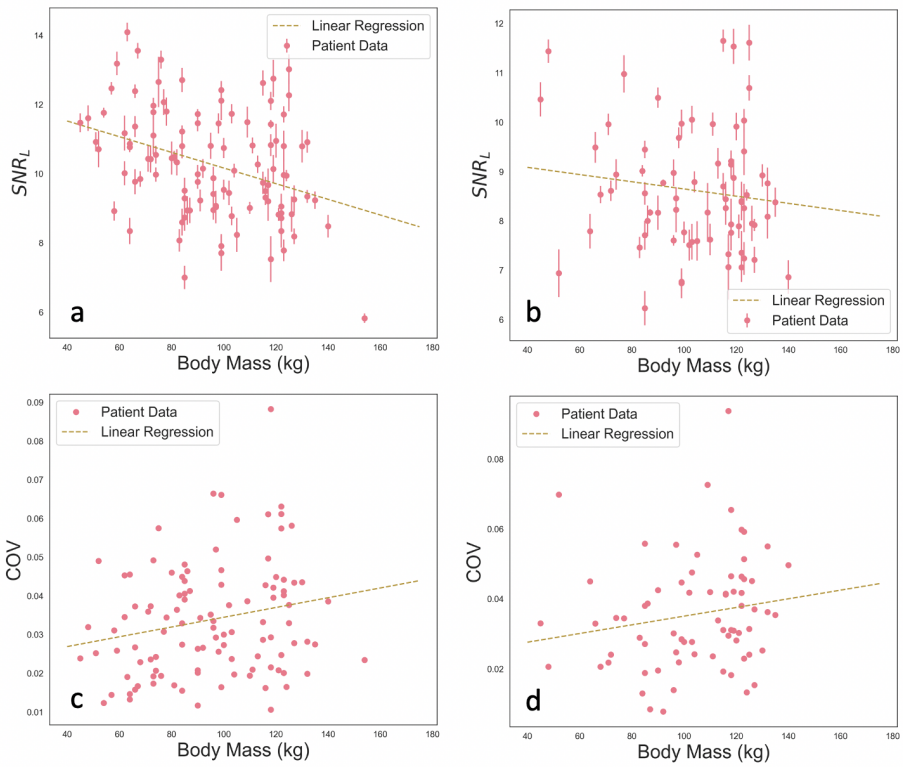

Figure 5.6: **Image Quality for PET/CT images acquired with the D690 scanner**: The measured SNR_L and COV as a function of patient body mass for non-TOF reconstructions **(a,c)** and TOF **(b,d)**.

SNR_{norm} as a function of patient dependent anatomical characteristics are shown in figures 5.7 - 5.10. Also shown are the power law fits calculated according to equation 5.14 and the fit parameter, b.

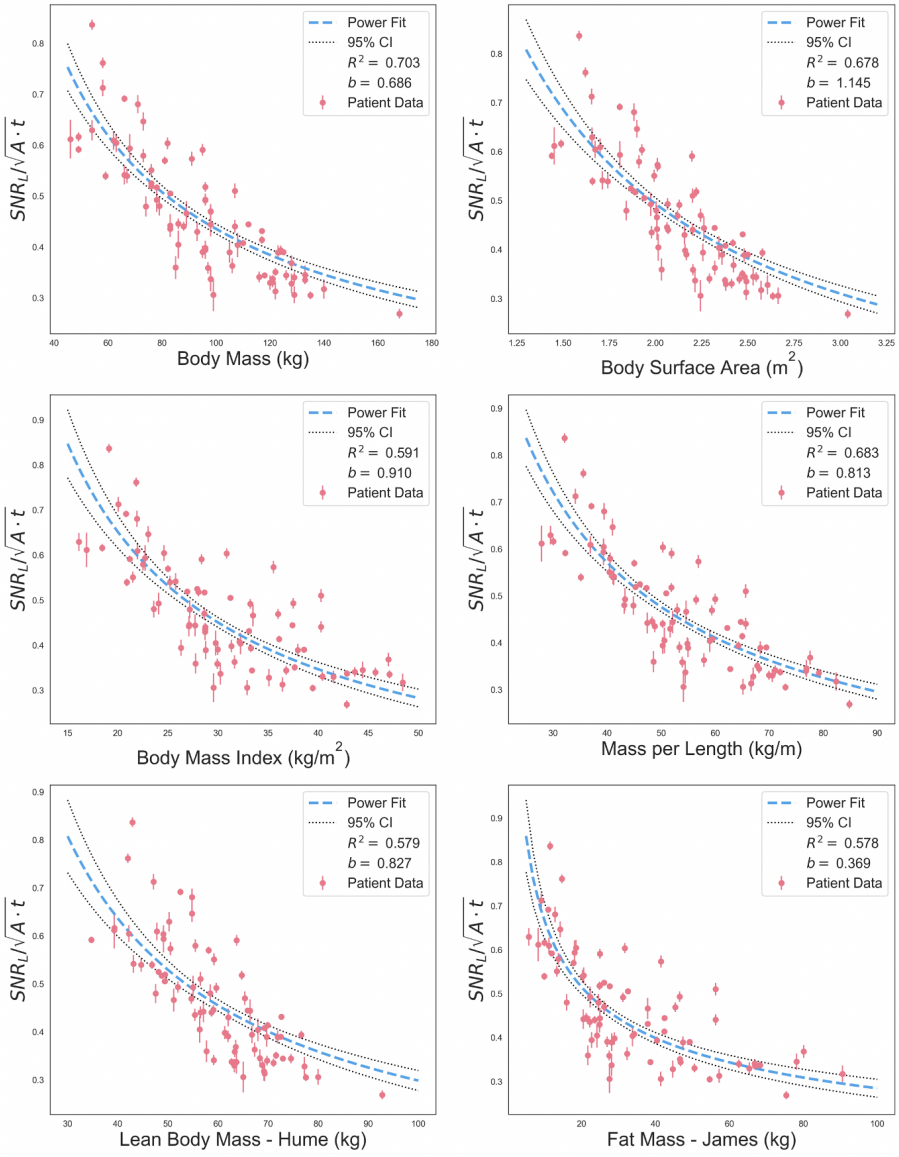

Figure 5.7: **Discovery MI (non-TOF) Normalized SNR**: SNR_L normalized by the injected activity and scan duration as a function of patient dependent anatomical characteristics for patients scanned on the Discovery MI reconstructed with non-TOF. Only the lean body mass and fat mass definitions with the highest R^2 are shown.

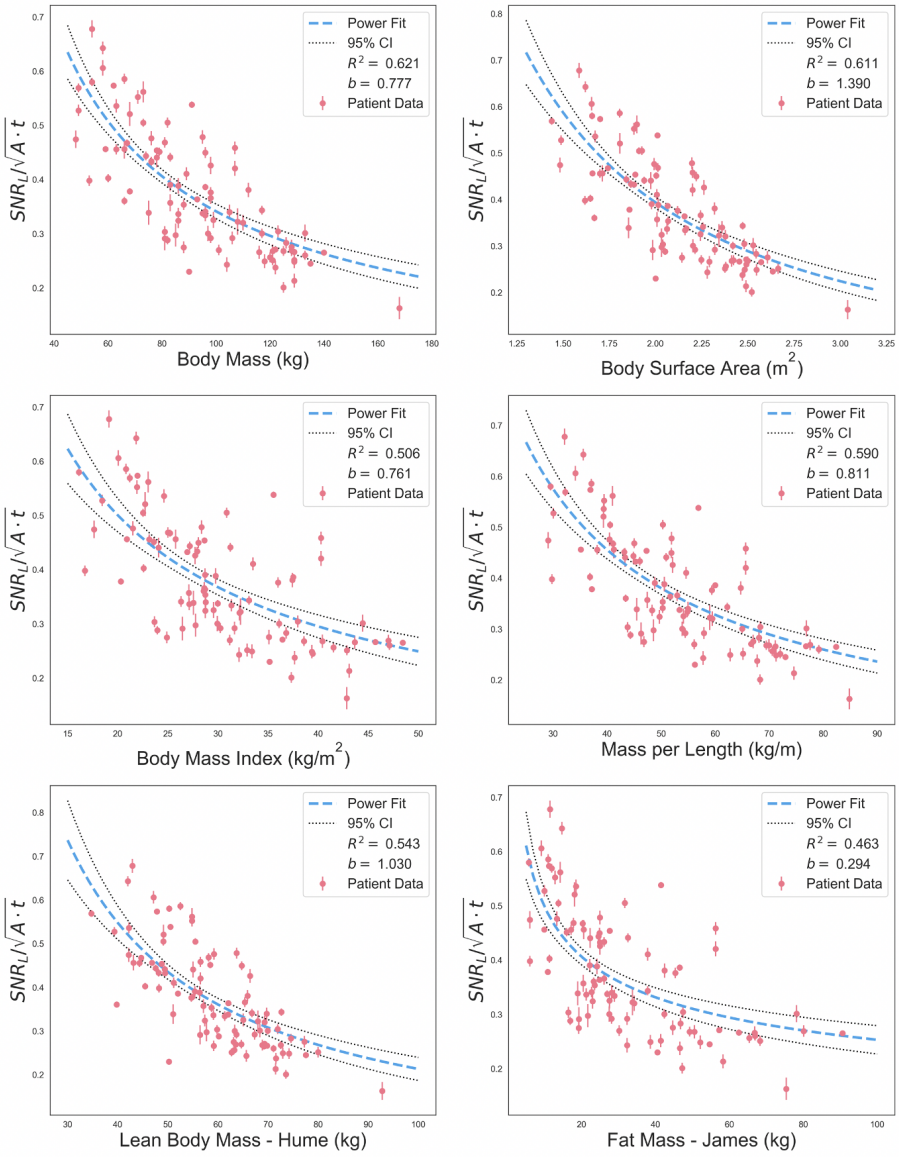

Figure 5.8: **Discovery MI (TOF) Normalized SNR**: SNR_L normalized by the injected activity and scan duration as a function of patient dependent anatomical characteristics for patients scanned on the Discovery MI reconstructed with TOF. Only the lean body mass and fat mass definitions with the highest R^2 are shown.

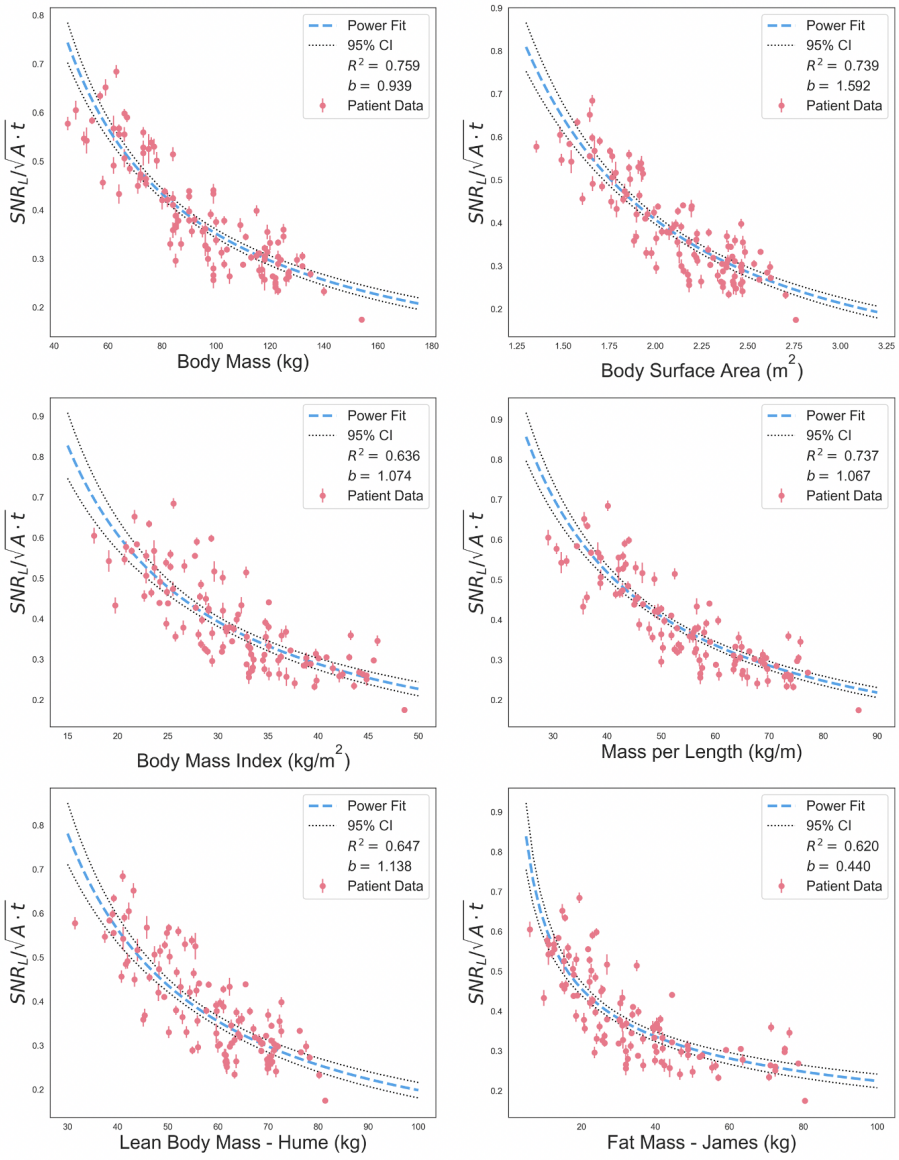

Figure 5.9: **D690 (non-TOF) Normalized SNR**: SNR_L normalized by the injected activity and scan duration as a function of patient dependent anatomical characteristics for patients scanned on the D690 reconstructed with non-TOF. Only the lean body mass and fat mass definitions with the highest R^2 are shown.

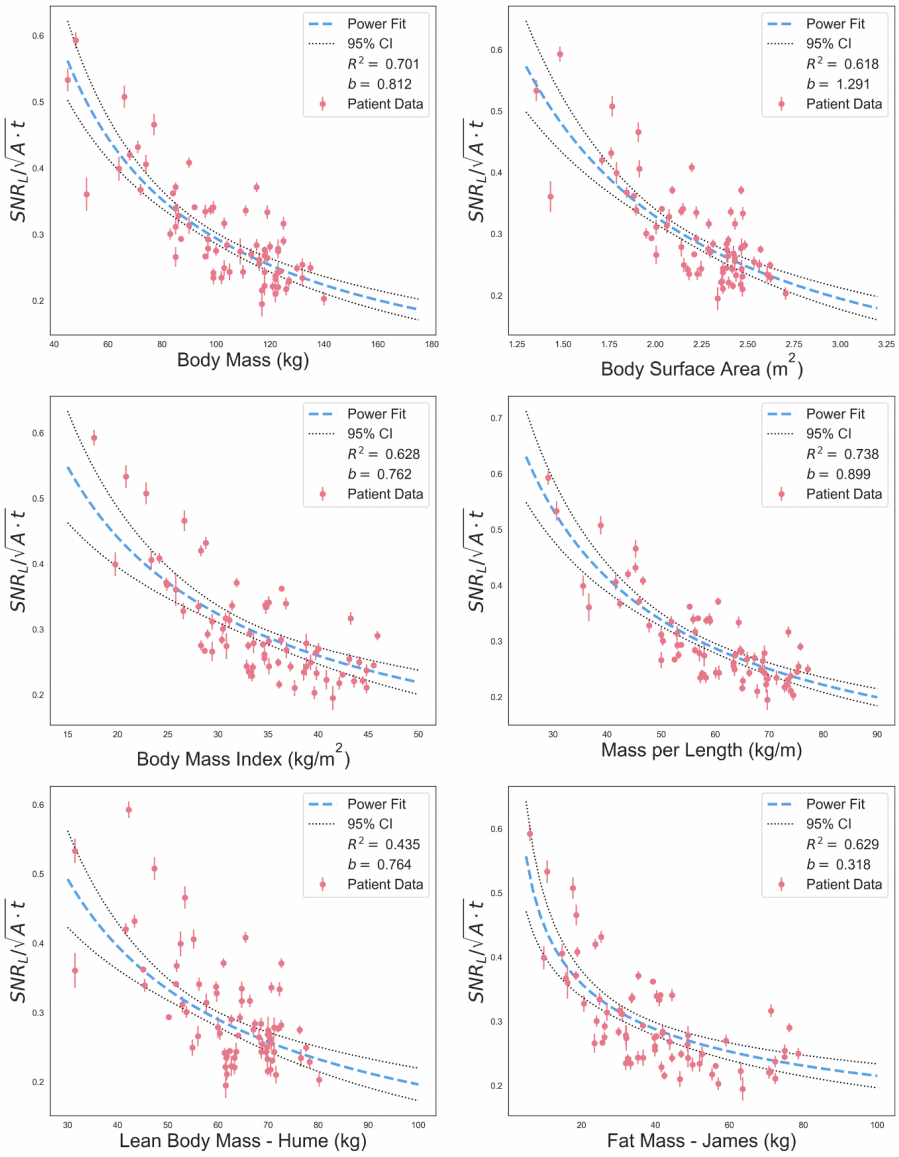

Figure 5.10: **D690 (TOF) Normalized SNR**: SNR_L normalized by the injected activity and scan duration as a function of patient dependent anatomical characteristics for patients scanned on the D690 reconstructed with TOF. Only the lean body mass and fat mass definitions with the highest R^2 are shown.

The calculated fit parameters from equation 5.14, coefficient of determination (R^2), and p-value from the Bartlett's test for each patient dependent anatomical

characteristic are displayed in table 5.3. Patient body mass was the parameter with the highest correlation between TAP and SNR_L for both scanners and reconstruction types. The power law fit of the non-TOF reconstructed images exhibited a higher R^2 than the TOF reconstructed images. Therefore the power law fit parameters from the non-TOF fit were used as the basis of a new activity and scan duration protocol. For the Discovery MI, using equation 5.16 we obtain:

$$A \cdot t = \left(\frac{10}{10.268}\right)^2 \cdot m^{1.372} = 0.9485\, m^{1.372} \xrightarrow[\text{Decay}]{\text{-1 hr}} 1.385\, m^{1.372}\, MBq \times min \tag{5.19}$$

where m is the patient body mass. The product was decay corrected back 1 hour to the time of injection. Then, scaling by the ratio of TAPs for the clinical non-TOF reconstruction (HDS 2i 34s) and the optimized FXS and QFX reconstructions investigated in chapter 3, we obtain:

$$\text{FXS 3i 8s:} \qquad A \cdot t = 0.932 \cdot m^{1.372}\, MBq \times min \tag{5.20}$$

$$\text{QFX } \beta = 600\text{:} \qquad A \cdot t = 1.09 \cdot m^{1.372}\, MBq \times min \tag{5.21}$$

These two potential TAP protocols along with the TAP used to scan the patients in this study are shown in figure 5.11.

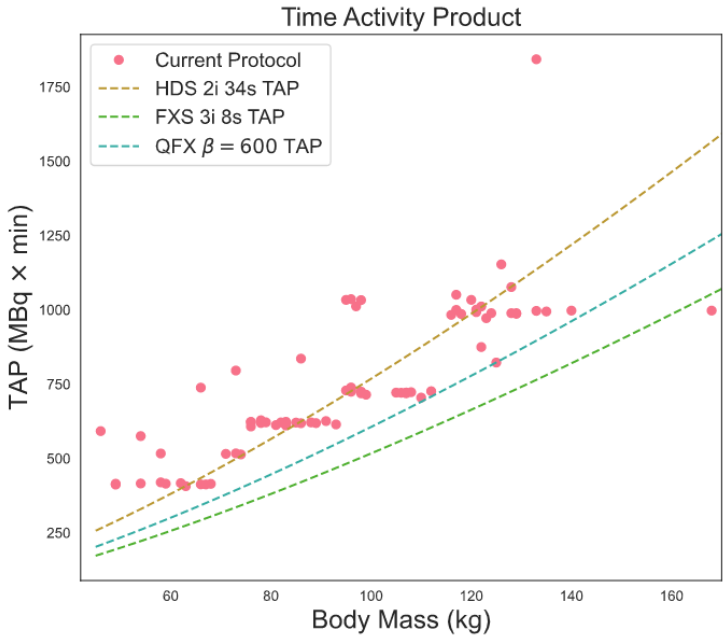

Figure 5.11: **New Activity Protocols:** TAP protocols based on equations 5.19, 5.20, and 5.21 for the current clinically used reconstruction (HDS 2i 34s), optimized FXS 3i 8s, and QFX $\beta = 600$, respectively. The TAP used in the patient study is also shown.

Body Mass (kg)	HDS 2i 34s TAP (MBq ×min)	FXS 3i 8s TAP (MBq ×min)	QFX $\beta = 600$ TAP (MBq ×min)
50	296.8	199.7	233.6
75	517.6	348.3	407.4
100	768.2	516.9	604.5
125	1043.3	702.1	821.1
150	1339.8	901.6	1054.4

Table 5.2: **TAP**: time-activity products calculated using equations 5.19, 5.20, and 5.21 for several patient body masses.

Patient Dependent Parameter	Discovery MI							
	OSEM + PSF (HDS)				OSEM + PSF + TOF (FXS)			
	a	**b**	**R^2**	**Bartlett's p-value**	**a**	**b**	**R^2**	**Bartlett's p-value**
Patient body mass	10.268	**0.686***	0.703	-	12.234	0.777	0.621	-
Body Surface Area	1.092	1.145	0.678	<0.001	1.032	1.390	0.611	<0.001
Body Mass Index	9.969	0.910	0.591	0.116	4.896	0.761	0.506	<0.001
Mass per Length	11.459	0.813	0.683	0.101	9.075	0.811	0.590	<0.001
Lean Body Mass (Boer)	9.341	0.728	0.538	0.004	14.937	0.897	0.519	0.002
Fat Mass (Boer)	1.371	0.332	0.450	<0.001	0.816	0.238	0.396	<0.001
Lean Body Mass (Hume)	13.449	0.827	0.579	<0.001	24.433	1.030	0.543	<0.001
Fat Mass (Hume)	1.371	0.332	0.450	<0.001	0.816	0.238	0.396	<0.001
Lean Body Mass (James)	7.390	0.673	0.401	<0.001	8.244	0.755	0.400	<0.001
Fat Mass (James)	1.556	0.369	0.578	<0.001	0.981	0.294	0.463	<0.001
Parameter	D690							
	OSEM + PSF (HDS)				OSEM + PSF + TOF (FXS)			
	a	**b**	**R^2**	**Bartlett's p-value**	**a**	**b**	**R^2**	**Bartlett's p-value**
Patient body mass	26.523	0.939	0.759	-	12.354	0.812	0.701	-
Body Surface Area	1.229	1.592	0.739	<0.001	0.804	1.291	0.618	<0.001
Body Mass Index	15.183	1.074	0.636	<0.001	4.320	0.762	0.628	<0.001
Mass per Length	26.544	1.067	0.737	0.786	11.396	0.899	0.738	0.732
Lean Body Mass (Boer)	23.114	1.010	0.590	<0.001	3.358	0.592	0.358	<0.001
Fat Mass (Boer)	1.739	0.448	0.504	<0.001	0.935	0.322	0.611	<0.001
Lean Body Mass (Hume)	37.484	1.138	0.647	<0.001	6.632	0.764	0.435	<0.001
Fat Mass (Hume)	1.739	0.448	0.504	<0.001	0.935	0.322	0.611	<0.001
Lean Body Mass (James)	9.922	0.813	0.388	<0.001	1.337	0.373	0.180	<0.001
Fat Mass (James)	1.704	0.440	0.620	<0.001	0.929	0.318	0.629	<0.001

Table 5.3: **Fit of SNR_L**: Fit parameters are shown for Discovery MI and D690 scanners with both non-TOF and TOF reconstructions.*b value chosen for scaling time activity product with patient body mass.

The mean hepatic activity concentration measured in the patients scanned on the Discovery MI was 5.4 kBq/mL (the 95% confidence interval ranged from 3.2 to 7.7 kBq/mL). The mean activity concentration normalized by injected activity per mass was 1.74 (kBq/mL)/(MBq/kg). These results were compared with the NEMA phantom filling assumptions made in the previous chapter. A measured hepatic activity concentration of 2.0 kBq/mL would be consistent with a 75 kg patient administered ~86 MBq FDG 1 hour prior to scanning. Figure 5.12 shows the assumptions made by Gnesin *et al.* [60] and Boellaard[51] and the measured data from our cohort of patients. The assumption made by Boellaard is for an average whole body activity concentration, not specifically the liver activity concentration.

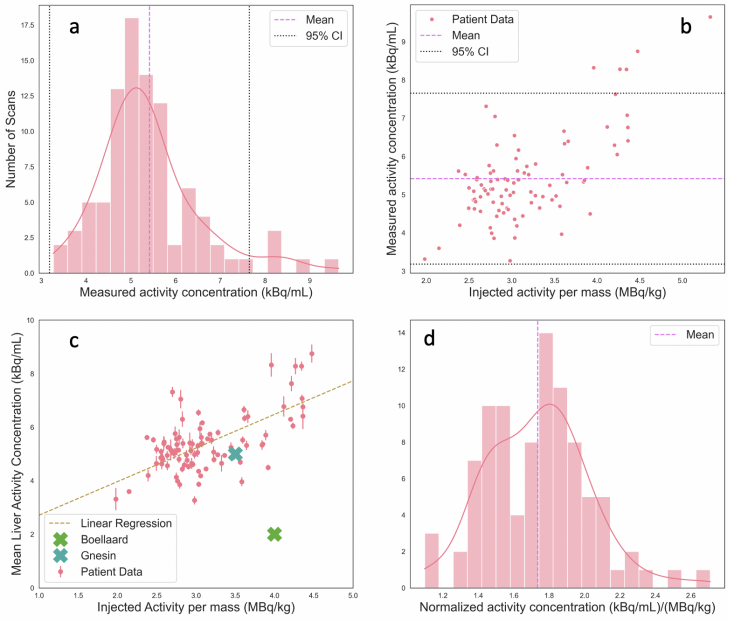

Figure 5.12: **Hepatic Activity Concentration**: measured from TOF scans **(a)**, plotted as a function of injected activity per mass **(b,c)**, and normalized by injected activity per mass **(d)**.

5.4 Discussion

In this study, our results showed that for the current clinical scanning protocols, SNR_L decreases with patient body mass for patients scanned on both the Discovery MI and D690. This suggests that the current TAP protocol used for scanning patients on both scanners is not providing consistent image quality.

The patient dependent parameter with the highest correlation between TAP and SNR_L for both non-TOF and TOF reconstructions was patient body mass. Body surface area was the parameter with the second highest R^2 though the result of the Bartlett's test showed statistical significance ($p<0.001$). COV was also modeled with a power law fit but the correlation between anatomical characteristics (including patient mass) and TAP was much lower (0.15 and 0.40 for non-TOF and TOF, respectively). This may be because the four VOIs used to calculate COV do not represent a sufficient number of noise realizations. However, it is not practical to draw additional non-overlapping ROIs in the liver of most patients.

In their work, de Groot *et al.* suggest that TAP should be scaled quadratically with patient body mass. The study presented here found that TAP be scaled by patient body mass (m) to the power of 1.88 ± 0.08 and 1.62 ± 0.14 (where the error is equal to one standard deviation of the fit) for non-TOF and TOF scans acquired with the D690, respectively. For scans acquired with the newer Discovery MI, the exponent was found to be 1.37 ± 0.08 and 1.55 ± 0.12. These results are more consistent with the ones presented by Wickham *et al.* [23], that scaling activity by $m^{1.6}$ is necessary using TOF reconstructions and by Machado *et al.* [21] that scaling regimens between $m^{1.0}$ and $m^{1.5}$ should be used for non-TOF reconstructions in order to achieve consistent image quality. The source of the discrepancy in the optimal exponent found for the scanners and reconstructions in this study is not clear, but may be related to the same number of iterations and subsets being used for both reconstructions (2 iterations, 34 subsets). This may help to explain why the TOF results from the Discovery MI suggest a higher exponent of patient body mass is required than with the non-TOF scans. As can be seen in figure 4.9, for high numbers of iterative updates, TOF scans exhibit greater noise levels than non-TOF scans. It should again be noted that not every patient scan included in this study was scanned with both non-TOF and TOF reconstructions.

A new TAP protocol was developed (equation 5.19) based on a $SNR_{acc} = 10$. In combination with the NEMA phantom study that investigated different reconstruction parameters, scaled TAP protocols (equations 5.20 and 5.21) are also recommended. The first protocol could be implemented without changing the reconstruction methods used clinically. The latter TAP protocols, however, are not applicable to the reconstruction methods used to acquire the patient images in this study and should only be implemented in conjunction with the optimized FXS and QFX reconstructions detailed in the previous chapter. The improvement in noise and bias of the optimized reconstruction should allow lower TAP values while maintaining the same level of image quality.

This study found the mean hepatic activity concentration in patients administered with FDG to be 5.4 kBq/mL. This is inconsistent with the NEMA phantom preparation assumptions made by EARL and referenced in the previous chapter [51]. The mean hepatic activity concentration normalized by the injected activity per mass was used to update this assumption. This new assumption along with an optimized reconstruction method predicts that very low injected activities (~86 MBq for a 75 kg patient) are sufficient to achieve target image quality. Further investigation of this assumption with anthropomorphic phantom studies are required to establish the relationship between phantom and patient injected activity levels.

5.4.1 Limits:

One limitation of this study is that it assumes NECR to have a linear relationship with injected activity (as shown for activity concentrations less than 40 kBq/cc in figure 2.10). While this is likely true, it should be validated by calculating the NECR for each patient. Calculation of NECR requires accurate estimates of prompt counts, random counts, and scatter fraction, none of which were available from the reconstructed and anonymized patient data used in this study. In the future, these fields, as well as detector dead time should be obtained. Using this data, patient specific NECR curves could then be estimated, as described by Danna *et al.* [70] and Stearns [71], to verify that injected activity could be increased without diminishing counting statistics.

The choice of SNR_{acc} used to determine the TAP in equations 5.19 - 5.21 was not informed by physician experience as in de Groot's work [22]. Further, values of SNR found to be acceptable with one reconstruction method may not be generalized to other reconstructions. Because this work is recommending the clinical adoption of a new reconstruction method based on the NEMA phantom study, the value of SNR_{acc} may have limited utility. Tables of injected activity for a range of patient body mass, bed durations, and SNR values are displayed in the appendix.

5.5 Conclusions

The first aim of this work was to characterize the relationship between injected activity protocols and image quality for a Discovery MI and a D690 scanner. Then, using this relationship, a new TAP protocol would be developed in an attempt to achieve consistent image quality for all patients, independent of their anatomy.

This was done by conducting a retrospective image quality study of [^{18}F]FDG PET/CT scans acquired at BC Cancer. It was determined that under the current scanning protocols, SNR_L decreases with patient body mass. The relationship between SNR_L and several patient dependent parameters was investigated leading to the finding that scaling the product of injected [^{18}F]FDG activity and scan duration as $m^{1.37}$ and $m^{1.88}$ for the Discovery MI and D690, respectively.

Chapter 6

Conclusions

The work performed in this MSc project and presented in this thesis aimed to improve the image quality and quantitative value of [^{18}F]FDG PET/CT images acquired in BC Cancer. In pursuit of this goal, the quality assurance of the CT scanner as well as the reconstruction methods for PET and injected activities of [^{18}F]FDG were considered.

The first step in this project was the development of software to enable automated image analysis of CT images. The software was designed to analyze images of the QA phantom scanned by technologists daily. Implementing this software clinically will allow for quantitative tracking of the CT scanner performance based on metrics such as modulation transfer function, low contrast detectability, and laser alignment. Further, because this phantom is widely used on standalone CT scanners in addition to the PET/CT scanners in BC Cancer, this software tool could be used to standardize quality assurance procedures for CT more generally.

The next step was to optimize the reconstruction methods for whole body [^{18}F]FDG PET using scans of the NEMA IQ phantom. The new scanners at BC Cancer possess advanced detector technology as well as a new generation of reconstruction algorithms which required investigation to determine the best parameters for patient scanning. By analyzing images of the phantom with known activity concentrations, it was possible to determine the reconstruction parameters that minimized both noise and bias. Based on this study, optimized reconstruction parameters were chosen for TOF OSEM reconstructions (FXS) and TOF BSREM reconstructions (QFX). By adopting these reconstruction methods clinically, it will be possible to obtain images of higher image quality and lower bias while delivering less dose to patients.

Finally, a retrospective image quality study was conducted using patient [^{18}F]FDG PET images previously acquired in Victoria and Vancouver. The image quality of each patient scan was assessed by measuring the signal-to-noise ratio in the liver (SNR_L). The relationship between image quality and a variety of patient dependent parameters was then investigated. Patient body mass was found to be the parameter best correlated with SNR_L. This relationship was then used to determine the optimum injected activity of [^{18}F]FDG and scaling regimen that would result in consistent image quality, independent of patient body mass. This injected activity protocol was also scaled by the results of the NEMA phantom study to reflect the reduction in patient dose that is possible by using optimized reconstruction methods.

After implementing the new reconstruction methods and injected activity protocol described in this work, verification of patient image quality should be conducted. The patient image quality study detailed in chapter 5 should be repeated after a sufficient number of patient scans are acquired using the proposed optimized scanning protocols.

Bibliography

[1] Jerrold T. Bushberg, J. Anthony Seibert, Edwin M. Leidholdt, John M. Boone, and Edward J. Goldschmidt. *The Essential Physics of Medical Imaging*, volume 30. 2003.

[2] W. Tania Rahman, Daniel J. Wale, Benjamin L. Viglianti, Danyelle M. Townsend, Matthew S. Manganaro, Milton D. Gross, Ka Kit Wong, and Domenico Rubello. The impact of infection and inflammation in oncologic 18F-FDG PET/CT imaging. *Biomedicine and Pharmacotherapy*, 117(June):109168, 2019.

[3] Sina Houshmand, Ali Salavati, Sandip Basu, Benjapa Khiewvan, and Abass Alavi. The role of dual and multiple time point imaging of FDG uptake in both normal and disease states. *Clinical and Translational Imaging*, 2(4):281–293, 2014.

[4] Ramsey Badawi. Introduction to PET Physics, 1999.

[5] Paul Lecoq. The 10ps Time-of-Flight PET Challenge, 2019.

[6] A. Del Guerra, N. Belcari, and M. Bisogni. Positron emission tomography: Its 65 years. *Rivista del Nuovo Cimento*, 39(4):155–223, 2016.

[7] Gopal B. Saha, PhD. *Basics of PET Imaging.* 2016.

[8] Ronald T. Droege and Richard L. Morin. A practical method to measure the mtf of ct scanners. *Medical Physics*, 9(5):758–760, 1982.

[9] GE Healthcare. Discovery MI ^{TM}. 2016.

[10] RL Wahl. *Principles and Practice of PET and PET/CT*. Lippincott Williams amp; Wilkins, 2nd ed. edition, 2008.

[11] Søren Hess, Björn A. Blomberg, Hongyun June Zhu, Poul Flemming Høilund-Carlsen, and Abass Alavi. The Pivotal Role of FDG-PET/CT in Modern Medicine. *Academic Radiology*, 21(2):232–249, 2014.

[12] Sanjiv S Gambhir, Johannes Czernin, Judy Schwimmer, Daniel H S Silverman, R Edward Coleman, and Michael E Phelps. Gambhir SS, Czernin J, Schwimmer J, Silverman DH, Coleman RE, Phelps ME.A Tabulated Summary of the FDG PET Literature. *J Nucl Med*, 42:1–93, 2001.

[13] Wolfgang A. Weber. Use of PET for monitoring cancer therapy and for predicting outcome. *Journal of Nuclear Medicine*, 46(6):983–995, 2005.

[14] Vincent Grégoire, Karin Haustermans, Xavier Geets, Sarah Roels, and Max Lonneux. PET-Based Treatment Planning in Radiotherapy: A New Standard? 48(1):68–77, 2007.

[15] Simona Ben-Haim and Peter Ell. 18F-FDG PET and PET/CT in the evaluation of cancer treatment response. *Journal of Nuclear Medicine*, 50(1):88–99, 2009.

[16] Georg Kuhnert, Ronald Boellaard, Sergej Sterzer, Deniz Kahraman, Matthias Scheffler, Jürgen Wolf, Markus Dietlein, Alexander Drzezga, and Carsten Kobe. Impact of PET/CT image reconstruction methods and liver uptake normalization strategies on quantitative image analysis. *European Journal of Nuclear Medicine and Molecular Imaging*, 43(2):249–258, 2016.

[17] Elin Lindström, Anders Sundin, Carlos Trampal, Lars Lindsjö, Ezgi Ilan, Torsten Danfors, Gunnar Antoni, Jens Sörensen, and Mark Lubberink. Evaluation of penalized-likelihood estimation reconstruction on a digital time-of-flight PET/CT scanner for 18 F-FDG whole-body examinations. *Journal of Nuclear Medicine*, 59(7):1152–1158, 2018.

[18] Elena Prieto, María José García-Velloso, Macarena Rodríguez-Fraile, Verónica Morán, Berta García-García, Fernando Guillén, María Isabel Morales, Lidia Sancho, Iván Peñuelas, José Ángel Richter, and Josep María Martí-Climent. Significant dose reduction is feasible in FDG PET/CT protocols without compromising diagnostic quality. *Physica Medica*, 46(February):134–139, 2018.

[19] Benjamin S. Halpern, Magnus Dahlbom, Andrew Quon, Christian Schiepers, Christian Waldherr, Daniel H. Silverman, Osman Ratib, and Johannes Czernin. Impact of patient weight and emission scan duration on PET/CT image

quality and lesion detectability. *Journal of Nuclear Medicine*, 45(5):797–801, 2004.

[20] Hendrik Everaert, Christian Vanhove, Tony Lahoutte, Kristoff Muylle, Vicky Caveliers, Axel Bossuyt, and Philippe R. Franken. Optimal dose of 18F-FDG required for whole-body PET using an LSO PET camera. *European Journal of Nuclear Medicine and Molecular Imaging*, 30(12):1615–1619, 2003.

[21] Marcos A.D. Machado, Vinícius O. Menezes, Mauro Namías, Naiara S. Vieira, Cleiton C. Queiroz, Roberta Matheoud, Adam M. Alessio, and Mércia L. Oliveira. Protocols for harmonized quantification and noise reduction in low-dose oncologic 18F-FDG PET/CT imaging. *Journal of Nuclear Medicine Technology*, 47(1):47–54, 2019.

[22] Eleonore H. de Groot, Nieky Post, Ronald Boellaard, Nils R.L. Wagenaar, Antoon T.M. Willemsen, and Jorn A. van Dalen. Optimized dose regimen for whole-body FDG-PET imaging. *EJNMMI Research*, 3(1):1–11, 2013.

[23] Fred Wickham, Helena McMeekin, Maria Burniston, Daniel McCool, Deborah Pencharz, Annah Skillen, and Thomas Wagner. Patient-specific optimisation of administered activity and acquisition times for 18 F-FDG PET imaging. *EJNMMI Research*, 7(1), 2017.

[24] Maurizio Conti and Lars Eriksson. Physics of pure and non-pure positron emitters for PET: A review and a discussion. *EJNMMI Physics*, 3(1), 2016.

[25] Thomas W. Barber, Kenneth S.K. Yap, Martin H. Cherk, Anne Powell, and Victor Kalff. Comparison of positron emission tomography/CT and bremsstrahlung imaging following Y-90 radiation synovectomy. *Journal of Medical Imaging and Radiation Oncology*, 57(5):567–571, 2013.

[26] Lise Meitner. A Simple Method for the Investigation of Secondary Electrons Excited by q-Rays and the Interference of These Electrons with Measurements of Primary Beta-Ray Spectra. *Physical Review*, 63:63–66, 1943.

[27] Ramesh Chandra and Arman Rahmim. *Nuclear Medicine Physics: The Basics*. 2018.

[28] Michael E. Phelps. *PET*. Springer New York, 2004.

[29] Terry Jones and David Townsend. History and future technical innovation in positron emission tomography. *Journal of Medical Imaging*, 4(1):011013, 2017.

[30] JW Keyes Jr. SUV: standard uptake or silly useless value? *Journal of Nuclear Medicine*, 36(10):1836–1839, 1995.

[31] Martin A. Lodge. Repeatability of SUV in oncologic 18F-FDG PET. *Journal of Nuclear Medicine*, 58(4):523–532, 2017.

[32] Arman Rahmim, Ju Chieh Cheng, Stephan Blinder, Maurie Laure Camborde, and Vesna Sossi. Statistical dynamic image reconstruction in state-of-the-art high-resolution PET. *Physics in Medicine and Biology*, 50(20):4887–4912, 2005.

[33] Arman Rahmim and Jing Tang. Noise propagation in resolution modeled PET imaging and its impact on detectability. *Physics in Medicine and Biology*, 58(19):6945–6968, 2013.

[34] H Malcolm Hudson and Richard S Larkin. Ordered Subsets of Projection Data. *IEEE transactions on medical imaging*, 13(4):601–609, 1994.

[35] A. Michael Morey and Dan J. Kadrmas. Effect of varying number of OSEM subsets on PET lesion detectability. *Journal of Nuclear Medicine Technology*, 41(4):268–273, 2013.

[36] Yang-Ming Zhu. Ordered subset expectation maximization algorithm for positron emission tomographic image reconstruction using belief kernels. *Journal of Medical Imaging*, 5(04):1, 2018.

[37] Sangtae Ahn and Jeffrey A. Fessler. Globally convergent image reconstruction for emission tomography using relaxed ordered subsets algorithms. *IEEE Transactions on Medical Imaging*, 22(5):613–626, 2003.

[38] Paulo R.R.V. Caribé, M. Koole, Yves D'Asseler, B. Van Den Broeck, and S. Vandenberghe. Noise reduction using a Bayesian penalized-likelihood reconstruction algorithm on a time-of-flight PET-CT scanner. *EJNMMI Physics*, 6(1), 2019.

[39] Judit Lantos, Erik Mittra, Craig Levin, and Andrei Iagaru. Standard OSEM vs. regularized PET image reconstruction: qualitative and semi-quantitative comparison. *Journal of Nuclear Medicine*, 56(supplement 3):1805, 2015.

[40] Patrizio Barca, Marco Giannelli, Maria Evelina Fantacci, and Davide Caramella. Computed tomography imaging with the Adaptive Statistical Iterative Reconstruction (ASIR) algorithm: dependence of image quality on the blending level of reconstruction. *Australasian Physical and Engineering Sciences in Medicine*, 41(2):463–473, 2018.

[41] A. Nassalski, M. Kapusta, T. Batsch, D. Wolski, D. Möckel, W. Enghardt, and M. Moszyński. Comparative study of scintillators for PET/CT detectors. *IEEE Transactions on Nuclear Science*, 54(1):3–10, 2007.

[42] Egbert Buhr, Susanne Guenther-Kohfahl, and Ulrich Neitzel. Simple method for modulation transfer function determination of digital imaging detectors from edge images. *Medical Imaging 2003: Physics of Medical Imaging*, 5030:877, 2003.

[43] Hoen Oh Shin, Christian V. Falck, and Michael Galanski. Low-contrast detectability in volume rendering: A phantom study on multidector-row spiral CT data. *European Radiology*, 14(2):341–349, 2004.

[44] Technical Reference Manual. Revolution EVO Technical Reference Manual. 2014.

[45] Darcy Mason, Scaramallion, Rhaxton, Mrbean-Bremen, Jonathan Suever, Vanessasaurus, Guillaume Lemaitre, Dimitri Papadopoulos Orfanos, Aditya Panchal, Joan Massich, Alex Rothberg, Korijn Van Golen, James Kerns, Thomas Robitaille, Matthew Shun-Shin, Moloney, Pawelzajdel, Markus Mattes, Markus D. Herrmann, Félix C. Morency, Huicpc0207, Ferdymercury, Colonelfazackerley, Masahiro Wada, Kevin S. Hahn, Hans Meine, Chris Bridge, Callan Bryant, Andrey Fedorov, and Adam Klimont. pydicom/pydicom: v1.4.1, 2020.

[46] Travis E Oliphant. *A guide to NumPy*, volume 1. Trelgol Publishing USA, 2006.

[47] John D. Hunter. Matplotlib: A 2d graphics environment. *Computing in Science & Engineering*, 9(3):90–95, 2007.

[48] Jeff Reback, Wes McKinney, Jbrockmendel, Joris Van Den Bossche, Tom Augspurger, Phillip Cloud, Gfyoung, Sinhrks, Adam Klein, Matthew Roeschke, Jeff Tratner, Chang She, William Ayd, Simon Hawkins, Terji Petersen, Jeremy Schendel, Andy Hayden, Marc Garcia, Vytautas Jancauskas, MomIsBestFriend, Pietro Battiston, Skipper Seabold, Chris-B1, H-Vetinari, Stephan

Hoyer, Wouter Overmeire, Alimcmaster1, Mortada Mehyar, Christopher Whelan, and Thomas Kluyver. pandas-dev/pandas: Pandas 1.0.0, 2020.

[49] Jun Zhang, Piotr Maniawski, and Michael V. Knopp. Performance evaluation of the next generation solid-state digital photon counting PET/CT system. *EJNMMI Research*, 8, 2018.

[50] Ronald Boellaard, Mike J. O'Doherty, Wolfgang A. Weber, Felix M. Mottaghy, Markus N. Lonsdale, Sigrid G. Stroobants, Wim J.G. Oyen, Joerg Kotzerke, Otto S. Hoekstra, Jan Pruim, Paul K. Marsden, Klaus Tatsch, Corneline J. Hoekstra, Eric P. Visser, Bertjan Arends, Fred J. Verzijlbergen, Josee M. Zijlstra, Emile F.I. Comans, Adriaan A. Lammertsma, Anne M. Paans, Antoon T. Willemsen, Thomas Beyer, Andreas Bockisch, Cornelia Schaefer-Prokop, Dominique Delbeke, Richard P. Baum, Arturo Chiti, and Bernd J. Krause. FDG PET and PET/CT: EANM procedure guidelines for tumour PET imaging: Version 1.0. *European Journal of Nuclear Medicine and Molecular Imaging*, 37(1):181–200, 2010.

[51] R Boellaard, AT Willemsen, B Arends, and E P Visser. EARL procedure for assessing PET/CT system specific patient FDG activity preparations for quantitative FDG PET/CT studies. *April 2013*, pages 1–3, 2010.

[52] Daniëlle Koopman, Jochen A.C. van Osch, Pieter L. Jager, Carlijn J.A. Tenbergen, Siert Knollema, Cornelis H. Slump, and Jorn A. van Dalen. Technical note: how to determine the FDG activity for tumour PET imaging that satisfies European guidelines. *EJNMMI Physics*, 3(1), 2016.

[53] Alexandre Chicheportiche, Rami Marciano, and Marina Orevi. Comparison of NEMA characterizations for Discovery MI and Discovery MI-DR TOF PET/CT systems at different sites and with other commercial PET/CT systems. *EJNMMI Physics*, 7(1), 2020.

[54] Teaghan O'Briain and Alexander Hart. EARL NEMA. https://github.com/teaghan/earl_nema, 2020.

[55] Andres Kaalep, Terez Sera, Sjoerd Rijnsdorp, Maqsood Yaqub, Anne Talsma, Martin A. Lodge, and Ronald Boellaard. Feasibility of state of the art PET/CT systems performance harmonisation. *European Journal of Nuclear Medicine and Molecular Imaging*, 45(8):1344–1361, 2018.

[56] Stéfan van der Walt, Johannes L Schönberger, Juan Nunez-Iglesias, François Boulogne, Joshua D Warner, Neil Yager, Emmanuelle Gouillart, Tony Yu, and The scikit-image contributors. scikit-image: image processing in Python. *PeerJ*, 2:e453, 2014.

[57] Martin Lodge and R Wahl. Quantifying metabolic tumor response to therapy: Total lesion glycolysis and partial volume reduction. *Journal of Nuclear Medicine*, 50(supplement 2):237–237, may 2009.

[58] Charles C. Watson, Michael E. Casey, Bernard Bendriem, Jonathan P. Carney, David W. Townsend, Stefan Eberl, Steve Meikle, and Frank P. DiFilippo. Optimizing injected dose in clinical PET by accurately modeling the counting-rate response functions specific to individual patient scans. *Journal of Nuclear Medicine*, 46(11):1825–1834, 2005.

[59] Tinsu Pan, Samuel A. Einstein, Srinivas Cheenu Kappadath, Kira S. Grogg, Cristina Lois Gomez, Adam M. Alessio, William C. Hunter, Georges El Fakhri, Paul E. Kinahan, and Osama R. Mawlawi. Performance evaluation of the 5-Ring GE Discovery MI PET/CT system using the national electrical manufacturers association NU 2-2012 Standard. *Medical Physics*, 46(7):3025–3033, 2019.

[60] Silvano Gnesin, Christine Kieffer, Konstantinos Zeimpekis, Jean Pierre Papazyan, Renaud Guignard, John O. Prior, Francis R. Verdun, and Thiago V.M. Lima. Phantom-based image quality assessment of clinical 18F-FDG protocols in digital PET/CT and comparison to conventional PMT-based PET/CT. *EJNMMI Physics*, 7(1):1–16, 2020.

[61] Saeed Ashrafinia, Hassan Mohy-Ud-Din, Nicolas A. Karakatsanis, Abhinav K. Jha, Michael E. Casey, Dan J. Kadrmas, and Arman Rahmim. Generalized PSF modeling for optimized quantitation in PET imaging. *Physics in Medicine and Biology*, 62(12):5149–5179, 2017.

[62] Tingting Chang, Guoping Chang, John W. Clark, Rami H. Diab, Eric Rohren, and Osama R. Mawlawi. Reliability of predicting image signal-to-noise ratio using noise equivalent count rate in PET imaging. *Medical Physics*, 39(10):5891–5900, 2012.

[63] Ronald Boellaard, Roberto Delgado-Bolton, Wim J.G. Oyen, Francesco Giammarile, Klaus Tatsch, Wolfgang Eschner, Fred J. Verzijlbergen, Sally F. Bar-

rington, Lucy C. Pike, Wolfgang A. Weber, Sigrid Stroobants, Dominique Delbeke, Kevin J. Donohoe, Scott Holbrook, Michael M. Graham, Giorgio Testanera, Otto S. Hoekstra, Josee Zijlstra, Eric Visser, Corneline J. Hoekstra, Jan Pruim, Antoon Willemsen, Bertjan Arends, Jörg Kotzerke, Andreas Bockisch, Thomas Beyer, Arturo Chiti, and Bernd J. Krause. FDG PET/CT: EANM procedure guidelines for tumour imaging: version 2.0. *European Journal of Nuclear Medicine and Molecular Imaging*, 42(2):328–354, 2015.

[64] Nicolas A Karakatsanis, Eleni Fokou, and Charalampos Tsoumpas. Dosage optimization in positron emission tomography: state-of-the-art methods and future prospects. *American journal of nuclear medicine and molecular imaging*, 5(5):527–47, 2015.

[65] Jianhua Yan, Josh Schaefferkoette, Maurizio Conti, and David Townsend. A method to assess image quality for Low-dose PET: Analysis of SNR, CNR, bias and image noise. *Cancer Imaging*, 16(1):1–12, 2016.

[66] Richard L. Wahl, Heather Jacene, Yvette Kasamon, and Martin A. Lodge. From RECIST to PERCIST: Evolving considerations for PET response criteria in solid tumors. *Journal of Nuclear Medicine*, 50(SUPPL. 1):122–151, 2009.

[67] Karen M. Fancher, Alicia J. Sacco, Robert C. Gwin, Luke K. Gormley, and Caitlin B. Mitchell. Comparison of two different formulas for body surface area in adults at extremes of height and weight. *Journal of Oncology Pharmacy Practice*, 22(5):690–695, 2016.

[68] Damiano Caruso, Domenico De Santis, Flaminia Rivosecchi, Marta Zerunian, Nicola Panvini, Marta Montesano, Tommaso Biondi, Davide Bellini, Marco Rengo, and Andrea Laghi. Lean Body Weight-Tailored Iodinated Contrast Injection in Obese Patient: Boer versus James Formula. *BioMed Research International*, 2018, 2018.

[69] R. Hume. Prediction of lean body mass from height and weight. *Journal of clinical pathology*, 19(4):389–391, 1966.

[70] M. Danna, M. Lecchi, V. Bettinardi, M. C. Gilardi, C. W. Stearns, G. Lucignani, and F. Fazio. Generation of the acquisition-specific NEC (AS-NEC) curves to optimize the injected dose in 3D 18F-FDG whole body PET studies. *IEEE Transactions on Nuclear Science*, 53(1):86–92, 2006.

[71] Charles W. Stearns. Estimating an acquisition-specific NEC curve for PET acquisitions. *IEEE Nuclear Science Symposium Conference Record*, 4:2578–2580, 2003.

Appendix A

[^{18}F]FDG Injected Activity Tables

A.1 Injected Activity (MBq): Discovery MI - HDS 2i 34s 6.4mm FWHM

The following tables display the [^{18}F]FDG injected activity in MBq for the current clinically used reconstruction, HDS 2i 34s 6.4mm FWHM as well as the optimized reconstruction methods FXS 3i 8s 3.2mm FWHM and QFX $\beta = 600$ required to provide consistent signal-to-noise ratio in the liver (SNR_L). Injected activity levels are tabulated for $SNR_L = 5$, 8, 10, 12, and 15 as well as bed durations from 1 to 5 min in 0.5 min increments.

SNR = 5									
Body Mass	**Bed Duration (min)**								
(kg)	**1**	**1.5**	**2**	**2.5**	**3**	**3.5**	**4**	**4.5**	**5**
10	8.2	5.4	4.1	3.3	2.7	2.3	2.0	1.8	1.6
12	10.5	7.0	5.2	4.2	3.5	3.0	2.6	2.3	2.1
14	12.9	8.6	6.5	5.2	4.3	3.7	3.2	2.9	2.6
16	15.5	10.4	7.8	6.2	5.2	4.4	3.9	3.5	3.1
18	18.3	12.2	9.1	7.3	6.1	5.2	4.6	4.1	3.7
20	21.1	14.1	10.6	8.4	7.0	6.0	5.3	4.7	4.2
22	24.1	16.0	12.0	9.6	8.0	6.9	6.0	5.3	4.8
24	27.1	18.1	13.6	10.8	9.0	7.7	6.8	6.0	5.4
26	30.3	20.2	15.1	12.1	10.1	8.6	7.6	6.7	6.1
28	33.5	22.3	16.8	13.4	11.2	9.6	8.4	7.4	6.7
30	36.8	24.6	18.4	14.7	12.3	10.5	9.2	8.2	7.4
32	40.2	26.8	20.1	16.1	13.4	11.5	10.1	8.9	8.0
34	43.7	29.2	21.9	17.5	14.6	12.5	10.9	9.7	8.7
36	47.3	31.5	23.7	18.9	15.8	13.5	11.8	10.5	9.5
38	50.9	34.0	25.5	20.4	17.0	14.6	12.7	11.3	10.2
40	54.7	36.4	27.3	21.9	18.2	15.6	13.7	12.1	10.9
42	58.4	39.0	29.2	23.4	19.5	16.7	14.6	13.0	11.7
44	62.3	41.5	31.1	24.9	20.8	17.8	15.6	13.8	12.5
46	66.2	44.1	33.1	26.5	22.1	18.9	16.6	14.7	13.2
48	70.2	46.8	35.1	28.1	23.4	20.1	17.5	15.6	14.0
50	74.2	49.5	37.1	29.7	24.7	21.2	18.6	16.5	14.8
52	78.3	52.2	39.2	31.3	26.1	22.4	19.6	17.4	15.7
54	82.5	55.0	41.3	33.0	27.5	23.6	20.6	18.3	16.5
56	86.7	57.8	43.4	34.7	28.9	24.8	21.7	19.3	17.3
58	91.0	60.7	45.5	36.4	30.3	26.0	22.8	20.2	18.2
60	95.3	63.6	47.7	38.1	31.8	27.2	23.8	21.2	19.1
62	99.7	66.5	49.9	39.9	33.2	28.5	24.9	22.2	19.9
64	104.2	69.4	52.1	41.7	34.7	29.8	26.0	23.1	20.8
66	108.7	72.4	54.3	43.5	36.2	31.0	27.2	24.1	21.7
68	113.2	75.5	56.6	45.3	37.7	32.3	28.3	25.2	22.6
70	117.8	78.5	58.9	47.1	39.3	33.7	29.4	26.2	23.6
72	122.4	81.6	61.2	49.0	40.8	35.0	30.6	27.2	24.5
74	127.1	84.7	63.6	50.8	42.4	36.3	31.8	28.2	25.4
76	131.9	87.9	65.9	52.7	44.0	37.7	33.0	29.3	26.4
78	136.6	91.1	68.3	54.7	45.5	39.0	34.2	30.4	27.3
80	141.5	94.3	70.7	56.6	47.2	40.4	35.4	31.4	28.3
82	146.3	97.6	73.2	58.5	48.8	41.8	36.6	32.5	29.3
84	151.3	100.8	75.6	60.5	50.4	43.2	37.8	33.6	30.3
86	156.2	104.1	78.1	62.5	52.1	44.6	39.1	34.7	31.2
88	161.2	107.5	80.6	64.5	53.7	46.1	40.3	35.8	32.2
90	166.3	110.9	83.1	66.5	55.4	47.5	41.6	37.0	33.3
92	171.4	114.2	85.7	68.5	57.1	49.0	42.8	38.1	34.3
94	176.5	117.7	88.3	70.6	58.8	50.4	44.1	39.2	35.3
96	181.7	121.1	90.8	72.7	60.6	51.9	45.4	40.4	36.3
98	186.9	124.6	93.4	74.8	62.3	53.4	46.7	41.5	37.4
100	192.1	128.1	96.1	76.9	64.0	54.9	48.0	42.7	38.4
102	197.4	131.6	98.7	79.0	65.8	56.4	49.4	43.9	39.5
104	202.8	135.2	101.4	81.1	67.6	57.9	50.7	45.1	40.6
106	208.1	138.8	104.1	83.3	69.4	59.5	52.0	46.3	41.6
108	213.5	142.4	106.8	85.4	71.2	61.0	53.4	47.5	42.7
110	219.0	146.0	109.5	87.6	73.0	62.6	54.7	48.7	43.8
112	224.5	149.6	112.2	89.8	74.8	64.1	56.1	49.9	44.9
114	230.0	153.3	115.0	92.0	76.7	65.7	57.5	51.1	46.0
116	235.5	157.0	117.8	94.2	78.5	67.3	58.9	52.3	47.1
118	241.1	160.7	120.6	96.4	80.4	68.9	60.3	53.6	48.2
120	246.7	164.5	123.4	98.7	82.2	70.5	61.7	54.8	49.3
122	252.4	168.3	126.2	101.0	84.1	72.1	63.1	56.1	50.5
124	258.1	172.1	129.1	103.2	86.0	73.7	64.5	57.4	51.6
126	263.8	175.9	131.9	105.5	87.9	75.4	66.0	58.6	52.8
128	269.6	179.7	134.8	107.8	89.9	77.0	67.4	59.9	53.9
130	275.4	183.6	137.7	110.2	91.8	78.7	68.8	61.2	55.1
132	281.2	187.5	140.6	112.5	93.7	80.3	70.3	62.5	56.2
134	287.1	191.4	143.5	114.8	95.7	82.0	71.8	63.8	57.4
136	293.0	195.3	146.5	117.2	97.7	83.7	73.2	65.1	58.6
138	298.9	199.3	149.5	119.6	99.6	85.4	74.7	66.4	59.8
140	304.9	203.2	152.4	121.9	101.6	87.1	76.2	67.7	61.0
142	310.9	207.2	155.4	124.3	103.6	88.8	77.7	69.1	62.2
144	316.9	211.3	158.4	126.8	105.6	90.5	79.2	70.4	63.4
146	322.9	215.3	161.5	129.2	107.6	92.3	80.7	71.8	64.6
148	329.0	219.3	164.5	131.6	109.7	94.0	82.3	73.1	65.8
150	335.1	223.4	167.6	134.1	111.7	95.8	83.8	74.5	67.0
152	341.3	227.5	170.6	136.5	113.8	97.5	85.3	75.8	68.3
154	347.5	231.6	173.7	139.0	115.8	99.3	86.9	77.2	69.5
156	353.7	235.8	176.8	141.5	117.9	101.0	88.4	78.6	70.7
158	359.9	239.9	179.9	144.0	120.0	102.8	90.0	80.0	72.0
160	366.2	244.1	183.1	146.5	122.1	104.6	91.5	81.4	73.2
162	372.5	248.3	186.2	149.0	124.2	106.4	93.1	82.8	74.5
164	378.8	252.5	189.4	151.5	126.3	108.2	94.7	84.2	75.8
166	385.1	256.8	192.6	154.1	128.4	110.0	96.3	85.6	77.0
168	391.5	261.0	195.8	156.6	130.5	111.9	97.9	87.0	78.3
170	397.9	265.3	199.0	159.2	132.6	113.7	99.5	88.4	79.6
172	404.4	269.6	202.2	161.7	134.8	115.5	101.1	89.9	80.9
174	410.8	273.9	205.4	164.3	136.9	117.4	102.7	91.3	82.2
176	417.3	278.2	208.7	166.9	139.1	119.2	104.3	92.7	83.5
178	423.8	282.6	211.9	169.5	141.3	121.1	106.0	94.2	84.8
180	430.4	286.9	215.2	172.2	143.5	123.0	107.6	95.6	86.1

SNR = 8									
Body Mass	**Bed Duration (min)**								
(kg)	**1**	**1.5**	**2**	**2.5**	**3**	**3.5**	**4**	**4.5**	**5**
10	20.9	13.9	10.4	8.4	7.0	6.0	5.2	4.6	4.2
12	26.8	17.9	13.4	10.7	8.9	7.7	6.7	6.0	5.4
14	33.1	22.1	16.6	13.3	11.0	9.5	8.3	7.4	6.6
16	39.8	26.5	19.9	15.9	13.3	11.4	10.0	8.8	8.0
18	46.8	31.2	23.4	18.7	15.6	13.4	11.7	10.4	9.4
20	54.1	36.0	27.0	21.6	18.0	15.4	13.5	12.0	10.8
22	61.6	41.1	30.8	24.6	20.5	17.6	15.4	13.7	12.3
24	69.4	46.3	34.7	27.8	23.1	19.8	17.4	15.4	13.9
26	77.5	51.7	38.7	31.0	25.8	22.1	19.4	17.2	15.5
28	85.8	57.2	42.9	34.3	28.6	24.5	21.4	19.1	17.2
30	94.3	62.9	47.1	37.7	31.4	26.9	23.6	21.0	18.9
32	103.0	68.7	51.5	41.2	34.3	29.4	25.8	22.9	20.6
34	112.0	74.6	56.0	44.8	37.3	32.0	28.0	24.9	22.4
36	121.1	80.7	60.5	48.4	40.4	34.6	30.3	26.9	24.2
38	130.4	86.9	65.2	52.2	43.5	37.3	32.6	29.0	26.1
40	139.9	93.3	70.0	56.0	46.6	40.0	35.0	31.1	28.0
42	149.6	99.7	74.8	59.8	49.9	42.7	37.4	33.2	29.9
44	159.5	106.3	79.7	63.8	53.2	45.6	39.9	35.4	31.9
46	169.5	113.0	84.7	67.8	56.5	48.4	42.4	37.7	33.9
48	179.7	119.8	89.8	71.9	59.9	51.3	44.9	39.9	35.9
50	190.0	126.7	95.0	76.0	63.3	54.3	47.5	42.2	38.0
52	200.5	133.7	100.3	80.2	66.8	57.3	50.1	44.6	40.1
54	211.2	140.8	105.6	84.5	70.4	60.3	52.8	46.9	42.2
56	222.0	148.0	111.0	88.8	74.0	63.4	55.5	49.3	44.4
58	233.0	155.3	116.5	93.2	77.7	66.6	58.2	51.8	46.6
60	244.1	162.7	122.0	97.6	81.4	69.7	61.0	54.2	48.8
62	255.3	170.2	127.6	102.1	85.1	72.9	63.8	56.7	51.1
64	266.6	177.8	133.3	106.7	88.9	76.2	66.7	59.3	53.3
66	278.1	185.4	139.1	111.3	92.7	79.5	69.5	61.8	55.6
68	289.8	193.2	144.9	115.9	96.6	82.8	72.4	64.4	58.0
70	301.5	201.0	150.8	120.6	100.5	86.2	75.4	67.0	60.3
72	313.4	208.9	156.7	125.4	104.5	89.5	78.4	69.6	62.7
74	325.4	216.9	162.7	130.2	108.5	93.0	81.4	72.3	65.1
76	337.5	225.0	168.8	135.0	112.5	96.4	84.4	75.0	67.5
78	349.8	233.2	174.9	139.9	116.6	99.9	87.4	77.7	70.0
80	362.2	241.4	181.1	144.9	120.7	103.5	90.5	80.5	72.4
82	374.6	249.8	187.3	149.9	124.9	107.0	93.7	83.3	74.9
84	387.2	258.2	193.6	154.9	129.1	110.6	96.8	86.1	77.4
86	399.9	266.6	200.0	160.0	133.3	114.3	100.0	88.9	80.0
88	412.8	275.2	206.4	165.1	137.6	117.9	103.2	91.7	82.6
90	425.7	283.8	212.8	170.3	141.9	121.6	106.4	94.6	85.1
92	438.7	292.5	219.4	175.5	146.2	125.3	109.7	97.5	87.7
94	451.8	301.2	225.9	180.7	150.6	129.1	113.0	100.4	90.4
96	465.1	310.1	232.5	186.0	155.0	132.9	116.3	103.4	93.0
98	478.4	319.0	239.2	191.4	159.5	136.7	119.6	106.3	95.7
100	491.9	327.9	245.9	196.8	164.0	140.5	123.0	109.3	98.4
102	505.4	337.0	252.7	202.2	168.5	144.4	126.4	112.3	101.1
104	519.1	346.0	259.5	207.6	173.0	148.3	129.8	115.3	103.8
106	532.8	355.2	266.4	213.1	177.6	152.2	133.2	118.4	106.6
108	546.7	364.4	273.3	218.7	182.2	156.2	136.7	121.5	109.3
110	560.6	373.7	280.3	224.2	186.9	160.2	140.1	124.6	112.1
112	574.6	383.1	287.3	229.9	191.5	164.2	143.7	127.7	114.9
114	588.8	392.5	294.4	235.5	196.3	168.2	147.2	130.8	117.8
116	603.0	402.0	301.5	241.2	201.0	172.3	150.7	134.0	120.6
118	617.3	411.5	308.6	246.9	205.8	176.4	154.3	137.2	123.5
120	631.7	421.1	315.8	252.7	210.6	180.5	157.9	140.4	126.3
122	646.2	430.8	323.1	258.5	215.4	184.6	161.5	143.6	129.2
124	660.7	440.5	330.4	264.3	220.2	188.8	165.2	146.8	132.1
126	675.4	450.3	337.7	270.2	225.1	193.0	168.9	150.1	135.1
128	690.2	460.1	345.1	276.1	230.1	197.2	172.5	153.4	138.0
130	705.0	470.0	352.5	282.0	235.0	201.4	176.2	156.7	141.0
132	719.9	479.9	360.0	288.0	240.0	205.7	180.0	160.0	144.0
134	734.9	490.0	367.5	294.0	245.0	210.0	183.7	163.3	147.0
136	750.0	500.0	375.0	300.0	250.0	214.3	187.5	166.7	150.0
138	765.2	510.1	382.6	306.1	255.1	218.6	191.3	170.0	153.0
140	780.5	520.3	390.2	312.2	260.2	223.0	195.1	173.4	156.1
142	795.8	530.5	397.9	318.3	265.3	227.4	198.9	176.8	159.2
144	811.2	540.8	405.6	324.5	270.4	231.8	202.8	180.3	162.2
146	826.7	551.1	413.4	330.7	275.6	236.2	206.7	183.7	165.3
148	842.3	561.5	421.1	336.9	280.8	240.7	210.6	187.2	168.5
150	857.9	572.0	429.0	343.2	286.0	245.1	214.5	190.7	171.6
152	873.7	582.4	436.8	349.5	291.2	249.6	218.4	194.1	174.7
154	889.5	593.0	444.7	355.8	296.5	254.1	222.4	197.7	177.9
156	905.4	603.6	452.7	362.1	301.8	258.7	226.3	201.2	181.1
158	921.3	614.2	460.7	368.5	307.1	263.2	230.3	204.7	184.3
160	937.4	624.9	468.7	374.9	312.5	267.8	234.3	208.3	187.5
162	953.5	635.7	476.7	381.4	317.8	272.4	238.4	211.9	190.7
164	969.7	646.4	484.8	387.9	323.2	277.0	242.4	215.5	193.9
166	985.9	657.3	493.0	394.4	328.6	281.7	246.5	219.1	197.2
168	1002.3	668.2	501.1	400.9	334.1	286.4	250.6	222.7	200.5
170	1018.7	679.1	509.3	407.5	339.6	291.0	254.7	226.4	203.7
172	1035.2	690.1	517.6	414.1	345.1	295.8	258.8	230.0	207.0
174	1051.7	701.1	525.9	420.7	350.6	300.5	262.9	233.7	210.3
176	1068.3	712.2	534.2	427.3	356.1	305.2	267.1	237.4	213.7
178	1085.0	723.3	542.5	434.0	361.7	310.0	271.3	241.1	217.0
180	1101.8	734.5	550.9	440.7	367.3	314.8	275.4	244.8	220.4

SNR = 10									
Body Mass	**Bed Duration (min)**								
(kg)	**1**	**1.5**	**2**	**2.5**	**3**	**3.5**	**4**	**4.5**	**5**
10	32.6	21.8	16.3	13.1	10.9	9.3	8.2	7.3	6.5
12	41.9	27.9	21.0	16.8	14.0	12.0	10.5	9.3	8.4
14	51.8	34.5	25.9	20.7	17.3	14.8	12.9	11.5	10.4
16	62.2	41.5	31.1	24.9	20.7	17.8	15.5	13.8	12.4
18	73.1	48.7	36.5	29.2	24.4	20.9	18.3	16.2	14.6
20	84.5	56.3	42.2	33.8	28.2	24.1	21.1	18.8	16.9
22	96.3	64.2	48.1	38.5	32.1	27.5	24.1	21.4	19.3
24	108.5	72.3	54.2	43.4	36.2	31.0	27.1	24.1	21.7
26	121.1	80.7	60.5	48.4	40.4	34.6	30.3	26.9	24.2
28	134.0	89.3	67.0	53.6	44.7	38.3	33.5	29.8	26.8
30	147.3	98.2	73.7	58.9	49.1	42.1	36.8	32.7	29.5
32	161.0	107.3	80.5	64.4	53.7	46.0	40.2	35.8	32.2
34	174.9	116.6	87.5	70.0	58.3	50.0	43.7	38.9	35.0
36	189.2	126.1	94.6	75.7	63.1	54.1	47.3	42.0	37.8
38	203.8	135.8	101.9	81.5	67.9	58.2	50.9	45.3	40.8
40	218.6	145.8	109.3	87.5	72.9	62.5	54.7	48.6	43.7
42	233.8	155.8	116.9	93.5	77.9	66.8	58.4	51.9	46.8
44	249.2	166.1	124.6	99.7	83.1	71.2	62.3	55.4	49.8
46	264.8	176.6	132.4	105.9	88.3	75.7	66.2	58.9	53.0
48	280.8	187.2	140.4	112.3	93.6	80.2	70.2	62.4	56.2
50	296.9	198.0	148.5	118.8	99.0	84.8	74.2	66.0	59.4
52	313.4	208.9	156.7	125.3	104.5	89.5	78.3	69.6	62.7
54	330.0	220.0	165.0	132.0	110.0	94.3	82.5	73.3	66.0
56	346.9	231.3	173.4	138.8	115.6	99.1	86.7	77.1	69.4
58	364.0	242.7	182.0	145.6	121.3	104.0	91.0	80.9	72.8
60	381.3	254.2	190.7	152.5	127.1	109.0	95.3	84.7	76.3
62	398.9	265.9	199.4	159.6	133.0	114.0	99.7	88.6	79.8
64	416.6	277.8	208.3	166.7	138.9	119.0	104.2	92.6	83.3
66	434.6	289.7	217.3	173.8	144.9	124.2	108.7	96.6	86.9
68	452.8	301.8	226.4	181.1	150.9	129.4	113.2	100.6	90.6
70	471.1	314.1	235.6	188.5	157.0	134.6	117.8	104.7	94.2
72	489.7	326.5	244.9	195.9	163.2	139.9	122.4	108.8	97.9
74	508.5	339.0	254.2	203.4	169.5	145.3	127.1	113.0	101.7
76	527.4	351.6	263.7	211.0	175.8	150.7	131.9	117.2	105.5
78	546.6	364.4	273.3	218.6	182.2	156.2	136.6	121.5	109.3
80	565.9	377.2	282.9	226.3	188.6	161.7	141.5	125.7	113.2
82	585.4	390.2	292.7	234.1	195.1	167.2	146.3	130.1	117.1
84	605.0	403.4	302.5	242.0	201.7	172.9	151.3	134.5	121.0
86	624.9	416.6	312.4	250.0	208.3	178.5	156.2	138.9	125.0
88	644.9	429.9	322.5	258.0	215.0	184.3	161.2	143.3	129.0
90	665.1	443.4	332.6	266.0	221.7	190.0	166.3	147.8	133.0
92	685.5	457.0	342.7	274.2	228.5	195.9	171.4	152.3	137.1
94	706.0	470.7	353.0	282.4	235.3	201.7	176.5	156.9	141.2
96	726.7	484.5	363.3	290.7	242.2	207.6	181.7	161.5	145.3
98	747.6	498.4	373.8	299.0	249.2	213.6	186.9	166.1	149.5
100	768.6	512.4	384.3	307.4	256.2	219.6	192.1	170.8	153.7
102	789.7	526.5	394.9	315.9	263.2	225.6	197.4	175.5	157.9
104	811.1	540.7	405.5	324.4	270.4	231.7	202.8	180.2	162.2
106	832.5	555.0	416.3	333.0	277.5	237.9	208.1	185.0	166.5
108	854.2	569.4	427.1	341.7	284.7	244.0	213.5	189.8	170.8
110	875.9	584.0	438.0	350.4	292.0	250.3	219.0	194.7	175.2
112	897.9	598.6	448.9	359.1	299.3	256.5	224.5	199.5	179.6
114	919.9	613.3	460.0	368.0	306.6	262.8	230.0	204.4	184.0
116	942.1	628.1	471.1	376.9	314.0	269.2	235.5	209.4	188.4
118	964.5	643.0	482.2	385.8	321.5	275.6	241.1	214.3	192.9
120	987.0	658.0	493.5	394.8	329.0	282.0	246.7	219.3	197.4
122	1009.6	673.1	504.8	403.9	336.5	288.5	252.4	224.4	201.9
124	1032.4	688.3	516.2	413.0	344.1	295.0	258.1	229.4	206.5
126	1055.3	703.6	527.7	422.1	351.8	301.5	263.8	234.5	211.1
128	1078.4	718.9	539.2	431.4	359.5	308.1	269.6	239.6	215.7
130	1101.6	734.4	550.8	440.6	367.2	314.7	275.4	244.8	220.3
132	1124.9	749.9	562.4	450.0	375.0	321.4	281.2	250.0	225.0
134	1148.3	765.6	574.2	459.3	382.8	328.1	287.1	255.2	229.7
136	1171.9	781.3	586.0	468.8	390.6	334.8	293.0	260.4	234.4
138	1195.6	797.1	597.8	478.2	398.5	341.6	298.9	265.7	239.1
140	1219.5	813.0	609.7	487.8	406.5	348.4	304.9	271.0	243.9
142	1243.4	828.9	621.7	497.4	414.5	355.3	310.9	276.3	248.7
144	1267.5	845.0	633.8	507.0	422.5	362.1	316.9	281.7	253.5
146	1291.7	861.2	645.9	516.7	430.6	369.1	322.9	287.1	258.3
148	1316.1	877.4	658.0	526.4	438.7	376.0	329.0	292.5	263.2
150	1340.5	893.7	670.3	536.2	446.8	383.0	335.1	297.9	268.1
152	1365.1	910.1	682.6	546.0	455.0	390.0	341.3	303.4	273.0
154	1389.8	926.5	694.9	555.9	463.3	397.1	347.5	308.8	278.0
156	1414.6	943.1	707.3	565.9	471.5	404.2	353.7	314.4	282.9
158	1439.6	959.7	719.8	575.8	479.9	411.3	359.9	319.9	287.9
160	1464.6	976.4	732.3	585.9	488.2	418.5	366.2	325.5	292.9
162	1489.8	993.2	744.9	595.9	496.6	425.7	372.5	331.1	298.0
164	1515.1	1010.1	757.6	606.0	505.0	432.9	378.8	336.7	303.0
166	1540.5	1027.0	770.3	616.2	513.5	440.1	385.1	342.3	308.1
168	1566.0	1044.0	783.0	626.4	522.0	447.4	391.5	348.0	313.2
170	1591.7	1061.1	795.8	636.7	530.6	454.8	397.9	353.7	318.3
172	1617.4	1078.3	808.7	647.0	539.1	462.1	404.4	359.4	323.5
174	1643.3	1095.5	821.6	657.3	547.8	469.5	410.8	365.2	328.7
176	1669.3	1112.8	834.6	667.7	556.4	476.9	417.3	370.9	333.9
178	1695.3	1130.2	847.7	678.1	565.1	484.4	423.8	376.7	339.1
180	1721.5	1147.7	860.8	688.6	573.8	491.9	430.4	382.6	344.3

SNR = 12									
Body Mass	**Bed Duration (min)**								
(kg)	**1**	**1.5**	**2**	**2.5**	**3**	**3.5**	**4**	**4.5**	**5**
10	47.0	31.3	23.5	18.8	15.7	13.4	11.7	10.4	9.4
12	60.4	40.2	30.2	24.1	20.1	17.2	15.1	13.4	12.1
14	74.6	49.7	37.3	29.8	24.9	21.3	18.6	16.6	14.9
16	89.6	59.7	44.8	35.8	29.9	25.6	22.4	19.9	17.9
18	105.3	70.2	52.6	42.1	35.1	30.1	26.3	23.4	21.1
20	121.6	81.1	60.8	48.7	40.5	34.8	30.4	27.0	24.3
22	138.6	92.4	69.3	55.5	46.2	39.6	34.7	30.8	27.7
24	156.2	104.1	78.1	62.5	52.1	44.6	39.1	34.7	31.2
26	174.3	116.2	87.2	69.7	58.1	49.8	43.6	38.7	34.9
28	193.0	128.7	96.5	77.2	64.3	55.1	48.2	42.9	38.6
30	212.2	141.4	106.1	84.9	70.7	60.6	53.0	47.1	42.4
32	231.8	154.5	115.9	92.7	77.3	66.2	57.9	51.5	46.4
34	251.9	167.9	126.0	100.8	84.0	72.0	63.0	56.0	50.4
36	272.5	181.6	136.2	109.0	90.8	77.8	68.1	60.5	54.5
38	293.4	195.6	146.7	117.4	97.8	83.8	73.4	65.2	58.7
40	314.8	209.9	157.4	125.9	104.9	89.9	78.7	70.0	63.0
42	336.6	224.4	168.3	134.6	112.2	96.2	84.2	74.8	67.3
44	358.8	239.2	179.4	143.5	119.6	102.5	89.7	79.7	71.8
46	381.4	254.2	190.7	152.5	127.1	109.0	95.3	84.7	76.3
48	404.3	269.5	202.2	161.7	134.8	115.5	101.1	89.8	80.9
50	427.6	285.1	213.8	171.0	142.5	122.2	106.9	95.0	85.5
52	451.2	300.8	225.6	180.5	150.4	128.9	112.8	100.3	90.2
54	475.2	316.8	237.6	190.1	158.4	135.8	118.8	105.6	95.0
56	499.5	333.0	249.8	199.8	166.5	142.7	124.9	111.0	99.9
58	524.2	349.4	262.1	209.7	174.7	149.8	131.0	116.5	104.8
60	549.1	366.1	274.6	219.6	183.0	156.9	137.3	122.0	109.8
62	574.4	382.9	287.2	229.8	191.5	164.1	143.6	127.6	114.9
64	600.0	400.0	300.0	240.0	200.0	171.4	150.0	133.3	120.0
66	625.8	417.2	312.9	250.3	208.6	178.8	156.5	139.1	125.2
68	652.0	434.7	326.0	260.8	217.3	186.3	163.0	144.9	130.4
70	678.4	452.3	339.2	271.4	226.1	193.8	169.6	150.8	135.7
72	705.2	470.1	352.6	282.1	235.1	201.5	176.3	156.7	141.0
74	732.2	488.1	366.1	292.9	244.1	209.2	183.0	162.7	146.4
76	759.5	506.3	379.7	303.8	253.2	217.0	189.9	168.8	151.9
78	787.0	524.7	393.5	314.8	262.3	224.9	196.8	174.9	157.4
80	814.9	543.2	407.4	325.9	271.6	232.8	203.7	181.1	163.0
82	842.9	562.0	421.5	337.2	281.0	240.8	210.7	187.3	168.6
84	871.3	580.8	435.6	348.5	290.4	248.9	217.8	193.6	174.3
86	899.9	599.9	449.9	359.9	300.0	257.1	225.0	200.0	180.0
88	928.7	619.1	464.3	371.5	309.6	265.3	232.2	206.4	185.7
90	957.8	638.5	478.9	383.1	319.3	273.6	239.4	212.8	191.6
92	987.1	658.1	493.5	394.8	329.0	282.0	246.8	219.4	197.4
94	1016.7	677.8	508.3	406.7	338.9	290.5	254.2	225.9	203.3
96	1046.4	697.6	523.2	418.6	348.8	299.0	261.6	232.5	209.3
98	1076.5	717.6	538.2	430.6	358.8	307.6	269.1	239.2	215.3
100	1106.7	737.8	553.4	442.7	368.9	316.2	276.7	245.9	221.3
102	1137.2	758.1	568.6	454.9	379.1	324.9	284.3	252.7	227.4
104	1167.9	778.6	584.0	467.2	389.3	333.7	292.0	259.5	233.6
106	1198.8	799.2	599.4	479.5	399.6	342.5	299.7	266.4	239.8
108	1230.0	820.0	615.0	492.0	410.0	351.4	307.5	273.3	246.0
110	1261.3	840.9	630.7	504.5	420.4	360.4	315.3	280.3	252.3
112	1292.9	861.9	646.5	517.2	431.0	369.4	323.2	287.3	258.6
114	1324.7	883.1	662.3	529.9	441.6	378.5	331.2	294.4	264.9
116	1356.7	904.5	678.3	542.7	452.2	387.6	339.2	301.5	271.3
118	1388.9	925.9	694.4	555.5	463.0	396.8	347.2	308.6	277.8
120	1421.3	947.5	710.6	568.5	473.8	406.1	355.3	315.8	284.3
122	1453.9	969.2	726.9	581.5	484.6	415.4	363.5	323.1	290.8
124	1486.7	991.1	743.3	594.7	495.6	424.8	371.7	330.4	297.3
126	1519.7	1013.1	759.8	607.9	506.6	434.2	379.9	337.7	303.9
128	1552.9	1035.2	776.4	621.1	517.6	443.7	388.2	345.1	310.6
130	1586.2	1057.5	793.1	634.5	528.7	453.2	396.6	352.5	317.2
132	1619.8	1079.9	809.9	647.9	539.9	462.8	405.0	360.0	324.0
134	1653.6	1102.4	826.8	661.4	551.2	472.5	413.4	367.5	330.7
136	1687.5	1125.0	843.8	675.0	562.5	482.2	421.9	375.0	337.5
138	1721.7	1147.8	860.8	688.7	573.9	491.9	430.4	382.6	344.3
140	1756.0	1170.7	878.0	702.4	585.3	501.7	439.0	390.2	351.2
142	1790.5	1193.7	895.3	716.2	596.8	511.6	447.6	397.9	358.1
144	1825.2	1216.8	912.6	730.1	608.4	521.5	456.3	405.6	365.0
146	1860.1	1240.1	930.0	744.0	620.0	531.5	465.0	413.4	372.0
148	1895.1	1263.4	947.6	758.1	631.7	541.5	473.8	421.1	379.0
150	1930.4	1286.9	965.2	772.1	643.5	551.5	482.6	429.0	386.1
152	1965.8	1310.5	982.9	786.3	655.3	561.6	491.4	436.8	393.2
154	2001.3	1334.2	1000.7	800.5	667.1	571.8	500.3	444.7	400.3
156	2037.1	1358.1	1018.5	814.8	679.0	582.0	509.3	452.7	407.4
158	2073.0	1382.0	1036.5	829.2	691.0	592.3	518.2	460.7	414.6
160	2109.1	1406.1	1054.5	843.6	703.0	602.6	527.3	468.7	421.8
162	2145.3	1430.2	1072.7	858.1	715.1	613.0	536.3	476.7	429.1
164	2181.8	1454.5	1090.9	872.7	727.3	623.4	545.4	484.8	436.4
166	2218.3	1478.9	1109.2	887.3	739.4	633.8	554.6	493.0	443.7
168	2255.1	1503.4	1127.5	902.0	751.7	644.3	563.8	501.1	451.0
170	2292.0	1528.0	1146.0	916.8	764.0	654.9	573.0	509.3	458.4
172	2329.1	1552.7	1164.5	931.6	776.4	665.5	582.3	517.6	465.8
174	2366.3	1577.6	1183.2	946.5	788.8	676.1	591.6	525.9	473.3
176	2403.7	1602.5	1201.9	961.5	801.2	686.8	600.9	534.2	480.7
178	2441.3	1627.5	1220.6	976.5	813.8	697.5	610.3	542.5	488.3
180	2479.0	1652.7	1239.5	991.6	826.3	708.3	619.7	550.9	495.8

SNR = 15									
Body Mass	**Bed Duration (min)**								
(kg)	**1**	**1.5**	**2**	**2.5**	**3**	**3.5**	**4**	**4.5**	**5**
10	73.4	49.0	36.7	29.4	24.5	21.0	18.4	16.3	14.7
12	94.3	62.9	47.1	37.7	31.4	26.9	23.6	21.0	18.9
14	116.5	77.7	58.3	46.6	38.8	33.3	29.1	25.9	23.3
16	139.9	93.3	70.0	56.0	46.6	40.0	35.0	31.1	28.0
18	164.5	109.6	82.2	65.8	54.8	47.0	41.1	36.5	32.9
20	190.1	126.7	95.0	76.0	63.4	54.3	47.5	42.2	38.0
22	216.6	144.4	108.3	86.6	72.2	61.9	54.2	48.1	43.3
24	244.1	162.7	122.0	97.6	81.4	69.7	61.0	54.2	48.8
26	272.4	181.6	136.2	109.0	90.8	77.8	68.1	60.5	54.5
28	301.6	201.0	150.8	120.6	100.5	86.2	75.4	67.0	60.3
30	331.5	221.0	165.7	132.6	110.5	94.7	82.9	73.7	66.3
32	362.2	241.5	181.1	144.9	120.7	103.5	90.5	80.5	72.4
34	393.6	262.4	196.8	157.4	131.2	112.5	98.4	87.5	78.7
36	425.7	283.8	212.9	170.3	141.9	121.6	106.4	94.6	85.1
38	458.5	305.7	229.2	183.4	152.8	131.0	114.6	101.9	91.7
40	491.9	327.9	246.0	196.8	164.0	140.5	123.0	109.3	98.4
42	526.0	350.6	263.0	210.4	175.3	150.3	131.5	116.9	105.2
44	560.6	373.8	280.3	224.3	186.9	160.2	140.2	124.6	112.1
46	595.9	397.3	297.9	238.4	198.6	170.3	149.0	132.4	119.2
48	631.7	421.1	315.9	252.7	210.6	180.5	157.9	140.4	126.3
50	668.1	445.4	334.1	267.2	222.7	190.9	167.0	148.5	133.6
52	705.0	470.0	352.5	282.0	235.0	201.4	176.3	156.7	141.0
54	742.5	495.0	371.3	297.0	247.5	212.1	185.6	165.0	148.5
56	780.5	520.3	390.3	312.2	260.2	223.0	195.1	173.4	156.1
58	819.0	546.0	409.5	327.6	273.0	234.0	204.8	182.0	163.8
60	858.0	572.0	429.0	343.2	286.0	245.1	214.5	190.7	171.6
62	897.5	598.3	448.7	359.0	299.2	256.4	224.4	199.4	179.5
64	937.4	625.0	468.7	375.0	312.5	267.8	234.4	208.3	187.5
66	977.9	651.9	488.9	391.1	326.0	279.4	244.5	217.3	195.6
68	1018.7	679.2	509.4	407.5	339.6	291.1	254.7	226.4	203.7
70	1060.1	706.7	530.0	424.0	353.4	302.9	265.0	235.6	212.0
72	1101.8	734.6	550.9	440.7	367.3	314.8	275.5	244.9	220.4
74	1144.1	762.7	572.0	457.6	381.4	326.9	286.0	254.2	228.8
76	1186.7	791.1	593.3	474.7	395.6	339.1	296.7	263.7	237.3
78	1229.7	819.8	614.9	491.9	409.9	351.4	307.4	273.3	245.9
80	1273.2	848.8	636.6	509.3	424.4	363.8	318.3	282.9	254.6
82	1317.1	878.1	658.5	526.8	439.0	376.3	329.3	292.7	263.4
84	1361.4	907.6	680.7	544.5	453.8	389.0	340.3	302.5	272.3
86	1406.0	937.3	703.0	562.4	468.7	401.7	351.5	312.4	281.2
88	1451.1	967.4	725.5	580.4	483.7	414.6	362.8	322.5	290.2
90	1496.5	997.7	748.3	598.6	498.8	427.6	374.1	332.6	299.3
92	1542.3	1028.2	771.2	616.9	514.1	440.7	385.6	342.7	308.5
94	1588.5	1059.0	794.3	635.4	529.5	453.9	397.1	353.0	317.7
96	1635.1	1090.0	817.5	654.0	545.0	467.2	408.8	363.3	327.0
98	1682.0	1121.3	841.0	672.8	560.7	480.6	420.5	373.8	336.4
100	1729.3	1152.8	864.6	691.7	576.4	494.1	432.3	384.3	345.9
102	1776.9	1184.6	888.4	710.8	592.3	507.7	444.2	394.9	355.4
104	1824.9	1216.6	912.4	729.9	608.3	521.4	456.2	405.5	365.0
106	1873.2	1248.8	936.6	749.3	624.4	535.2	468.3	416.3	374.6
108	1921.8	1281.2	960.9	768.7	640.6	549.1	480.5	427.1	384.4
110	1970.8	1313.9	985.4	788.3	656.9	563.1	492.7	438.0	394.2
112	2020.2	1346.8	1010.1	808.1	673.4	577.2	505.0	448.9	404.0
114	2069.8	1379.9	1034.9	827.9	689.9	591.4	517.5	460.0	414.0
116	2119.8	1413.2	1059.9	847.9	706.6	605.7	530.0	471.1	424.0
118	2170.1	1446.7	1085.1	868.0	723.4	620.0	542.5	482.2	434.0
120	2220.7	1480.5	1110.4	888.3	740.2	634.5	555.2	493.5	444.1
122	2271.7	1514.5	1135.8	908.7	757.2	649.1	567.9	504.8	454.3
124	2322.9	1548.6	1161.5	929.2	774.3	663.7	580.7	516.2	464.6
126	2374.5	1583.0	1187.2	949.8	791.5	678.4	593.6	527.7	474.9
128	2426.3	1617.6	1213.2	970.5	808.8	693.2	606.6	539.2	485.3
130	2478.5	1652.3	1239.3	991.4	826.2	708.1	619.6	550.8	495.7
132	2531.0	1687.3	1265.5	1012.4	843.7	723.1	632.7	562.4	506.2
134	2583.7	1722.5	1291.9	1033.5	861.2	738.2	645.9	574.2	516.7
136	2636.8	1757.9	1318.4	1054.7	878.9	753.4	659.2	586.0	527.4
138	2690.1	1793.4	1345.1	1076.1	896.7	768.6	672.5	597.8	538.0
140	2743.8	1829.2	1371.9	1097.5	914.6	783.9	685.9	609.7	548.8
142	2797.7	1865.1	1398.8	1119.1	932.6	799.3	699.4	621.7	559.5
144	2851.9	1901.3	1426.0	1140.8	950.6	814.8	713.0	633.8	570.4
146	2906.4	1937.6	1453.2	1162.6	968.8	830.4	726.6	645.9	581.3
148	2961.1	1974.1	1480.6	1184.5	987.0	846.0	740.3	658.0	592.2
150	3016.2	2010.8	1508.1	1206.5	1005.4	861.8	754.0	670.3	603.2
152	3071.5	2047.7	1535.7	1228.6	1023.8	877.6	767.9	682.6	614.3
154	3127.1	2084.7	1563.5	1250.8	1042.4	893.5	781.8	694.9	625.4
156	3182.9	2122.0	1591.5	1273.2	1061.0	909.4	795.7	707.3	636.6
158	3239.1	2159.4	1619.5	1295.6	1079.7	925.4	809.8	719.8	647.8
160	3295.4	2197.0	1647.7	1318.2	1098.5	941.6	823.9	732.3	659.1
162	3352.1	2234.7	1676.0	1340.8	1117.4	957.7	838.0	744.9	670.4
164	3409.0	2272.7	1704.5	1363.6	1136.3	974.0	852.2	757.6	681.8
166	3466.2	2310.8	1733.1	1386.5	1155.4	990.3	866.5	770.3	693.2
168	3523.6	2349.1	1761.8	1409.4	1174.5	1006.7	880.9	783.0	704.7
170	3581.3	2387.5	1790.6	1432.5	1193.8	1023.2	895.3	795.8	716.3
172	3639.2	2426.1	1819.6	1455.7	1213.1	1039.8	909.8	808.7	727.8
174	3697.4	2464.9	1848.7	1479.0	1232.5	1056.4	924.3	821.6	739.5
176	3755.8	2503.9	1877.9	1502.3	1251.9	1073.1	939.0	834.6	751.2
178	3814.5	2543.0	1907.2	1525.8	1271.5	1089.9	953.6	847.7	762.9
180	3873.4	2582.3	1936.7	1549.4	1291.1	1106.7	968.4	860.8	774.7

A.2 Injected Activity (MBq): Discovery MI - FXS 3i 8s 3.2mm FWHM

SNR = 5									
Body Mass (kg)	Bed Duration (min)								
	1	1.5	2	2.5	3	3.5	4	4.5	5
10	22.0	14.6	11.0	8.8	7.3	6.3	5.5	4.9	4.4
12	28.2	18.8	14.1	11.3	9.4	8.1	7.1	6.3	5.6
14	34.8	23.2	17.4	13.9	11.6	10.0	8.7	7.7	7.0
16	41.9	27.9	20.9	16.7	14.0	12.0	10.5	9.3	8.4
18	49.2	32.8	24.6	19.7	16.4	14.1	12.3	10.9	9.8
20	56.8	37.9	28.4	22.7	18.9	16.2	14.2	12.6	11.4
22	64.8	43.2	32.4	25.9	21.6	18.5	16.2	14.4	13.0
24	73.0	48.7	36.5	29.2	24.3	20.9	18.3	16.2	14.6
26	81.5	54.3	40.7	32.6	27.2	23.3	20.4	18.1	16.3
28	90.2	60.1	45.1	36.1	30.1	25.8	22.5	20.0	18.0
30	99.2	66.1	49.6	39.7	33.1	28.3	24.8	22.0	19.8
32	108.3	72.2	54.2	43.3	36.1	31.0	27.1	24.1	21.7
34	117.7	78.5	58.9	47.1	39.2	33.6	29.4	26.2	23.5
36	127.3	84.9	63.7	50.9	42.4	36.4	31.8	28.3	25.5
38	137.1	91.4	68.6	54.9	45.7	39.2	34.3	30.5	27.4
40	147.1	98.1	73.6	58.9	49.0	42.0	36.8	32.7	29.4
42	157.3	104.9	78.7	62.9	52.4	44.9	39.3	35.0	31.5
44	167.7	111.8	83.8	67.1	55.9	47.9	41.9	37.3	33.5
46	178.2	118.8	89.1	71.3	59.4	50.9	44.6	39.6	35.6
48	189.0	126.0	94.5	75.6	63.0	54.0	47.2	42.0	37.8
50	199.8	133.2	99.9	79.9	66.6	57.1	50.0	44.4	40.0
52	210.9	140.6	105.4	84.4	70.3	60.3	52.7	46.9	42.2
54	222.1	148.1	111.0	88.8	74.0	63.5	55.5	49.4	44.4
56	233.5	155.6	116.7	93.4	77.8	66.7	58.4	51.9	46.7
58	245.0	163.3	122.5	98.0	81.7	70.0	61.2	54.4	49.0
60	256.6	171.1	128.3	102.7	85.5	73.3	64.2	57.0	51.3
62	268.4	179.0	134.2	107.4	89.5	76.7	67.1	59.7	53.7
64	280.4	186.9	140.2	112.2	93.5	80.1	70.1	62.3	56.1
66	292.5	195.0	146.2	117.0	97.5	83.6	73.1	65.0	58.5
68	304.7	203.1	152.4	121.9	101.6	87.1	76.2	67.7	60.9
70	317.1	211.4	158.5	126.8	105.7	90.6	79.3	70.5	63.4
72	329.6	219.7	164.8	131.8	109.9	94.2	82.4	73.2	65.9
74	342.2	228.1	171.1	136.9	114.1	97.8	85.5	76.0	68.4
76	355.0	236.6	177.5	142.0	118.3	101.4	88.7	78.9	71.0
78	367.8	245.2	183.9	147.1	122.6	105.1	92.0	81.7	73.6
80	380.8	253.9	190.4	152.3	126.9	108.8	95.2	84.6	76.2
82	394.0	262.6	197.0	157.6	131.3	112.6	98.5	87.5	78.8
84	407.2	271.5	203.6	162.9	135.7	116.3	101.8	90.5	81.4
86	420.6	280.4	210.3	168.2	140.2	120.2	105.1	93.5	84.1
88	434.0	289.4	217.0	173.6	144.7	124.0	108.5	96.5	86.8
90	447.6	298.4	223.8	179.0	149.2	127.9	111.9	99.5	89.5
92	461.3	307.6	230.7	184.5	153.8	131.8	115.3	102.5	92.3
94	475.1	316.8	237.6	190.1	158.4	135.8	118.8	105.6	95.0
96	489.1	326.0	244.5	195.6	163.0	139.7	122.3	108.7	97.8
98	503.1	335.4	251.6	201.2	167.7	143.7	125.8	111.8	100.6
100	517.2	344.8	258.6	206.9	172.4	147.8	129.3	114.9	103.4
102	531.5	354.3	265.7	212.6	177.2	151.9	132.9	118.1	106.3
104	545.8	363.9	272.9	218.3	181.9	156.0	136.5	121.3	109.2
106	560.3	373.5	280.1	224.1	186.8	160.1	140.1	124.5	112.1
108	574.8	383.2	287.4	229.9	191.6	164.2	143.7	127.7	115.0
110	589.5	393.0	294.8	235.8	196.5	168.4	147.4	131.0	117.9
112	604.3	402.8	302.1	241.7	201.4	172.6	151.1	134.3	120.9
114	619.1	412.7	309.6	247.6	206.4	176.9	154.8	137.6	123.8
116	634.1	422.7	317.0	253.6	211.4	181.2	158.5	140.9	126.8
118	649.1	432.7	324.6	259.6	216.4	185.5	162.3	144.2	129.8
120	664.2	442.8	332.1	265.7	221.4	189.8	166.1	147.6	132.8
122	679.5	453.0	339.7	271.8	226.5	194.1	169.9	151.0	135.9
124	694.8	463.2	347.4	277.9	231.6	198.5	173.7	154.4	139.0
126	710.2	473.5	355.1	284.1	236.7	202.9	177.6	157.8	142.0
128	725.7	483.8	362.9	290.3	241.9	207.4	181.4	161.3	145.1
130	741.4	494.2	370.7	296.5	247.1	211.8	185.3	164.7	148.3
132	757.0	504.7	378.5	302.8	252.3	216.3	189.3	168.2	151.4
134	772.8	515.2	386.4	309.1	257.6	220.8	193.2	171.7	154.6
136	788.7	525.8	394.3	315.5	262.9	225.3	197.2	175.3	157.7
138	804.7	536.4	402.3	321.9	268.2	229.9	201.2	178.8	160.9
140	820.7	547.1	410.3	328.3	273.6	234.5	205.2	182.4	164.1
142	836.8	557.9	418.4	334.7	278.9	239.1	209.2	186.0	167.4
144	853.0	568.7	426.5	341.2	284.3	243.7	213.3	189.6	170.6
146	869.3	579.6	434.7	347.7	289.8	248.4	217.3	193.2	173.9
148	885.7	590.5	442.9	354.3	295.2	253.1	221.4	196.8	177.1
150	902.2	601.4	451.1	360.9	300.7	257.8	225.5	200.5	180.4
152	918.7	612.5	459.4	367.5	306.2	262.5	229.7	204.2	183.7
154	935.3	623.6	467.7	374.1	311.8	267.2	233.8	207.9	187.1
156	952.1	634.7	476.0	380.8	317.4	272.0	238.0	211.6	190.4
158	968.8	645.9	484.4	387.5	322.9	276.8	242.2	215.3	193.8
160	985.7	657.1	492.9	394.3	328.6	281.6	246.4	219.0	197.1
162	1002.6	668.4	501.3	401.1	334.2	286.5	250.7	222.8	200.5
164	1019.7	679.8	509.8	407.9	339.9	291.3	254.9	226.6	203.9
166	1036.8	691.2	518.4	414.7	345.6	296.2	259.2	230.4	207.4
168	1053.9	702.6	527.0	421.6	351.3	301.1	263.5	234.2	210.8
170	1071.2	714.1	535.6	428.5	357.1	306.1	267.8	238.0	214.2
172	1088.5	725.7	544.3	435.4	362.8	311.0	272.1	241.9	217.7
174	1105.9	737.3	553.0	442.4	368.6	316.0	276.5	245.8	221.2
176	1123.4	748.9	561.7	449.4	374.5	321.0	280.9	249.6	224.7
178	1141.0	760.6	570.5	456.4	380.3	326.0	285.2	253.5	228.2
180	1158.6	772.4	579.3	463.4	386.2	331.0	289.6	257.5	231.7

SNR = 8									
Body Mass	**Bed Duration (min)**								
(kg)	**1**	**1.5**	**2**	**2.5**	**3**	**3.5**	**4**	**4.5**	**5**
10	14.1	9.4	7.0	5.6	4.7	4.0	3.5	3.1	2.8
12	18.1	12.0	9.0	7.2	6.0	5.2	4.5	4.0	3.6
14	22.3	14.9	11.2	8.9	7.4	6.4	5.6	5.0	4.5
16	26.8	17.9	13.4	10.7	8.9	7.7	6.7	6.0	5.4
18	31.5	21.0	15.7	12.6	10.5	9.0	7.9	7.0	6.3
20	36.4	24.3	18.2	14.6	12.1	10.4	9.1	8.1	7.3
22	41.5	27.6	20.7	16.6	13.8	11.8	10.4	9.2	8.3
24	46.7	31.1	23.4	18.7	15.6	13.3	11.7	10.4	9.3
26	52.1	34.8	26.1	20.9	17.4	14.9	13.0	11.6	10.4
28	57.7	38.5	28.9	23.1	19.2	16.5	14.4	12.8	11.5
30	63.5	42.3	31.7	25.4	21.2	18.1	15.9	14.1	12.7
32	69.3	46.2	34.7	27.7	23.1	19.8	17.3	15.4	13.9
34	75.3	50.2	37.7	30.1	25.1	21.5	18.8	16.7	15.1
36	81.5	54.3	40.7	32.6	27.2	23.3	20.4	18.1	16.3
38	87.8	58.5	43.9	35.1	29.3	25.1	21.9	19.5	17.6
40	94.2	62.8	47.1	37.7	31.4	26.9	23.5	20.9	18.8
42	100.7	67.1	50.3	40.3	33.6	28.8	25.2	22.4	20.1
44	107.3	71.5	53.7	42.9	35.8	30.7	26.8	23.8	21.5
46	114.1	76.0	57.0	45.6	38.0	32.6	28.5	25.3	22.8
48	120.9	80.6	60.5	48.4	40.3	34.6	30.2	26.9	24.2
50	127.9	85.3	63.9	51.2	42.6	36.5	32.0	28.4	25.6
52	135.0	90.0	67.5	54.0	45.0	38.6	33.7	30.0	27.0
54	142.1	94.8	71.1	56.9	47.4	40.6	35.5	31.6	28.4
56	149.4	99.6	74.7	59.8	49.8	42.7	37.4	33.2	29.9
58	156.8	104.5	78.4	62.7	52.3	44.8	39.2	34.8	31.4
60	164.2	109.5	82.1	65.7	54.7	46.9	41.1	36.5	32.8
62	171.8	114.5	85.9	68.7	57.3	49.1	43.0	38.2	34.4
64	179.5	119.6	89.7	71.8	59.8	51.3	44.9	39.9	35.9
66	187.2	124.8	93.6	74.9	62.4	53.5	46.8	41.6	37.4
68	195.0	130.0	97.5	78.0	65.0	55.7	48.8	43.3	39.0
70	202.9	135.3	101.5	81.2	67.6	58.0	50.7	45.1	40.6
72	210.9	140.6	105.5	84.4	70.3	60.3	52.7	46.9	42.2
74	219.0	146.0	109.5	87.6	73.0	62.6	54.8	48.7	43.8
76	227.2	151.4	113.6	90.9	75.7	64.9	56.8	50.5	45.4
78	235.4	156.9	117.7	94.2	78.5	67.3	58.9	52.3	47.1
80	243.7	162.5	121.9	97.5	81.2	69.6	60.9	54.2	48.7
82	252.1	168.1	126.1	100.9	84.0	72.0	63.0	56.0	50.4
84	260.6	173.7	130.3	104.2	86.9	74.5	65.2	57.9	52.1
86	269.2	179.4	134.6	107.7	89.7	76.9	67.3	59.8	53.8
88	277.8	185.2	138.9	111.1	92.6	79.4	69.4	61.7	55.6
90	286.5	191.0	143.2	114.6	95.5	81.9	71.6	63.7	57.3
92	295.3	196.8	147.6	118.1	98.4	84.4	73.8	65.6	59.1
94	304.1	202.7	152.0	121.6	101.4	86.9	76.0	67.6	60.8
96	313.0	208.7	156.5	125.2	104.3	89.4	78.3	69.6	62.6
98	322.0	214.7	161.0	128.8	107.3	92.0	80.5	71.6	64.4
100	331.0	220.7	165.5	132.4	110.3	94.6	82.8	73.6	66.2
102	340.2	226.8	170.1	136.1	113.4	97.2	85.0	75.6	68.0
104	349.3	232.9	174.7	139.7	116.4	99.8	87.3	77.6	69.9
106	358.6	239.1	179.3	143.4	119.5	102.5	89.6	79.7	71.7
108	367.9	245.3	184.0	147.2	122.6	105.1	92.0	81.8	73.6
110	377.3	251.5	188.6	150.9	125.8	107.8	94.3	83.8	75.5
112	386.7	257.8	193.4	154.7	128.9	110.5	96.7	85.9	77.3
114	396.2	264.2	198.1	158.5	132.1	113.2	99.1	88.1	79.2
116	405.8	270.5	202.9	162.3	135.3	115.9	101.4	90.2	81.2
118	415.4	277.0	207.7	166.2	138.5	118.7	103.9	92.3	83.1
120	425.1	283.4	212.6	170.0	141.7	121.5	106.3	94.5	85.0
122	434.9	289.9	217.4	173.9	145.0	124.2	108.7	96.6	87.0
124	444.7	296.5	222.3	177.9	148.2	127.1	111.2	98.8	88.9
126	454.6	303.0	227.3	181.8	151.5	129.9	113.6	101.0	90.9
128	464.5	309.7	232.2	185.8	154.8	132.7	116.1	103.2	92.9
130	474.5	316.3	237.2	189.8	158.2	135.6	118.6	105.4	94.9
132	484.5	323.0	242.3	193.8	161.5	138.4	121.1	107.7	96.9
134	494.6	329.7	247.3	197.8	164.9	141.3	123.7	109.9	98.9
136	504.8	336.5	252.4	201.9	168.3	144.2	126.2	112.2	101.0
138	515.0	343.3	257.5	206.0	171.7	147.1	128.7	114.4	103.0
140	525.2	350.2	262.6	210.1	175.1	150.1	131.3	116.7	105.0
142	535.6	357.0	267.8	214.2	178.5	153.0	133.9	119.0	107.1
144	545.9	364.0	273.0	218.4	182.0	156.0	136.5	121.3	109.2
146	556.4	370.9	278.2	222.5	185.5	159.0	139.1	123.6	111.3
148	566.9	377.9	283.4	226.7	189.0	162.0	141.7	126.0	113.4
150	577.4	384.9	288.7	231.0	192.5	165.0	144.3	128.3	115.5
152	588.0	392.0	294.0	235.2	196.0	168.0	147.0	130.7	117.6
154	598.6	399.1	299.3	239.4	199.5	171.0	149.7	133.0	119.7
156	609.3	406.2	304.7	243.7	203.1	174.1	152.3	135.4	121.9
158	620.1	413.4	310.0	248.0	206.7	177.2	155.0	137.8	124.0
160	630.9	420.6	315.4	252.3	210.3	180.2	157.7	140.2	126.2
162	641.7	427.8	320.8	256.7	213.9	183.3	160.4	142.6	128.3
164	652.6	435.1	326.3	261.0	217.5	186.5	163.1	145.0	130.5
166	663.5	442.4	331.8	265.4	221.2	189.6	165.9	147.5	132.7
168	674.5	449.7	337.3	269.8	224.8	192.7	168.6	149.9	134.9
170	685.6	457.0	342.8	274.2	228.5	195.9	171.4	152.3	137.1
172	696.7	464.4	348.3	278.7	232.2	199.0	174.2	154.8	139.3
174	707.8	471.9	353.9	283.1	235.9	202.2	176.9	157.3	141.6
176	719.0	479.3	359.5	287.6	239.7	205.4	179.7	159.8	143.8
178	730.2	486.8	365.1	292.1	243.4	208.6	182.6	162.3	146.0
180	741.5	494.3	370.7	296.6	247.2	211.9	185.4	164.8	148.3

SNR = 10									
Body Mass	**Bed Duration (min)**								
(kg)	**1**	**1.5**	**2**	**2.5**	**3**	**3.5**	**4**	**4.5**	**5**
10	22.0	14.6	11.0	8.8	7.3	6.3	5.5	4.9	4.4
12	28.2	18.8	14.1	11.3	9.4	8.1	7.1	6.3	5.6
14	34.8	23.2	17.4	13.9	11.6	10.0	8.7	7.7	7.0
16	41.9	27.9	20.9	16.7	14.0	12.0	10.5	9.3	8.4
18	49.2	32.8	24.6	19.7	16.4	14.1	12.3	10.9	9.8
20	56.8	37.9	28.4	22.7	18.9	16.2	14.2	12.6	11.4
22	64.8	43.2	32.4	25.9	21.6	18.5	16.2	14.4	13.0
24	73.0	48.7	36.5	29.2	24.3	20.9	18.3	16.2	14.6
26	81.5	54.3	40.7	32.6	27.2	23.3	20.4	18.1	16.3
28	90.2	60.1	45.1	36.1	30.1	25.8	22.5	20.0	18.0
30	99.2	66.1	49.6	39.7	33.1	28.3	24.8	22.0	19.8
32	108.3	72.2	54.2	43.3	36.1	31.0	27.1	24.1	21.7
34	117.7	78.5	58.9	47.1	39.2	33.6	29.4	26.2	23.5
36	127.3	84.9	63.7	50.9	42.4	36.4	31.8	28.3	25.5
38	137.1	91.4	68.6	54.9	45.7	39.2	34.3	30.5	27.4
40	147.1	98.1	73.6	58.9	49.0	42.0	36.8	32.7	29.4
42	157.3	104.9	78.7	62.9	52.4	44.9	39.3	35.0	31.5
44	167.7	111.8	83.8	67.1	55.9	47.9	41.9	37.3	33.5
46	178.2	118.8	89.1	71.3	59.4	50.9	44.6	39.6	35.6
48	189.0	126.0	94.5	75.6	63.0	54.0	47.2	42.0	37.8
50	199.8	133.2	99.9	79.9	66.6	57.1	50.0	44.4	40.0
52	210.9	140.6	105.4	84.4	70.3	60.3	52.7	46.9	42.2
54	222.1	148.1	111.0	88.8	74.0	63.5	55.5	49.4	44.4
56	233.5	155.6	116.7	93.4	77.8	66.7	58.4	51.9	46.7
58	245.0	163.3	122.5	98.0	81.7	70.0	61.2	54.4	49.0
60	256.6	171.1	128.3	102.7	85.5	73.3	64.2	57.0	51.3
62	268.4	179.0	134.2	107.4	89.5	76.7	67.1	59.7	53.7
64	280.4	186.9	140.2	112.2	93.5	80.1	70.1	62.3	56.1
66	292.5	195.0	146.2	117.0	97.5	83.6	73.1	65.0	58.5
68	304.7	203.1	152.4	121.9	101.6	87.1	76.2	67.7	60.9
70	317.1	211.4	158.5	126.8	105.7	90.6	79.3	70.5	63.4
72	329.6	219.7	164.8	131.8	109.9	94.2	82.4	73.2	65.9
74	342.2	228.1	171.1	136.9	114.1	97.8	85.5	76.0	68.4
76	355.0	236.6	177.5	142.0	118.3	101.4	88.7	78.9	71.0
78	367.8	245.2	183.9	147.1	122.6	105.1	92.0	81.7	73.6
80	380.8	253.9	190.4	152.3	126.9	108.8	95.2	84.6	76.2
82	394.0	262.6	197.0	157.6	131.3	112.6	98.5	87.5	78.8
84	407.2	271.5	203.6	162.9	135.7	116.3	101.8	90.5	81.4
86	420.6	280.4	210.3	168.2	140.2	120.2	105.1	93.5	84.1
88	434.0	289.4	217.0	173.6	144.7	124.0	108.5	96.5	86.8
90	447.6	298.4	223.8	179.0	149.2	127.9	111.9	99.5	89.5
92	461.3	307.6	230.7	184.5	153.8	131.8	115.3	102.5	92.3
94	475.1	316.8	237.6	190.1	158.4	135.8	118.8	105.6	95.0
96	489.1	326.0	244.5	195.6	163.0	139.7	122.3	108.7	97.8
98	503.1	335.4	251.6	201.2	167.7	143.7	125.8	111.8	100.6
100	517.2	344.8	258.6	206.9	172.4	147.8	129.3	114.9	103.4
102	531.5	354.3	265.7	212.6	177.2	151.9	132.9	118.1	106.3
104	545.8	363.9	272.9	218.3	181.9	156.0	136.5	121.3	109.2
106	560.3	373.5	280.1	224.1	186.8	160.1	140.1	124.5	112.1
108	574.8	383.2	287.4	229.9	191.6	164.2	143.7	127.7	115.0
110	589.5	393.0	294.8	235.8	196.5	168.4	147.4	131.0	117.9
112	604.3	402.8	302.1	241.7	201.4	172.6	151.1	134.3	120.9
114	619.1	412.7	309.6	247.6	206.4	176.9	154.8	137.6	123.8
116	634.1	422.7	317.0	253.6	211.4	181.2	158.5	140.9	126.8
118	649.1	432.7	324.6	259.6	216.4	185.5	162.3	144.2	129.8
120	664.2	442.8	332.1	265.7	221.4	189.8	166.1	147.6	132.8
122	679.5	453.0	339.7	271.8	226.5	194.1	169.9	151.0	135.9
124	694.8	463.2	347.4	277.9	231.6	198.5	173.7	154.4	139.0
126	710.2	473.5	355.1	284.1	236.7	202.9	177.6	157.8	142.0
128	725.7	483.8	362.9	290.3	241.9	207.4	181.4	161.3	145.1
130	741.4	494.2	370.7	296.5	247.1	211.8	185.3	164.7	148.3
132	757.0	504.7	378.5	302.8	252.3	216.3	189.3	168.2	151.4
134	772.8	515.2	386.4	309.1	257.6	220.8	193.2	171.7	154.6
136	788.7	525.8	394.3	315.5	262.9	225.3	197.2	175.3	157.7
138	804.7	536.4	402.3	321.9	268.2	229.9	201.2	178.8	160.9
140	820.7	547.1	410.3	328.3	273.6	234.5	205.2	182.4	164.1
142	836.8	557.9	418.4	334.7	278.9	239.1	209.2	186.0	167.4
144	853.0	568.7	426.5	341.2	284.3	243.7	213.3	189.6	170.6
146	869.3	579.6	434.7	347.7	289.8	248.4	217.3	193.2	173.9
148	885.7	590.5	442.9	354.3	295.2	253.1	221.4	196.8	177.1
150	902.2	601.4	451.1	360.9	300.7	257.8	225.5	200.5	180.4
152	918.7	612.5	459.4	367.5	306.2	262.5	229.7	204.2	183.7
154	935.3	623.6	467.7	374.1	311.8	267.2	233.8	207.9	187.1
156	952.1	634.7	476.0	380.8	317.4	272.0	238.0	211.6	190.4
158	968.8	645.9	484.4	387.5	322.9	276.8	242.2	215.3	193.8
160	985.7	657.1	492.9	394.3	328.6	281.6	246.4	219.0	197.1
162	1002.6	668.4	501.3	401.1	334.2	286.5	250.7	222.8	200.5
164	1019.7	679.8	509.8	407.9	339.9	291.3	254.9	226.6	203.9
166	1036.8	691.2	518.4	414.7	345.6	296.2	259.2	230.4	207.4
168	1053.9	702.6	527.0	421.6	351.3	301.1	263.5	234.2	210.8
170	1071.2	714.1	535.6	428.5	357.1	306.1	267.8	238.0	214.2
172	1088.5	725.7	544.3	435.4	362.8	311.0	272.1	241.9	217.7
174	1105.9	737.3	553.0	442.4	368.6	316.0	276.5	245.8	221.2
176	1123.4	748.9	561.7	449.4	374.5	321.0	280.9	249.6	224.7
178	1141.0	760.6	570.5	456.4	380.3	326.0	285.2	253.5	228.2
180	1158.6	772.4	579.3	463.4	386.2	331.0	289.6	257.5	231.7

SNR = 12									
Body Mass	**Bed Duration (min)**								
(kg)	**1**	**1.5**	**2**	**2.5**	**3**	**3.5**	**4**	**4.5**	**5**
10	31.6	21.1	15.8	12.7	10.5	9.0	7.9	7.0	6.3
12	40.6	27.1	20.3	16.2	13.5	11.6	10.2	9.0	8.1
14	50.2	33.5	25.1	20.1	16.7	14.3	12.5	11.2	10.0
16	60.3	40.2	30.1	24.1	20.1	17.2	15.1	13.4	12.1
18	70.8	47.2	35.4	28.3	23.6	20.2	17.7	15.7	14.2
20	81.9	54.6	40.9	32.7	27.3	23.4	20.5	18.2	16.4
22	93.3	62.2	46.6	37.3	31.1	26.7	23.3	20.7	18.7
24	105.1	70.1	52.6	42.0	35.0	30.0	26.3	23.4	21.0
26	117.3	78.2	58.7	46.9	39.1	33.5	29.3	26.1	23.5
28	129.9	86.6	64.9	52.0	43.3	37.1	32.5	28.9	26.0
30	142.8	95.2	71.4	57.1	47.6	40.8	35.7	31.7	28.6
32	156.0	104.0	78.0	62.4	52.0	44.6	39.0	34.7	31.2
34	169.5	113.0	84.8	67.8	56.5	48.4	42.4	37.7	33.9
36	183.4	122.2	91.7	73.3	61.1	52.4	45.8	40.7	36.7
38	197.5	131.7	98.7	79.0	65.8	56.4	49.4	43.9	39.5
40	211.9	141.3	105.9	84.8	70.6	60.5	53.0	47.1	42.4
42	226.5	151.0	113.3	90.6	75.5	64.7	56.6	50.3	45.3
44	241.5	161.0	120.7	96.6	80.5	69.0	60.4	53.7	48.3
46	256.7	171.1	128.3	102.7	85.6	73.3	64.2	57.0	51.3
48	272.1	181.4	136.0	108.8	90.7	77.7	68.0	60.5	54.4
50	287.8	191.8	143.9	115.1	95.9	82.2	71.9	63.9	57.6
52	303.7	202.5	151.8	121.5	101.2	86.8	75.9	67.5	60.7
54	319.8	213.2	159.9	127.9	106.6	91.4	80.0	71.1	64.0
56	336.2	224.1	168.1	134.5	112.1	96.1	84.0	74.7	67.2
58	352.8	235.2	176.4	141.1	117.6	100.8	88.2	78.4	70.6
60	369.6	246.4	184.8	147.8	123.2	105.6	92.4	82.1	73.9
62	386.6	257.7	193.3	154.6	128.9	110.4	96.6	85.9	77.3
64	403.8	269.2	201.9	161.5	134.6	115.4	100.9	89.7	80.8
66	421.2	280.8	210.6	168.5	140.4	120.3	105.3	93.6	84.2
68	438.8	292.5	219.4	175.5	146.3	125.4	109.7	97.5	87.8
70	456.6	304.4	228.3	182.6	152.2	130.5	114.1	101.5	91.3
72	474.6	316.4	237.3	189.8	158.2	135.6	118.6	105.5	94.9
74	492.8	328.5	246.4	197.1	164.3	140.8	123.2	109.5	98.6
76	511.1	340.8	255.6	204.5	170.4	146.0	127.8	113.6	102.2
78	529.7	353.1	264.8	211.9	176.6	151.3	132.4	117.7	105.9
80	548.4	365.6	274.2	219.4	182.8	156.7	137.1	121.9	109.7
82	567.3	378.2	283.6	226.9	189.1	162.1	141.8	126.1	113.5
84	586.4	390.9	293.2	234.5	195.5	167.5	146.6	130.3	117.3
86	605.6	403.7	302.8	242.2	201.9	173.0	151.4	134.6	121.1
88	625.0	416.7	312.5	250.0	208.3	178.6	156.3	138.9	125.0
90	644.6	429.7	322.3	257.8	214.9	184.2	161.1	143.2	128.9
92	664.3	442.9	332.2	265.7	221.4	189.8	166.1	147.6	132.9
94	684.2	456.1	342.1	273.7	228.1	195.5	171.1	152.0	136.8
96	704.3	469.5	352.1	281.7	234.8	201.2	176.1	156.5	140.9
98	724.5	483.0	362.2	289.8	241.5	207.0	181.1	161.0	144.9
100	744.8	496.6	372.4	297.9	248.3	212.8	186.2	165.5	149.0
102	765.3	510.2	382.7	306.1	255.1	218.7	191.3	170.1	153.1
104	786.0	524.0	393.0	314.4	262.0	224.6	196.5	174.7	157.2
106	806.8	537.9	403.4	322.7	268.9	230.5	201.7	179.3	161.4
108	827.8	551.9	413.9	331.1	275.9	236.5	206.9	184.0	165.6
110	848.9	565.9	424.4	339.6	283.0	242.5	212.2	188.6	169.8
112	870.1	580.1	435.1	348.1	290.0	248.6	217.5	193.4	174.0
114	891.5	594.3	445.8	356.6	297.2	254.7	222.9	198.1	178.3
116	913.0	608.7	456.5	365.2	304.3	260.9	228.3	202.9	182.6
118	934.7	623.1	467.4	373.9	311.6	267.1	233.7	207.7	186.9
120	956.5	637.7	478.3	382.6	318.8	273.3	239.1	212.6	191.3
122	978.5	652.3	489.2	391.4	326.2	279.6	244.6	217.4	195.7
124	1000.5	667.0	500.3	400.2	333.5	285.9	250.1	222.3	200.1
126	1022.7	681.8	511.4	409.1	340.9	292.2	255.7	227.3	204.5
128	1045.1	696.7	522.5	418.0	348.4	298.6	261.3	232.2	209.0
130	1067.5	711.7	533.8	427.0	355.8	305.0	266.9	237.2	213.5
132	1090.1	726.8	545.1	436.1	363.4	311.5	272.5	242.3	218.0
134	1112.9	741.9	556.4	445.1	371.0	318.0	278.2	247.3	222.6
136	1135.7	757.1	567.9	454.3	378.6	324.5	283.9	252.4	227.1
138	1158.7	772.5	579.3	463.5	386.2	331.1	289.7	257.5	231.7
140	1181.8	787.9	590.9	472.7	393.9	337.7	295.4	262.6	236.4
142	1205.0	803.3	602.5	482.0	401.7	344.3	301.3	267.8	241.0
144	1228.4	818.9	614.2	491.3	409.5	351.0	307.1	273.0	245.7
146	1251.8	834.6	625.9	500.7	417.3	357.7	313.0	278.2	250.4
148	1275.4	850.3	637.7	510.2	425.1	364.4	318.9	283.4	255.1
150	1299.1	866.1	649.6	519.7	433.0	371.2	324.8	288.7	259.8
152	1323.0	882.0	661.5	529.2	441.0	378.0	330.7	294.0	264.6
154	1346.9	897.9	673.4	538.8	449.0	384.8	336.7	299.3	269.4
156	1371.0	914.0	685.5	548.4	457.0	391.7	342.7	304.7	274.2
158	1395.1	930.1	697.6	558.1	465.0	398.6	348.8	310.0	279.0
160	1419.4	946.3	709.7	567.8	473.1	405.5	354.9	315.4	283.9
162	1443.8	962.5	721.9	577.5	481.3	412.5	361.0	320.8	288.8
164	1468.3	978.9	734.2	587.3	489.4	419.5	367.1	326.3	293.7
166	1492.9	995.3	746.5	597.2	497.6	426.6	373.2	331.8	298.6
168	1517.7	1011.8	758.8	607.1	505.9	433.6	379.4	337.3	303.5
170	1542.5	1028.3	771.3	617.0	514.2	440.7	385.6	342.8	308.5
172	1567.5	1045.0	783.7	627.0	522.5	447.9	391.9	348.3	313.5
174	1592.5	1061.7	796.3	637.0	530.8	455.0	398.1	353.9	318.5
176	1617.7	1078.5	808.9	647.1	539.2	462.2	404.4	359.5	323.5
178	1643.0	1095.3	821.5	657.2	547.7	469.4	410.7	365.1	328.6
180	1668.4	1112.2	834.2	667.3	556.1	476.7	417.1	370.7	333.7

SNR = 15									
Body Mass	**Bed Duration (min)**								
(kg)	**1**	**1.5**	**2**	**2.5**	**3**	**3.5**	**4**	**4.5**	**5**
10	49.4	32.9	24.7	19.8	16.5	14.1	12.4	11.0	9.9
12	63.5	42.3	31.7	25.4	21.2	18.1	15.9	14.1	12.7
14	78.4	52.3	39.2	31.4	26.1	22.4	19.6	17.4	15.7
16	94.2	62.8	47.1	37.7	31.4	26.9	23.5	20.9	18.8
18	110.7	73.8	55.3	44.3	36.9	31.6	27.7	24.6	22.1
20	127.9	85.3	64.0	51.2	42.6	36.5	32.0	28.4	25.6
22	145.8	97.2	72.9	58.3	48.6	41.6	36.4	32.4	29.2
24	164.3	109.5	82.1	65.7	54.8	46.9	41.1	36.5	32.9
26	183.3	122.2	91.7	73.3	61.1	52.4	45.8	40.7	36.7
28	202.9	135.3	101.5	81.2	67.6	58.0	50.7	45.1	40.6
30	223.1	148.7	111.5	89.2	74.4	63.7	55.8	49.6	44.6
32	243.7	162.5	121.9	97.5	81.2	69.6	60.9	54.2	48.7
34	264.9	176.6	132.4	106.0	88.3	75.7	66.2	58.9	53.0
36	286.5	191.0	143.2	114.6	95.5	81.9	71.6	63.7	57.3
38	308.6	205.7	154.3	123.4	102.9	88.2	77.1	68.6	61.7
40	331.1	220.7	165.5	132.4	110.4	94.6	82.8	73.6	66.2
42	354.0	236.0	177.0	141.6	118.0	101.1	88.5	78.7	70.8
44	377.3	251.5	188.7	150.9	125.8	107.8	94.3	83.8	75.5
46	401.0	267.4	200.5	160.4	133.7	114.6	100.3	89.1	80.2
48	425.1	283.4	212.6	170.1	141.7	121.5	106.3	94.5	85.0
50	449.6	299.8	224.8	179.9	149.9	128.5	112.4	99.9	89.9
52	474.5	316.3	237.2	189.8	158.2	135.6	118.6	105.4	94.9
54	499.7	333.1	249.9	199.9	166.6	142.8	124.9	111.0	99.9
56	525.3	350.2	262.6	210.1	175.1	150.1	131.3	116.7	105.1
58	551.2	367.5	275.6	220.5	183.7	157.5	137.8	122.5	110.2
60	577.4	385.0	288.7	231.0	192.5	165.0	144.4	128.3	115.5
62	604.0	402.7	302.0	241.6	201.3	172.6	151.0	134.2	120.8
64	630.9	420.6	315.4	252.4	210.3	180.3	157.7	140.2	126.2
66	658.1	438.7	329.0	263.2	219.4	188.0	164.5	146.2	131.6
68	685.6	457.1	342.8	274.2	228.5	195.9	171.4	152.4	137.1
70	713.4	475.6	356.7	285.4	237.8	203.8	178.4	158.5	142.7
72	741.5	494.4	370.8	296.6	247.2	211.9	185.4	164.8	148.3
74	769.9	513.3	385.0	308.0	256.6	220.0	192.5	171.1	154.0
76	798.6	532.4	399.3	319.5	266.2	228.2	199.7	177.5	159.7
78	827.6	551.7	413.8	331.0	275.9	236.5	206.9	183.9	165.5
80	856.9	571.2	428.4	342.7	285.6	244.8	214.2	190.4	171.4
82	886.4	590.9	443.2	354.6	295.5	253.3	221.6	197.0	177.3
84	916.2	610.8	458.1	366.5	305.4	261.8	229.0	203.6	183.2
86	946.3	630.8	473.1	378.5	315.4	270.4	236.6	210.3	189.3
88	976.6	651.1	488.3	390.6	325.5	279.0	244.1	217.0	195.3
90	1007.2	671.4	503.6	402.9	335.7	287.8	251.8	223.8	201.4
92	1038.0	692.0	519.0	415.2	346.0	296.6	259.5	230.7	207.6
94	1069.1	712.7	534.5	427.6	356.4	305.4	267.3	237.6	213.8
96	1100.4	733.6	550.2	440.2	366.8	314.4	275.1	244.5	220.1
98	1132.0	754.7	566.0	452.8	377.3	323.4	283.0	251.6	226.4
100	1163.8	775.9	581.9	465.5	387.9	332.5	290.9	258.6	232.8
102	1195.8	797.2	597.9	478.3	398.6	341.7	299.0	265.7	239.2
104	1228.1	818.8	614.1	491.3	409.4	350.9	307.0	272.9	245.6
106	1260.7	840.4	630.3	504.3	420.2	360.2	315.2	280.1	252.1
108	1293.4	862.3	646.7	517.4	431.1	369.5	323.4	287.4	258.7
110	1326.4	884.3	663.2	530.6	442.1	379.0	331.6	294.8	265.3
112	1359.6	906.4	679.8	543.8	453.2	388.5	339.9	302.1	271.9
114	1393.0	928.7	696.5	557.2	464.3	398.0	348.2	309.6	278.6
116	1426.6	951.1	713.3	570.7	475.5	407.6	356.7	317.0	285.3
118	1460.5	973.7	730.2	584.2	486.8	417.3	365.1	324.6	292.1
120	1494.6	996.4	747.3	597.8	498.2	427.0	373.6	332.1	298.9
122	1528.8	1019.2	764.4	611.5	509.6	436.8	382.2	339.7	305.8
124	1563.3	1042.2	781.7	625.3	521.1	446.7	390.8	347.4	312.7
126	1598.0	1065.4	799.0	639.2	532.7	456.6	399.5	355.1	319.6
128	1632.9	1088.6	816.5	653.2	544.3	466.6	408.2	362.9	326.6
130	1668.0	1112.0	834.0	667.2	556.0	476.6	417.0	370.7	333.6
132	1703.3	1135.6	851.7	681.3	567.8	486.7	425.8	378.5	340.7
134	1738.9	1159.2	869.4	695.5	579.6	496.8	434.7	386.4	347.8
136	1774.6	1183.0	887.3	709.8	591.5	507.0	443.6	394.3	354.9
138	1810.5	1207.0	905.2	724.2	603.5	517.3	452.6	402.3	362.1
140	1846.6	1231.0	923.3	738.6	615.5	527.6	461.6	410.3	369.3
142	1882.8	1255.2	941.4	753.1	627.6	538.0	470.7	418.4	376.6
144	1919.3	1279.6	959.7	767.7	639.8	548.4	479.8	426.5	383.9
146	1956.0	1304.0	978.0	782.4	652.0	558.9	489.0	434.7	391.2
148	1992.9	1328.6	996.4	797.1	664.3	569.4	498.2	442.9	398.6
150	2029.9	1353.3	1014.9	812.0	676.6	580.0	507.5	451.1	406.0
152	2067.1	1378.1	1033.6	826.8	689.0	590.6	516.8	459.4	413.4
154	2104.5	1403.0	1052.3	841.8	701.5	601.3	526.1	467.7	420.9
156	2142.1	1428.1	1071.1	856.8	714.0	612.0	535.5	476.0	428.4
158	2179.9	1453.3	1089.9	872.0	726.6	622.8	545.0	484.4	436.0
160	2217.8	1478.6	1108.9	887.1	739.3	633.7	554.5	492.9	443.6
162	2256.0	1504.0	1128.0	902.4	752.0	644.6	564.0	501.3	451.2
164	2294.3	1529.5	1147.1	917.7	764.8	655.5	573.6	509.8	458.9
166	2332.7	1555.2	1166.4	933.1	777.6	666.5	583.2	518.4	466.5
168	2371.4	1580.9	1185.7	948.6	790.5	677.5	592.8	527.0	474.3
170	2410.2	1606.8	1205.1	964.1	803.4	688.6	602.5	535.6	482.0
172	2449.2	1632.8	1224.6	979.7	816.4	699.8	612.3	544.3	489.8
174	2488.3	1658.9	1244.2	995.3	829.4	711.0	622.1	553.0	497.7
176	2527.7	1685.1	1263.8	1011.1	842.6	722.2	631.9	561.7	505.5
178	2567.2	1711.4	1283.6	1026.9	855.7	733.5	641.8	570.5	513.4
180	2606.8	1737.9	1303.4	1042.7	868.9	744.8	651.7	579.3	521.4

A.3 Injected Activity (MBq): Discovery MI - QFX β = 600

SNR = 5									
Body Mass	Bed Duration (min)								
(kg)	1	1.5	2	2.5	3	3.5	4	4.5	5
10	6.4	4.3	3.2	2.6	2.1	1.8	1.6	1.4	1.3
12	8.3	5.5	4.1	3.3	2.8	2.4	2.1	1.8	1.7
14	10.2	6.8	5.1	4.1	3.4	2.9	2.6	2.3	2.0
16	12.3	8.2	6.1	4.9	4.1	3.5	3.1	2.7	2.5
18	14.4	9.6	7.2	5.8	4.8	4.1	3.6	3.2	2.9
20	16.7	11.1	8.3	6.7	5.6	4.8	4.2	3.7	3.3
22	19.0	12.7	9.5	7.6	6.3	5.4	4.7	4.2	3.8
24	21.4	14.3	10.7	8.6	7.1	6.1	5.3	4.8	4.3
26	23.9	15.9	11.9	9.6	8.0	6.8	6.0	5.3	4.8
28	26.4	17.6	13.2	10.6	8.8	7.6	6.6	5.9	5.3
30	29.1	19.4	14.5	11.6	9.7	8.3	7.3	6.5	5.8
32	31.8	21.2	15.9	12.7	10.6	9.1	7.9	7.1	6.4
34	34.5	23.0	17.3	13.8	11.5	9.9	8.6	7.7	6.9
36	37.3	24.9	18.7	14.9	12.4	10.7	9.3	8.3	7.5
38	40.2	26.8	20.1	16.1	13.4	11.5	10.0	8.9	8.0
40	43.1	28.7	21.6	17.2	14.4	12.3	10.8	9.6	8.6
42	46.1	30.7	23.1	18.4	15.4	13.2	11.5	10.2	9.2
44	49.1	32.8	24.6	19.7	16.4	14.0	12.3	10.9	9.8
46	52.2	34.8	26.1	20.9	17.4	14.9	13.1	11.6	10.4
48	55.4	36.9	27.7	22.2	18.5	15.8	13.8	12.3	11.1
50	58.6	39.0	29.3	23.4	19.5	16.7	14.6	13.0	11.7
52	61.8	41.2	30.9	24.7	20.6	17.7	15.5	13.7	12.4
54	65.1	43.4	32.5	26.0	21.7	18.6	16.3	14.5	13.0
56	68.4	45.6	34.2	27.4	22.8	19.5	17.1	15.2	13.7
58	71.8	47.9	35.9	28.7	23.9	20.5	17.9	16.0	14.4
60	75.2	50.1	37.6	30.1	25.1	21.5	18.8	16.7	15.0
62	78.7	52.5	39.3	31.5	26.2	22.5	19.7	17.5	15.7
64	82.2	54.8	41.1	32.9	27.4	23.5	20.5	18.3	16.4
66	85.7	57.2	42.9	34.3	28.6	24.5	21.4	19.1	17.1
68	89.3	59.5	44.7	35.7	29.8	25.5	22.3	19.8	17.9
70	92.9	62.0	46.5	37.2	31.0	26.6	23.2	20.7	18.6
72	96.6	64.4	48.3	38.6	32.2	27.6	24.1	21.5	19.3
74	100.3	66.9	50.1	40.1	33.4	28.7	25.1	22.3	20.1
76	104.0	69.4	52.0	41.6	34.7	29.7	26.0	23.1	20.8
78	107.8	71.9	53.9	43.1	35.9	30.8	27.0	24.0	21.6
80	111.6	74.4	55.8	44.6	37.2	31.9	27.9	24.8	22.3
82	115.5	77.0	57.7	46.2	38.5	33.0	28.9	25.7	23.1
84	119.3	79.6	59.7	47.7	39.8	34.1	29.8	26.5	23.9
86	123.3	82.2	61.6	49.3	41.1	35.2	30.8	27.4	24.7
88	127.2	84.8	63.6	50.9	42.4	36.3	31.8	28.3	25.4
90	131.2	87.5	65.6	52.5	43.7	37.5	32.8	29.2	26.2
92	135.2	90.1	67.6	54.1	45.1	38.6	33.8	30.0	27.0
94	139.3	92.8	69.6	55.7	46.4	39.8	34.8	30.9	27.9
96	143.3	95.6	71.7	57.3	47.8	41.0	35.8	31.9	28.7
98	147.5	98.3	73.7	59.0	49.2	42.1	36.9	32.8	29.5
100	151.6	101.1	75.8	60.6	50.5	43.3	37.9	33.7	30.3
102	155.8	103.8	77.9	62.3	51.9	44.5	38.9	34.6	31.2
104	160.0	106.7	80.0	64.0	53.3	45.7	40.0	35.6	32.0
106	164.2	109.5	82.1	65.7	54.7	46.9	41.1	36.5	32.8
108	168.5	112.3	84.2	67.4	56.2	48.1	42.1	37.4	33.7
110	172.8	115.2	86.4	69.1	57.6	49.4	43.2	38.4	34.6
112	177.1	118.1	88.6	70.8	59.0	50.6	44.3	39.4	35.4
114	181.5	121.0	90.7	72.6	60.5	51.8	45.4	40.3	36.3
116	185.8	123.9	92.9	74.3	61.9	53.1	46.5	41.3	37.2
118	190.2	126.8	95.1	76.1	63.4	54.4	47.6	42.3	38.0
120	194.7	129.8	97.3	77.9	64.9	55.6	48.7	43.3	38.9
122	199.2	132.8	99.6	79.7	66.4	56.9	49.8	44.3	39.8
124	203.6	135.8	101.8	81.5	67.9	58.2	50.9	45.3	40.7
126	208.2	138.8	104.1	83.3	69.4	59.5	52.0	46.3	41.6
128	212.7	141.8	106.4	85.1	70.9	60.8	53.2	47.3	42.5
130	217.3	144.9	108.6	86.9	72.4	62.1	54.3	48.3	43.5
132	221.9	147.9	110.9	88.8	74.0	63.4	55.5	49.3	44.4
134	226.5	151.0	113.3	90.6	75.5	64.7	56.6	50.3	45.3
136	231.2	154.1	115.6	92.5	77.1	66.0	57.8	51.4	46.2
138	235.8	157.2	117.9	94.3	78.6	67.4	59.0	52.4	47.2
140	240.5	160.4	120.3	96.2	80.2	68.7	60.1	53.5	48.1
142	245.3	163.5	122.6	98.1	81.8	70.1	61.3	54.5	49.1
144	250.0	166.7	125.0	100.0	83.3	71.4	62.5	55.6	50.0
146	254.8	169.9	127.4	101.9	84.9	72.8	63.7	56.6	51.0
148	259.6	173.1	129.8	103.8	86.5	74.2	64.9	57.7	51.9
150	264.4	176.3	132.2	105.8	88.1	75.5	66.1	58.8	52.9
152	269.3	179.5	134.6	107.7	89.8	76.9	67.3	59.8	53.9
154	274.1	182.8	137.1	109.7	91.4	78.3	68.5	60.9	54.8
156	279.0	186.0	139.5	111.6	93.0	79.7	69.8	62.0	55.8
158	284.0	189.3	142.0	113.6	94.7	81.1	71.0	63.1	56.8
160	288.9	192.6	144.5	115.6	96.3	82.5	72.2	64.2	57.8
162	293.9	195.9	146.9	117.5	98.0	84.0	73.5	65.3	58.8
164	298.9	199.2	149.4	119.5	99.6	85.4	74.7	66.4	59.8
166	303.9	202.6	151.9	121.5	101.3	86.8	76.0	67.5	60.8
168	308.9	205.9	154.5	123.6	103.0	88.3	77.2	68.6	61.8
170	314.0	209.3	157.0	125.6	104.7	89.7	78.5	69.8	62.8
172	319.0	212.7	159.5	127.6	106.3	91.2	79.8	70.9	63.8
174	324.1	216.1	162.1	129.7	108.0	92.6	81.0	72.0	64.8
176	329.3	219.5	164.6	131.7	109.8	94.1	82.3	73.2	65.9
178	334.4	222.9	167.2	133.8	111.5	95.5	83.6	74.3	66.9
180	339.6	226.4	169.8	135.8	113.2	97.0	84.9	75.5	67.9

SNR = 8									
Body Mass	**Bed Duration (min)**								
(kg)	**1**	**1.5**	**2**	**2.5**	**3**	**3.5**	**4**	**4.5**	**5**
10	16.5	11.0	8.2	6.6	5.5	4.7	4.1	3.7	3.3
12	21.2	14.1	10.6	8.5	7.1	6.0	5.3	4.7	4.2
14	26.1	17.4	13.1	10.5	8.7	7.5	6.5	5.8	5.2
16	31.4	20.9	15.7	12.6	10.5	9.0	7.9	7.0	6.3
18	36.9	24.6	18.5	14.8	12.3	10.5	9.2	8.2	7.4
20	42.7	28.4	21.3	17.1	14.2	12.2	10.7	9.5	8.5
22	48.6	32.4	24.3	19.4	16.2	13.9	12.2	10.8	9.7
24	54.8	36.5	27.4	21.9	18.3	15.7	13.7	12.2	11.0
26	61.1	40.8	30.6	24.5	20.4	17.5	15.3	13.6	12.2
28	67.7	45.1	33.8	27.1	22.6	19.3	16.9	15.0	13.5
30	74.4	49.6	37.2	29.8	24.8	21.3	18.6	16.5	14.9
32	81.3	54.2	40.6	32.5	27.1	23.2	20.3	18.1	16.3
34	88.3	58.9	44.2	35.3	29.4	25.2	22.1	19.6	17.7
36	95.5	63.7	47.8	38.2	31.8	27.3	23.9	21.2	19.1
38	102.9	68.6	51.4	41.2	34.3	29.4	25.7	22.9	20.6
40	110.4	73.6	55.2	44.2	36.8	31.5	27.6	24.5	22.1
42	118.0	78.7	59.0	47.2	39.3	33.7	29.5	26.2	23.6
44	125.8	83.9	62.9	50.3	41.9	35.9	31.5	28.0	25.2
46	133.7	89.2	66.9	53.5	44.6	38.2	33.4	29.7	26.7
48	141.8	94.5	70.9	56.7	47.3	40.5	35.4	31.5	28.4
50	149.9	100.0	75.0	60.0	50.0	42.8	37.5	33.3	30.0
52	158.2	105.5	79.1	63.3	52.7	45.2	39.6	35.2	31.6
54	166.6	111.1	83.3	66.7	55.5	47.6	41.7	37.0	33.3
56	175.2	116.8	87.6	70.1	58.4	50.0	43.8	38.9	35.0
58	183.8	122.5	91.9	73.5	61.3	52.5	46.0	40.8	36.8
60	192.6	128.4	96.3	77.0	64.2	55.0	48.1	42.8	38.5
62	201.4	134.3	100.7	80.6	67.1	57.5	50.4	44.8	40.3
64	210.4	140.3	105.2	84.2	70.1	60.1	52.6	46.8	42.1
66	219.5	146.3	109.7	87.8	73.2	62.7	54.9	48.8	43.9
68	228.6	152.4	114.3	91.5	76.2	65.3	57.2	50.8	45.7
70	237.9	158.6	119.0	95.2	79.3	68.0	59.5	52.9	47.6
72	247.3	164.9	123.6	98.9	82.4	70.7	61.8	55.0	49.5
74	256.8	171.2	128.4	102.7	85.6	73.4	64.2	57.1	51.4
76	266.3	177.5	133.2	106.5	88.8	76.1	66.6	59.2	53.3
78	276.0	184.0	138.0	110.4	92.0	78.9	69.0	61.3	55.2
80	285.7	190.5	142.9	114.3	95.2	81.6	71.4	63.5	57.1
82	295.6	197.1	147.8	118.2	98.5	84.5	73.9	65.7	59.1
84	305.5	203.7	152.8	122.2	101.8	87.3	76.4	67.9	61.1
86	315.5	210.4	157.8	126.2	105.2	90.2	78.9	70.1	63.1
88	325.7	217.1	162.8	130.3	108.6	93.0	81.4	72.4	65.1
90	335.9	223.9	167.9	134.3	112.0	96.0	84.0	74.6	67.2
92	346.1	230.8	173.1	138.5	115.4	98.9	86.5	76.9	69.2
94	356.5	237.7	178.3	142.6	118.8	101.9	89.1	79.2	71.3
96	367.0	244.6	183.5	146.8	122.3	104.8	91.7	81.5	73.4
98	377.5	251.7	188.7	151.0	125.8	107.9	94.4	83.9	75.5
100	388.1	258.7	194.0	155.2	129.4	110.9	97.0	86.2	77.6
102	398.8	265.9	199.4	159.5	132.9	113.9	99.7	88.6	79.8
104	409.5	273.0	204.8	163.8	136.5	117.0	102.4	91.0	81.9
106	420.4	280.3	210.2	168.2	140.1	120.1	105.1	93.4	84.1
108	431.3	287.5	215.7	172.5	143.8	123.2	107.8	95.8	86.3
110	442.3	294.9	221.2	176.9	147.4	126.4	110.6	98.3	88.5
112	453.4	302.3	226.7	181.4	151.1	129.5	113.3	100.8	90.7
114	464.5	309.7	232.3	185.8	154.8	132.7	116.1	103.2	92.9
116	475.7	317.2	237.9	190.3	158.6	135.9	118.9	105.7	95.1
118	487.0	324.7	243.5	194.8	162.3	139.2	121.8	108.2	97.4
120	498.4	332.3	249.2	199.4	166.1	142.4	124.6	110.8	99.7
122	509.8	339.9	254.9	203.9	169.9	145.7	127.5	113.3	102.0
124	521.3	347.6	260.7	208.5	173.8	149.0	130.3	115.9	104.3
126	532.9	355.3	266.4	213.2	177.6	152.3	133.2	118.4	106.6
128	544.5	363.0	272.3	217.8	181.5	155.6	136.1	121.0	108.9
130	556.2	370.8	278.1	222.5	185.4	158.9	139.1	123.6	111.2
132	568.0	378.7	284.0	227.2	189.3	162.3	142.0	126.2	113.6
134	579.9	386.6	289.9	231.9	193.3	165.7	145.0	128.9	116.0
136	591.8	394.5	295.9	236.7	197.3	169.1	147.9	131.5	118.4
138	603.7	402.5	301.9	241.5	201.2	172.5	150.9	134.2	120.7
140	615.8	410.5	307.9	246.3	205.3	175.9	153.9	136.8	123.2
142	627.9	418.6	313.9	251.2	209.3	179.4	157.0	139.5	125.6
144	640.0	426.7	320.0	256.0	213.3	182.9	160.0	142.2	128.0
146	652.3	434.8	326.1	260.9	217.4	186.4	163.1	144.9	130.5
148	664.6	443.0	332.3	265.8	221.5	189.9	166.1	147.7	132.9
150	676.9	451.3	338.5	270.8	225.6	193.4	169.2	150.4	135.4
152	689.3	459.6	344.7	275.7	229.8	197.0	172.3	153.2	137.9
154	701.8	467.9	350.9	280.7	233.9	200.5	175.5	156.0	140.4
156	714.3	476.2	357.2	285.7	238.1	204.1	178.6	158.7	142.9
158	726.9	484.6	363.5	290.8	242.3	207.7	181.7	161.5	145.4
160	739.6	493.1	369.8	295.8	246.5	211.3	184.9	164.4	147.9
162	752.3	501.5	376.1	300.9	250.8	214.9	188.1	167.2	150.5
164	765.1	510.0	382.5	306.0	255.0	218.6	191.3	170.0	153.0
166	777.9	518.6	388.9	311.2	259.3	222.3	194.5	172.9	155.6
168	790.8	527.2	395.4	316.3	263.6	225.9	197.7	175.7	158.2
170	803.7	535.8	401.9	321.5	267.9	229.6	200.9	178.6	160.7
172	816.7	544.5	408.4	326.7	272.2	233.4	204.2	181.5	163.3
174	829.8	553.2	414.9	331.9	276.6	237.1	207.4	184.4	166.0
176	842.9	561.9	421.5	337.2	281.0	240.8	210.7	187.3	168.6
178	856.1	570.7	428.0	342.4	285.4	244.6	214.0	190.2	171.2
180	869.3	579.5	434.6	347.7	289.8	248.4	217.3	193.2	173.9

SNR = 10									
Body Mass	**Bed Duration (min)**								
(kg)	**1**	**1.5**	**2**	**2.5**	**3**	**3.5**	**4**	**4.5**	**5**
10	25.7	17.2	12.9	10.3	8.6	7.4	6.4	5.7	5.1
12	33.1	22.0	16.5	13.2	11.0	9.4	8.3	7.3	6.6
14	40.9	27.2	20.4	16.3	13.6	11.7	10.2	9.1	8.2
16	49.1	32.7	24.5	19.6	16.4	14.0	12.3	10.9	9.8
18	57.7	38.5	28.8	23.1	19.2	16.5	14.4	12.8	11.5
20	66.6	44.4	33.3	26.7	22.2	19.0	16.7	14.8	13.3
22	76.0	50.6	38.0	30.4	25.3	21.7	19.0	16.9	15.2
24	85.6	57.1	42.8	34.2	28.5	24.5	21.4	19.0	17.1
26	95.5	63.7	47.8	38.2	31.8	27.3	23.9	21.2	19.1
28	105.7	70.5	52.9	42.3	35.2	30.2	26.4	23.5	21.1
30	116.2	77.5	58.1	46.5	38.7	33.2	29.1	25.8	23.2
32	127.0	84.7	63.5	50.8	42.3	36.3	31.8	28.2	25.4
34	138.0	92.0	69.0	55.2	46.0	39.4	34.5	30.7	27.6
36	149.3	99.5	74.6	59.7	49.8	42.7	37.3	33.2	29.9
38	160.8	107.2	80.4	64.3	53.6	45.9	40.2	35.7	32.2
40	172.5	115.0	86.2	69.0	57.5	49.3	43.1	38.3	34.5
42	184.4	123.0	92.2	73.8	61.5	52.7	46.1	41.0	36.9
44	196.6	131.1	98.3	78.6	65.5	56.2	49.1	43.7	39.3
46	209.0	139.3	104.5	83.6	69.7	59.7	52.2	46.4	41.8
48	221.5	147.7	110.8	88.6	73.8	63.3	55.4	49.2	44.3
50	234.3	156.2	117.1	93.7	78.1	66.9	58.6	52.1	46.9
52	247.2	164.8	123.6	98.9	82.4	70.6	61.8	54.9	49.4
54	260.4	173.6	130.2	104.2	86.8	74.4	65.1	57.9	52.1
56	273.7	182.5	136.8	109.5	91.2	78.2	68.4	60.8	54.7
58	287.2	191.5	143.6	114.9	95.7	82.1	71.8	63.8	57.4
60	300.9	200.6	150.4	120.3	100.3	86.0	75.2	66.9	60.2
62	314.7	209.8	157.4	125.9	104.9	89.9	78.7	69.9	62.9
64	328.7	219.2	164.4	131.5	109.6	93.9	82.2	73.1	65.7
66	342.9	228.6	171.5	137.2	114.3	98.0	85.7	76.2	68.6
68	357.2	238.2	178.6	142.9	119.1	102.1	89.3	79.4	71.4
70	371.7	247.8	185.9	148.7	123.9	106.2	92.9	82.6	74.3
72	386.4	257.6	193.2	154.6	128.8	110.4	96.6	85.9	77.3
74	401.2	267.5	200.6	160.5	133.7	114.6	100.3	89.2	80.2
76	416.1	277.4	208.1	166.5	138.7	118.9	104.0	92.5	83.2
78	431.2	287.5	215.6	172.5	143.7	123.2	107.8	95.8	86.2
80	446.5	297.6	223.2	178.6	148.8	127.6	111.6	99.2	89.3
82	461.9	307.9	230.9	184.7	154.0	132.0	115.5	102.6	92.4
84	477.4	318.3	238.7	191.0	159.1	136.4	119.3	106.1	95.5
86	493.0	328.7	246.5	197.2	164.3	140.9	123.3	109.6	98.6
88	508.8	339.2	254.4	203.5	169.6	145.4	127.2	113.1	101.8
90	524.8	349.9	262.4	209.9	174.9	149.9	131.2	116.6	105.0
92	540.8	360.6	270.4	216.3	180.3	154.5	135.2	120.2	108.2
94	557.0	371.4	278.5	222.8	185.7	159.2	139.3	123.8	111.4
96	573.4	382.2	286.7	229.3	191.1	163.8	143.3	127.4	114.7
98	589.8	393.2	294.9	235.9	196.6	168.5	147.5	131.1	118.0
100	606.4	404.3	303.2	242.6	202.1	173.3	151.6	134.8	121.3
102	623.1	415.4	311.5	249.2	207.7	178.0	155.8	138.5	124.6
104	639.9	426.6	320.0	256.0	213.3	182.8	160.0	142.2	128.0
106	656.9	437.9	328.4	262.7	219.0	187.7	164.2	146.0	131.4
108	673.9	449.3	337.0	269.6	224.6	192.6	168.5	149.8	134.8
110	691.1	460.7	345.6	276.4	230.4	197.5	172.8	153.6	138.2
112	708.4	472.3	354.2	283.4	236.1	202.4	177.1	157.4	141.7
114	725.8	483.9	362.9	290.3	241.9	207.4	181.5	161.3	145.2
116	743.3	495.6	371.7	297.3	247.8	212.4	185.8	165.2	148.7
118	761.0	507.3	380.5	304.4	253.7	217.4	190.2	169.1	152.2
120	778.7	519.2	389.4	311.5	259.6	222.5	194.7	173.1	155.7
122	796.6	531.1	398.3	318.6	265.5	227.6	199.2	177.0	159.3
124	814.6	543.0	407.3	325.8	271.5	232.7	203.6	181.0	162.9
126	832.7	555.1	416.3	333.1	277.6	237.9	208.2	185.0	166.5
128	850.8	567.2	425.4	340.3	283.6	243.1	212.7	189.1	170.2
130	869.1	579.4	434.6	347.7	289.7	248.3	217.3	193.1	173.8
132	887.5	591.7	443.8	355.0	295.8	253.6	221.9	197.2	177.5
134	906.0	604.0	453.0	362.4	302.0	258.9	226.5	201.3	181.2
136	924.6	616.4	462.3	369.9	308.2	264.2	231.2	205.5	184.9
138	943.3	628.9	471.7	377.3	314.4	269.5	235.8	209.6	188.7
140	962.2	641.4	481.1	384.9	320.7	274.9	240.5	213.8	192.4
142	981.1	654.0	490.5	392.4	327.0	280.3	245.3	218.0	196.2
144	1000.1	666.7	500.0	400.0	333.4	285.7	250.0	222.2	200.0
146	1019.2	679.4	509.6	407.7	339.7	291.2	254.8	226.5	203.8
148	1038.4	692.3	519.2	415.4	346.1	296.7	259.6	230.8	207.7
150	1057.7	705.1	528.8	423.1	352.6	302.2	264.4	235.0	211.5
152	1077.1	718.0	538.5	430.8	359.0	307.7	269.3	239.3	215.4
154	1096.6	731.0	548.3	438.6	365.5	313.3	274.1	243.7	219.3
156	1116.1	744.1	558.1	446.5	372.0	318.9	279.0	248.0	223.2
158	1135.8	757.2	567.9	454.3	378.6	324.5	284.0	252.4	227.2
160	1155.6	770.4	577.8	462.2	385.2	330.2	288.9	256.8	231.1
162	1175.5	783.6	587.7	470.2	391.8	335.8	293.9	261.2	235.1
164	1195.4	796.9	597.7	478.2	398.5	341.5	298.9	265.6	239.1
166	1215.5	810.3	607.7	486.2	405.2	347.3	303.9	270.1	243.1
168	1235.6	823.7	617.8	494.2	411.9	353.0	308.9	274.6	247.1
170	1255.8	837.2	627.9	502.3	418.6	358.8	314.0	279.1	251.2
172	1276.1	850.8	638.1	510.5	425.4	364.6	319.0	283.6	255.2
174	1296.5	864.4	648.3	518.6	432.2	370.4	324.1	288.1	259.3
176	1317.0	878.0	658.5	526.8	439.0	376.3	329.3	292.7	263.4
178	1337.6	891.7	668.8	535.0	445.9	382.2	334.4	297.2	267.5
180	1358.3	905.5	679.1	543.3	452.8	388.1	339.6	301.8	271.7

SNR = 12									
Body Mass	**Bed Duration (min)**								
(kg)	**1**	**1.5**	**2**	**2.5**	**3**	**3.5**	**4**	**4.5**	**5**
10	37.1	24.7	18.5	14.8	12.4	10.6	9.3	8.2	7.4
12	47.6	31.7	23.8	19.0	15.9	13.6	11.9	10.6	9.5
14	58.8	39.2	29.4	23.5	19.6	16.8	14.7	13.1	11.8
16	70.7	47.1	35.3	28.3	23.6	20.2	17.7	15.7	14.1
18	83.1	55.4	41.5	33.2	27.7	23.7	20.8	18.5	16.6
20	96.0	64.0	48.0	38.4	32.0	27.4	24.0	21.3	19.2
22	109.4	72.9	54.7	43.8	36.5	31.3	27.3	24.3	21.9
24	123.2	82.2	61.6	49.3	41.1	35.2	30.8	27.4	24.6
26	137.6	91.7	68.8	55.0	45.9	39.3	34.4	30.6	27.5
28	152.3	101.5	76.1	60.9	50.8	43.5	38.1	33.8	30.5
30	167.4	111.6	83.7	67.0	55.8	47.8	41.8	37.2	33.5
32	182.9	121.9	91.4	73.2	61.0	52.3	45.7	40.6	36.6
34	198.7	132.5	99.4	79.5	66.2	56.8	49.7	44.2	39.7
36	215.0	143.3	107.5	86.0	71.7	61.4	53.7	47.8	43.0
38	231.5	154.3	115.8	92.6	77.2	66.1	57.9	51.4	46.3
40	248.4	165.6	124.2	99.4	82.8	71.0	62.1	55.2	49.7
42	265.6	177.1	132.8	106.2	88.5	75.9	66.4	59.0	53.1
44	283.1	188.7	141.5	113.2	94.4	80.9	70.8	62.9	56.6
46	300.9	200.6	150.4	120.4	100.3	86.0	75.2	66.9	60.2
48	319.0	212.7	159.5	127.6	106.3	91.1	79.7	70.9	63.8
50	337.4	224.9	168.7	134.9	112.5	96.4	84.3	75.0	67.5
52	356.0	237.3	178.0	142.4	118.7	101.7	89.0	79.1	71.2
54	374.9	250.0	187.5	150.0	125.0	107.1	93.7	83.3	75.0
56	394.1	262.7	197.1	157.6	131.4	112.6	98.5	87.6	78.8
58	413.6	275.7	206.8	165.4	137.9	118.2	103.4	91.9	82.7
60	433.3	288.8	216.6	173.3	144.4	123.8	108.3	96.3	86.7
62	453.2	302.1	226.6	181.3	151.1	129.5	113.3	100.7	90.6
64	473.4	315.6	236.7	189.3	157.8	135.2	118.3	105.2	94.7
66	493.8	329.2	246.9	197.5	164.6	141.1	123.4	109.7	98.8
68	514.4	342.9	257.2	205.8	171.5	147.0	128.6	114.3	102.9
70	535.3	356.9	267.6	214.1	178.4	152.9	133.8	119.0	107.1
72	556.4	370.9	278.2	222.6	185.5	159.0	139.1	123.6	111.3
74	577.7	385.1	288.9	231.1	192.6	165.1	144.4	128.4	115.5
76	599.2	399.5	299.6	239.7	199.7	171.2	149.8	133.2	119.8
78	621.0	414.0	310.5	248.4	207.0	177.4	155.2	138.0	124.2
80	642.9	428.6	321.5	257.2	214.3	183.7	160.7	142.9	128.6
82	665.1	443.4	332.5	266.0	221.7	190.0	166.3	147.8	133.0
84	687.4	458.3	343.7	275.0	229.1	196.4	171.9	152.8	137.5
86	710.0	473.3	355.0	284.0	236.7	202.9	177.5	157.8	142.0
88	732.7	488.5	366.4	293.1	244.2	209.4	183.2	162.8	146.5
90	755.7	503.8	377.8	302.3	251.9	215.9	188.9	167.9	151.1
92	778.8	519.2	389.4	311.5	259.6	222.5	194.7	173.1	155.8
94	802.1	534.8	401.1	320.9	267.4	229.2	200.5	178.3	160.4
96	825.6	550.4	412.8	330.3	275.2	235.9	206.4	183.5	165.1
98	849.3	566.2	424.7	339.7	283.1	242.7	212.3	188.7	169.9
100	873.2	582.1	436.6	349.3	291.1	249.5	218.3	194.0	174.6
102	897.3	598.2	448.6	358.9	299.1	256.4	224.3	199.4	179.5
104	921.5	614.3	460.7	368.6	307.2	263.3	230.4	204.8	184.3
106	945.9	630.6	472.9	378.4	315.3	270.3	236.5	210.2	189.2
108	970.5	647.0	485.2	388.2	323.5	277.3	242.6	215.7	194.1
110	995.2	663.5	497.6	398.1	331.7	284.3	248.8	221.2	199.0
112	1020.1	680.1	510.1	408.0	340.0	291.5	255.0	226.7	204.0
114	1045.2	696.8	522.6	418.1	348.4	298.6	261.3	232.3	209.0
116	1070.4	713.6	535.2	428.2	356.8	305.8	267.6	237.9	214.1
118	1095.8	730.5	547.9	438.3	365.3	313.1	274.0	243.5	219.2
120	1121.4	747.6	560.7	448.6	373.8	320.4	280.3	249.2	224.3
122	1147.1	764.7	573.6	458.8	382.4	327.7	286.8	254.9	229.4
124	1173.0	782.0	586.5	469.2	391.0	335.1	293.2	260.7	234.6
126	1199.0	799.3	599.5	479.6	399.7	342.6	299.8	266.4	239.8
128	1225.2	816.8	612.6	490.1	408.4	350.1	306.3	272.3	245.0
130	1251.6	834.4	625.8	500.6	417.2	357.6	312.9	278.1	250.3
132	1278.0	852.0	639.0	511.2	426.0	365.2	319.5	284.0	255.6
134	1304.7	869.8	652.3	521.9	434.9	372.8	326.2	289.9	260.9
136	1331.5	887.7	665.7	532.6	443.8	380.4	332.9	295.9	266.3
138	1358.4	905.6	679.2	543.4	452.8	388.1	339.6	301.9	271.7
140	1385.5	923.7	692.7	554.2	461.8	395.9	346.4	307.9	277.1
142	1412.7	941.8	706.4	565.1	470.9	403.6	353.2	313.9	282.5
144	1440.1	960.1	720.0	576.0	480.0	411.5	360.0	320.0	288.0
146	1467.6	978.4	733.8	587.0	489.2	419.3	366.9	326.1	293.5
148	1495.3	996.8	747.6	598.1	498.4	427.2	373.8	332.3	299.1
150	1523.1	1015.4	761.5	609.2	507.7	435.2	380.8	338.5	304.6
152	1551.0	1034.0	775.5	620.4	517.0	443.1	387.7	344.7	310.2
154	1579.1	1052.7	789.5	631.6	526.4	451.2	394.8	350.9	315.8
156	1607.3	1071.5	803.6	642.9	535.8	459.2	401.8	357.2	321.5
158	1635.6	1090.4	817.8	654.2	545.2	467.3	408.9	363.5	327.1
160	1664.1	1109.4	832.0	665.6	554.7	475.4	416.0	369.8	332.8
162	1692.7	1128.4	846.3	677.1	564.2	483.6	423.2	376.1	338.5
164	1721.4	1147.6	860.7	688.6	573.8	491.8	430.4	382.5	344.3
166	1750.3	1166.8	875.1	700.1	583.4	500.1	437.6	388.9	350.1
168	1779.3	1186.2	889.6	711.7	593.1	508.4	444.8	395.4	355.9
170	1808.4	1205.6	904.2	723.4	602.8	516.7	452.1	401.9	361.7
172	1837.7	1225.1	918.8	735.1	612.6	525.0	459.4	408.4	367.5
174	1867.0	1244.7	933.5	746.8	622.3	533.4	466.8	414.9	373.4
176	1896.5	1264.4	948.3	758.6	632.2	541.9	474.1	421.5	379.3
178	1926.2	1284.1	963.1	770.5	642.1	550.3	481.5	428.0	385.2
180	1955.9	1303.9	978.0	782.4	652.0	558.8	489.0	434.6	391.2

SNR = 15									
Body Mass	**Bed Duration (min)**								
(kg)	**1**	**1.5**	**2**	**2.5**	**3**	**3.5**	**4**	**4.5**	**5**
10	57.9	38.6	29.0	23.2	19.3	16.6	14.5	12.9	11.6
12	74.4	49.6	37.2	29.8	24.8	21.3	18.6	16.5	14.9
14	91.9	61.3	46.0	36.8	30.6	26.3	23.0	20.4	18.4
16	110.4	73.6	55.2	44.2	36.8	31.5	27.6	24.5	22.1
18	129.8	86.5	64.9	51.9	43.3	37.1	32.4	28.8	26.0
20	150.0	100.0	75.0	60.0	50.0	42.8	37.5	33.3	30.0
22	170.9	113.9	85.4	68.4	57.0	48.8	42.7	38.0	34.2
24	192.6	128.4	96.3	77.0	64.2	55.0	48.1	42.8	38.5
26	214.9	143.3	107.5	86.0	71.6	61.4	53.7	47.8	43.0
28	237.9	158.6	119.0	95.2	79.3	68.0	59.5	52.9	47.6
30	261.5	174.4	130.8	104.6	87.2	74.7	65.4	58.1	52.3
32	285.8	190.5	142.9	114.3	95.3	81.6	71.4	63.5	57.2
34	310.5	207.0	155.3	124.2	103.5	88.7	77.6	69.0	62.1
36	335.9	223.9	167.9	134.4	112.0	96.0	84.0	74.6	67.2
38	361.7	241.2	180.9	144.7	120.6	103.4	90.4	80.4	72.3
40	388.1	258.7	194.1	155.2	129.4	110.9	97.0	86.2	77.6
42	415.0	276.7	207.5	166.0	138.3	118.6	103.7	92.2	83.0
44	442.3	294.9	221.2	176.9	147.4	126.4	110.6	98.3	88.5
46	470.2	313.4	235.1	188.1	156.7	134.3	117.5	104.5	94.0
48	498.4	332.3	249.2	199.4	166.1	142.4	124.6	110.8	99.7
50	527.1	351.4	263.6	210.9	175.7	150.6	131.8	117.1	105.4
52	556.3	370.9	278.1	222.5	185.4	158.9	139.1	123.6	111.3
54	585.8	390.6	292.9	234.3	195.3	167.4	146.5	130.2	117.2
56	615.8	410.5	307.9	246.3	205.3	175.9	154.0	136.8	123.2
58	646.2	430.8	323.1	258.5	215.4	184.6	161.5	143.6	129.2
60	677.0	451.3	338.5	270.8	225.7	193.4	169.2	150.4	135.4
62	708.1	472.1	354.1	283.2	236.0	202.3	177.0	157.4	141.6
64	739.6	493.1	369.8	295.9	246.5	211.3	184.9	164.4	147.9
66	771.5	514.4	385.8	308.6	257.2	220.4	192.9	171.5	154.3
68	803.8	535.9	401.9	321.5	267.9	229.7	200.9	178.6	160.8
70	836.4	557.6	418.2	334.6	278.8	239.0	209.1	185.9	167.3
72	869.4	579.6	434.7	347.7	289.8	248.4	217.3	193.2	173.9
74	902.7	601.8	451.3	361.1	300.9	257.9	225.7	200.6	180.5
76	936.3	624.2	468.1	374.5	312.1	267.5	234.1	208.1	187.3
78	970.3	646.8	485.1	388.1	323.4	277.2	242.6	215.6	194.1
80	1004.6	669.7	502.3	401.8	334.9	287.0	251.1	223.2	200.9
82	1039.2	692.8	519.6	415.7	346.4	296.9	259.8	230.9	207.8
84	1074.1	716.1	537.1	429.6	358.0	306.9	268.5	238.7	214.8
86	1109.4	739.6	554.7	443.7	369.8	317.0	277.3	246.5	221.9
88	1144.9	763.3	572.5	458.0	381.6	327.1	286.2	254.4	229.0
90	1180.8	787.2	590.4	472.3	393.6	337.4	295.2	262.4	236.2
92	1216.9	811.3	608.5	486.8	405.6	347.7	304.2	270.4	243.4
94	1253.3	835.6	626.7	501.3	417.8	358.1	313.3	278.5	250.7
96	1290.1	860.0	645.0	516.0	430.0	368.6	322.5	286.7	258.0
98	1327.1	884.7	663.5	530.8	442.4	379.2	331.8	294.9	265.4
100	1364.4	909.6	682.2	545.8	454.8	389.8	341.1	303.2	272.9
102	1402.0	934.6	701.0	560.8	467.3	400.6	350.5	311.5	280.4
104	1439.8	959.9	719.9	575.9	479.9	411.4	360.0	320.0	288.0
106	1477.9	985.3	739.0	591.2	492.6	422.3	369.5	328.4	295.6
108	1516.3	1010.9	758.2	606.5	505.4	433.2	379.1	337.0	303.3
110	1555.0	1036.7	777.5	622.0	518.3	444.3	388.7	345.6	311.0
112	1593.9	1062.6	797.0	637.6	531.3	455.4	398.5	354.2	318.8
114	1633.1	1088.7	816.5	653.2	544.4	466.6	408.3	362.9	326.6
116	1672.5	1115.0	836.3	669.0	557.5	477.9	418.1	371.7	334.5
118	1712.2	1141.5	856.1	684.9	570.7	489.2	428.1	380.5	342.4
120	1752.2	1168.1	876.1	700.9	584.1	500.6	438.0	389.4	350.4
122	1792.4	1194.9	896.2	716.9	597.5	512.1	448.1	398.3	358.5
124	1832.8	1221.9	916.4	733.1	610.9	523.7	458.2	407.3	366.6
126	1873.5	1249.0	936.7	749.4	624.5	535.3	468.4	416.3	374.7
128	1914.4	1276.3	957.2	765.8	638.1	547.0	478.6	425.4	382.9
130	1955.5	1303.7	977.8	782.2	651.8	558.7	488.9	434.6	391.1
132	1996.9	1331.3	998.5	798.8	665.6	570.6	499.2	443.8	399.4
134	2038.6	1359.0	1019.3	815.4	679.5	582.4	509.6	453.0	407.7
136	2080.4	1387.0	1040.2	832.2	693.5	594.4	520.1	462.3	416.1
138	2122.5	1415.0	1061.3	849.0	707.5	606.4	530.6	471.7	424.5
140	2164.8	1443.2	1082.4	865.9	721.6	618.5	541.2	481.1	433.0
142	2207.4	1471.6	1103.7	883.0	735.8	630.7	551.8	490.5	441.5
144	2250.1	1500.1	1125.1	900.1	750.0	642.9	562.5	500.0	450.0
146	2293.1	1528.8	1146.6	917.3	764.4	655.2	573.3	509.6	458.6
148	2336.3	1557.6	1168.2	934.5	778.8	667.5	584.1	519.2	467.3
150	2379.8	1586.5	1189.9	951.9	793.3	679.9	594.9	528.8	476.0
152	2423.4	1615.6	1211.7	969.4	807.8	692.4	605.9	538.5	484.7
154	2467.3	1644.8	1233.6	986.9	822.4	704.9	616.8	548.3	493.5
156	2511.3	1674.2	1255.7	1004.5	837.1	717.5	627.8	558.1	502.3
158	2555.6	1703.7	1277.8	1022.2	851.9	730.2	638.9	567.9	511.1
160	2600.1	1733.4	1300.1	1040.0	866.7	742.9	650.0	577.8	520.0
162	2644.8	1763.2	1322.4	1057.9	881.6	755.7	661.2	587.7	529.0
164	2689.7	1793.1	1344.8	1075.9	896.6	768.5	672.4	597.7	537.9
166	2734.8	1823.2	1367.4	1093.9	911.6	781.4	683.7	607.7	547.0
168	2780.1	1853.4	1390.1	1112.0	926.7	794.3	695.0	617.8	556.0
170	2825.6	1883.7	1412.8	1130.2	941.9	807.3	706.4	627.9	565.1
172	2871.3	1914.2	1435.7	1148.5	957.1	820.4	717.8	638.1	574.3
174	2917.2	1944.8	1458.6	1166.9	972.4	833.5	729.3	648.3	583.4
176	2963.3	1975.6	1481.7	1185.3	987.8	846.7	740.8	658.5	592.7
178	3009.6	2006.4	1504.8	1203.9	1003.2	859.9	752.4	668.8	601.9
180	3056.1	2037.4	1528.1	1222.5	1018.7	873.2	764.0	679.1	611.2